INTER-BAR CURRENTS IN ROTATING STATOR INDUCTION MACHINES

INTER-BAR CURRENTS
IN
ROTATING STATOR INDUCTION MACHINES

By

STEPHEN CZARNUCH, B.ENG. & MGMT.

A Thesis
Submitted to the School of Graduate Studies
in Partial Fulfillment of the Requirements
for the Degree of
Masters of Applied Sciences

McMaster University
Hamilton, Ontario, Canada
December, 2005

MASTER OF APPLIED SCIENCE (2005) McMaster University

(Engineering) Hamilton, Ontario

TITLE: Inter-bar Currents in Rotating Stator Induction Machines

AUTHOR: Stephen Czarnuch, B. Eng. & Mgmt. (McMaster University)

SUPERVISOR: Dr. Raymond Findlay

NUMBER OF PAGES: x, 169

Abstract

This work pioneers the experimental acquisition of data relating to the heating effects of inter-bar currents, and the frequency components of the main field rotating flux. Previous research in the field of inter-bar currents is reliant on theory and mathematical modeling. Yet, with the growing need for increasing machine efficiency; experimental application of conceptualized theoretical models of machine losses is paramount. Focusing specifically on inter-bar currents in a rotating stator induction machine revealed a correlation between the heat generated in the iron core and the presence of inter-bar currents. Using temperature sensing instrumentation, experimental data was gathered to determine the inter-bar current distribution along the length of the rotor bars during acceleration. Additionally, custom current transducers were implemented to directly measure the main field rotating flux. The results present a solid foundation for direct and indirect measurement of inter-bar currents.

Acknowledgments

I would like to extend a word of thanks and appreciation to all the people who supported me and made this thesis possible. I want to recognize my former colleagues at ATL Industries for their electrical and mechanical support while running the experiments, particularly Sandy Simon. Further, I am deeply indebted to Fraser MacDuffee for his support and motivation through the extent of my thesis.

I would like to thank Dr. Raymond Findlay of McMaster University for his patience, guidance and encouragement during the research and compilation of this thesis.

To my parents Stan and Regina who taught me to place value in hard work, dedication and perseverance, and to my sister Lisa for her endless support, I cannot say enough. And finally, most of all, I offer my sincerest thanks and gratitude to Rose Ricciardelli for her inspiration, motivation, patience, corrections and improvements. Without her love and support, this project would be incomplete.

Table of Contents

List of Figures

List of Tables

Chapter 1

Introduction

Induction machines are one of the most common electrical machines used by industry for automation and manufacturing because they are robust and relatively easy and inexpensive to manufacture. Induction machines offer a simple, effective method of transferring electric power to mechanical rotational power or vice-versa. However, inefficiencies exist with all machines and due to increasing demands on performance and cost reduction, the topic of induction machine efficiency has attracted the attention of researchers for decades.

Induction machine efficiency is defined as the rated output power achieved as a percentage of the required input power, with the difference between the two coming from losses. The losses in an induction machine can be broken down into two main types: conventional losses, calculated using the loss segregation method, and stray load losses. The conventional losses were widely accepted by the design community as losses that can be accounted for through analytical and mathematical calculations prior to the construction of an induction machine, and verifiable through experimentation and measurement. However, after the construction of the machines, additional losses are measured beyond the losses determined by conventional means. The difference between the total measured losses and the losses calculated by conventional methods were termed stray-load losses primarily because of their perceived dependence on the loading of the machines. Unlike the conventional losses, there is not a universal acceptance by the academic community of either the magnitude of stray load losses or methods to account for them at the design stage. The result is an inconsistent and somewhat arbitrary allocation for stray load losses at the design stage based largely on manufacturer experience.

1.1 General Description of the problem

In general, the individual components that comprise stray load losses are well documented, and a broad understanding of the causes of most of the components are known. Stray load losses can be divided into two general categories; fundamental frequency and high frequency losses. The fundamental-frequency components are eddy current losses in the stator conductors, end-ring losses due to leakage fluxes and skewed rotor losses in skewed rotor machines. The high-frequency components are induced eddy current losses in the rotor, induced losses in the stator resulting from the rotor m.m.f. harmonics and losses due to inter-bar currents.

Most stray load losses that occur in the stator of an induction machine can be measured either directly or indirectly using various instruments through experimentation. This is because the stator of a typical induction machine is stationary, while the rotor is allowed to rotate freely. As a result, many conceptual and theoretical stray load loss models can be tested and verified for the stator. Conversely, the rotor stray load losses are usually difficult to measure because the rotor cannot be directly instrumented since it is rotating. Additionally, the rotor of a standard induction machine is mechanically buried within the stator, making it difficult to access critical areas with sensitive instruments.

Despite the difficulties presented with measuring rotor stray load losses, experimental data related to them is still relevant. Specifically, high-frequency inter-bar current losses are important because it is believed that these losses are much higher than presently accounted for. Several authors in the academic community have developed mathematical models and theoretical frameworks to predict and account for inter-bar currents, but little work has been done to experimentally verify these postulates.

1.2 Purpose of this project

The challenge of measuring inter-bar currents is particularly difficult beyond the physical restrictions because the presence, magnitude, distribution and effects of inter-bar currents are relatively unknown. It is the purpose of this project to experimentally determine inter-bar currents through the use of a custom inverted induction machine. A special rotating stator induction machine was designed at McMaster University and manufactured by Westinghouse to allow direct instrumentation of the rotor without suffering losses through slip rings or other indirect means. The measurements are taken from the rotor using thermocouples and search coils to measure the heat generated by inter-bar currents, as well as to determine the inter-bar current waveform.

It is the core intention of this thesis to mathematically correlate the heat generated in the iron core of the rotating stator induction machine rotor to inter-bar currents using experimental data. The instantaneous rate-of-rise of temperature during start-up, modeled with an ohmic heating equation will then be used to calculate the magnitude of inter-bar currents. Fundamental to the rate-of-rise calculations is the assumption that inter-bar currents are constant during motor operation, and that the heat generated in the iron core during the initial seconds of acceleration is from inter-bar currents in isolation.

The resultant heating effects of inter-bar currents, determined from experimentation, will be used to calculate the RMS value of inter-bar currents required to generate the temperature rise at select points in the rotor iron. However, because of the relatively slow thermal response of iron compared to the frequency of the inter-bar currents, the thermal models will not give insight into the waveform and frequency components of inter-bar currents. Consequently, custom current transducers, or search coils, will be used to obtain detailed data relating to the frequency composition of inter-bar currents.

1.3 Scope of the project

The intention of this project is to generate a compendium of theoretical research related to inter-bar currents, a significant component of stray load losses. Based on the theoretical work of core authors in the field, two major experimental tests will be performed to generate data related to both the thermal effects and the frequency components of inter-bar currents. The scope of this project is limited to the acquisition of the experimental data and analysis of the results to obtain preliminary information related to the presence, magnitude, distribution, frequency components and effects of inter-bar currents.

A supplementary objective is to determine the usefulness of thermocouples, Resistance Temperature Detectors (RTD's) and custom current transducers for inter-bar current measurement. The evaluation of the various devices will be based on how effectively experimental data acquired from these instruments, and how well the data can be applied to determine both the inter-bar current distribution and a thermal distribution in the rotor iron. Finally, this thesis is intended to contribute experimental data to a field of research heavily dominated by theoretical study.

1.4 Organization of the thesis

A comprehensive review of stray load losses in general and inter-bar currents specifically, with particular focus on increased machine efficiency requirements driven by industry, is presented in Chapter 2. This chapter includes a detailed review of the work of major authors in the field of stray load losses and inter-bar currents. The parameters and design considerations affecting the presence and effects of inter-bar currents, as well as several mathematical models and methods used to calculate inter-bar currents are also presented in Chapter 2.

Chapters 3 through 5 are related to the physical experiments referenced throughout this project, and the procedures used to obtain data related to inter-bar currents. Chapter

3 outlines the motivations behind the two major types of tests used in the experiments: indirect temperature and direct search coil tests. Additionally, the fundamental principles behind the two tests and the methods with which they will be used to determine information relating to inter-bar currents will also be presented.

Chapter 4 describes the experimental equipment used to perform the test, including relevant information on the custom inverted induction machine, the electrical and the mechanical connections. A detailed description of the instrumentation used, the configuration of the instruments on the motor, and the data acquisition system is also provided. Chapter 4 concludes with a thorough explanation of the tests, including timing charts for the application and removal of the excitation, expected temperature increases and test duration.

The raw results of the two thermal tests are presented in Chapter 5 along with representative best-fit polynomials for critical portions of each test. This chapter also includes the raw results of the direct measurement tests, both in the time domain and in the frequency domain. The direct measurement test results are also dissected into the individual frequency components of the signals.

Chapter 6 focuses on the analysis of the data and models presented in Chapter 5. The results of the thermal tests are used to obtain the rate-of-rise of temperature during start-up, which is then used to derive an expression for the inter-bar current at various points in the rotor iron. From these results, the thermal distribution across the rotor is proposed. Similarly, the direct measurement test results are investigated, with specific attention to the source of the individual frequency components.

Finally, Chapter 7 outlines the main contributions of this thesis and how the results pioneer practical, experimental work in the field of Inter-bar currents. The final chapter concludes with recommended future work that can build from the results of this project.

References used for this project are included at the end, followed by three appendices. Appendix A contains a partial set of mechanical and assembly drawings constructed from physical measurements of the motor. Appendix B displays relevant raw data and plots used for preliminary analysis throughout the project. Appendix C contains information about the data acquisition system hardware, as well as the physical and electrical setup of the system.

Chapter 2

Comprehensive Review

This chapter begins with a general discussion of induction machines and their common uses in industry. Issues relating to the efficiency of induction machines are presented, with particular attention to stray load losses and more specifically inter-bar currents in induction machines. A comprehensive review of key literature in the field of stray load losses and inter-bar currents is then offered. The chapter continues with a discussion about the effects of inter-bar currents as a specific case of stray load losses, with emphasis on heat generation, and general performance of induction machines. Finally, the chapter is concluded with a compendium of present and historical methods used to calculate and predict inter-bar currents.

2.1 Background: Industry and the induction motor

In today's industrialized society, high efficiency and productivity are requirements for making business's profitable, and they often distinguish successful ventures from failures. In business, the topic of efficiency is often associated with cost reduction. Generally, the cost of running a business is the sum of a fixed overhead cost, consisting of expenses such as property cost and utilities, and variable costs like labour and materials. Historically, industry has dedicated many resources to reducing both fixed and variable costs to increase profit.

A common method of reducing variable costs is by minimizing the cost of labour through automation. However, automation often means an increase in capital expenditure because automation involves the replacement of workers with machines consisting of devices such as controllers, motors, and hydraulic and pneumatic systems, all of which consume resources. One of the most common devices integrated in automated equipment is the electric motor. The induction motor, in particular, is responsible for much of the electrical power consumed by industry and commerce [1]. Induction motors are robust, easy and inexpensive to manufacture compared to other electric motors, and can be easily controlled for output speed and torque [2]. The most common induction motor used by industry by far is the squirrel-cage induction motor, because it has the lowest manufacturing cost, the highest reliability, requires no slip rings and has no brushes, which reduces the requirements for maintenance [3]. Unfortunately, induction motors are generally less efficient compared to other types of electric motors.

Induction machine efficiency is particularly important to business because roughly 70% of the electrical energy consumed by industry is by electrical machines [4], therefore increased operating efficiency will reduce fixed utility costs. The popularity of induction machines in industry and society has motivated the study of their efficiency by researchers dating back as far as the final decade of the 1800's. Unfortunately, a universal method of calculating and modeling all machine losses still does not exist because the issues surrounding the determination and measurement of machine efficiency are complicated[1]. There is significant pressure on the academic community to continue the development of methods to predict and accurately state machine efficiency, because "[customers] are interested in the total loss in the machine as this is the useless power they are paying for" [1].

The importance industry is placing on increasing machine efficiency, or conversely reducing machine losses, is increasing the pressure placed on induction machine designers to accurately determine and state machine ratings. Surprisingly, it is well documented that allocations for inefficiencies at the design stage have been erroneous for several decades, yet little progress has been made in rectifying the problem [5]. From the end users perspective, this results in an induction machine that cannot necessarily perform to specification. The most prevalent obstacle facing induction machine designers and users is the lack of a universal technique or method to calculate machine efficiency before construction, and to measure losses after manufacturing. The challenge facing the academic community is to first determine the source of induction machine losses, and then develop standard methods of reducing or eliminating these losses.

2.1.1 The principle of power transfer in induction motors

In order to quantify and eventually reduce or eliminate losses in induction motors, a comprehensive understanding of how power is converted and consumed by these machines is paramount. The purpose of an electrical motor, whether single phase or

---

[1] Determination and measurement of efficiency are discussed in detail in Section 2.1.3

poly-phase, is to convert electrical power to mechanical power, most often in rotary form. Induction motors are mechanically constructed of a cylindrical rotor imbedded in a concentrically larger cylindrical stator. For the large majority of induction motors in industry, the stator is fixed in position and the rotor is allowed to rotate freely around the axis of the machine, although some applications exist in which the rotor is fixed and the stator is allowed to rotate. In almost all cases electrical current is induced in the rotor when power is applied to the stator windings, whether directly by stationary terminals or through slip rings.

The power flow in a standard squirrel-cage induction machine is briefly summarized as follows [2]:

1. The input power results from an electrical current in the stator winding, and is necessary for setting up an electromagnetic field. Since there is current through a conductor with a finite resistance, some power is expended as I^2R losses, typically referred to as stator copper loss.
2. The remaining power contained in the electromagnetic field can be resolved into a non-leakage and a leakage component:
    i. The non-leakage component is transferred across the stator air gap boundary either into the air gap or out of the air gap, returning to the power system. The power that is transferred into the air gap is either absorbed, accounting for mechanical power conversion, or is transferred across the rotor air gap boundary into the rotor. During this process, the electromagnetic field is interacting with the stator iron, inducing eddy

currents in the core and causing hysteresis loss. These loss components are commonly referred to as stator core loss.

ii. The leakage component can be further split into three elements. The first, referred to as skin effect, is a frequency-related loss phenomenon that occurs in the stator windings. The second, end region leakage power, is associated with magnetic fields around the end-regions. This leakage power is either stored in the air gaps in the end regions or expended as heat generated by eddy currents in the motor materials, and is most prevalent in ferromagnetic materials. The third, non-end region leakage power, will either cross the stator air gap boundary into the air gap, or cause eddy current and hysteresis losses in the stator core, and is partially responsible for causing vibration and noise during operation.

3. The components of power that are transferred through the air gap and across the rotor air gap boundary induce current in the squirrel cage windings. As was the case with the stator, these currents occur in conductors with a finite resistance, generating I^2R losses, commonly called rotor copper losses. These currents are necessary and responsible for generating the electromagnetic field that opposes the stator electromagnetic field, generating the mechanical rotation.
4. The electromagnetic field induced by the rotor also interacts with the rotor iron, similar to that in the stator, inducing eddy currents and hysteresis losses. This final component of loss is called rotor iron loss.

A thorough understanding of how electric power flows through the motor and is converted to mechanical power is a fundamental requirement in the eventual understanding of the sources of loss in induction motors.

2.1.2 Efficiency and Losses in Induction Machines

The induction motor acquired its name from the principle of operation of the machine Current in the primary winding, typically the stator, will generate an electromagnetic field that will induce current in the secondary windings, usually the rotor [3]. The current in the secondary windings generates an electromagnetic field that will oppose the field generated in the stator windings, resulting in a rotation of the rotor if it is allowed to turn freely, or in other words a conversion of electrical power to mechanical power. However, as discussed in the previous section, and as a result of physical properties of the motor, perfect transfer of power is impossible. An electrical motor designer must expect that certain losses will occur, but reducing losses is very much a possibility. Unfortunately, reducing losses often increases manufacturing and material costs or requires a design compromise.

For example, the conductors used to construct an induction machine have an intrinsic resistance, which varies with material. As such, I^2R loss in both the stator and the rotor will always exist. By selecting different materials with lower relative resistances, or by increasing the size of the conductors, reductions in these losses can sometimes be achieved. The trade-off is that these design changes can create additional issues such as placement of larger conductors in the slots, the material cost in manufacturing can increase, and the effects of slot harmonics can be further amplified.

The determination of different components of loss has proven difficult, especially when the origins of the losses and their effects are obscure and cannot be easily distinguished from one another. In most cases, the losses manifest in the form of additional heat production, while affecting the performance of the machine through effects such as power and torque loss [2]. As such, "the losses must be kept low, not only to achieve high efficiency, but also to keep the size of the machine to a minimum" [2]. The effects of these losses are becoming increasingly relevant due to the pressure modern industry is placing on performance requirements of induction motors. Bousbaine, Low and McCormick [6] note that "modern motors are now being operated much nearer to their overload limits because of stringent high torque to inertia requirements of mechanical systems. Consequently, the risk of adverse thermal conditions increases".

The core subjects of the determination and reduction of losses are complicated when issues with nomenclature arise. The terminology used to identify and communicate motor performance parameters and define losses is a problem that has recently been acknowledge by researchers, and was addressed thoroughly by Jimoh, Findlay, et. al. [2][7]. In addition, despite the fact that induction machine losses have been researched for decades, a universally accepted method of modeling and measuring these losses does not exist. As Jimoh [2] noted, "significantly, the original goal of researchers, which is to improve machine performance and energy efficiency, is still very much relevant. In any case, there is still the need to develop widely acceptable methods of measurement and prediction of these losses, the absence of which has considerably hindered further progress on the subject". The development of suitable and universally acceptable methods of measurement and prediction will enable machine losses to be studied more effectively, eventually reducing them [2]. The general topic of losses in induction machines is well documented, yet the area of stray load losses still remains ambiguous and relatively little progress has been made in understanding and quantifying it. Bousbaine, Low and McCormick [6] state, "the estimation and experimental investigation of stray load losses in an assembled machine poses one of the most difficult problems in the characterization of losses in a machine". Stray load losses, and in particular, the losses created by imperfect rotor bar insulation, will be the core topic of this research.

2.1.3 Stray Load Losses

Several methods[2] have been developed to determine the power losses in an induction machine prior to manufacturing and fabrication, as well as to measure the actual power losses during operation. The viability and practicability of many of these tests is questionable, yet the majority of the current measurement and prediction techniques offer some further insight into losses. In general, the actual total power loss obtained from measurement and the losses calculated by mathematical or analytical means differ as a result of inadequate methods of prediction and calculation. The difference between the actual losses and the calculated losses was initially termed stray-load loss in the early

---

[2] The most prevalent methods used in industry will be thoroughly discussed in section 2.3.4 below

1960's. Christophides was one of the first authors to quantify the difference between the actual total power losses as measured by experimentation and the losses determined from the loss segregation method as stray losses [8].

The unknown or stray losses are commonly referred to as stray load losses because the effects of these losses are most prevalent while an induction machine is under load, although the designations are often used interchangeably. According to Jimoh [2], "it was discovered that stray losses are related most closely to the loading of a machine. Hence, they are called stray load losses, or load losses, or unknown losses". Yamazaki and Haruishi [9] have developed a similar, more general definition by stating that, "the difference between practical losses and the estimated losses may be classified as the stray load loss". Glew [1] noted that, "stray load losses are the consequences of the requirements of a practical machine. In an actual machine it is necessary to locate finite stator and rotor windings in discrete slots in the laminations". Veinott further expands by stating [3],

> "It is a well-established experimental fact that in any poly-phase motor losses over and above those discussed above occur under load conditions. Since the source is not accurately known, they are frequently called 'stray-load losses'. For the most part, these losses impose an additional drag or mechanical load on the motor shaft".

An in-depth analysis of the causes and effects of stray losses is presented in detail in subsequent sections[3].

The fact that stray load losses exist is well established, although much work still needs to be done to understand their causes and reduce their effects [2]. This lack of

---

[3] The causes and effects of inter-bar currents are discussed in section 2.3.2

understanding was noted by Schwartz as far back as 1965 when he stated that, "there is still considerable confusion on various aspects of stray losses, particularly with regard to their definition and origin". Schwartz accurately noted the need for a suitable definition of what is to be evaluated is necessary before determining suitable techniques for this evaluation. Jimoh [2] extends the Schwartz concept by observing that, "the question of definition as a stray load loss problem arose out of lack of success in developing a direct method for determining this loss". Carlson [10] contributes that, "stray load losses are a challenge to the industrial and scientific community because there is not consensus on standard methods to measure and calculated them".

Remaining within the above author's strict definitions, stray load losses are the difference between the power loss determined through experimentation and the losses calculated using the loss segregation method. Although stress is often placed on determining stray load losses during the design stage, there is still no consensus on the standard methods used to determine the practical losses or measure the actual losses, making the determination of stray load losses even more difficult.

Stray load losses have been particularly problematic for the academic community mainly because, "unlike stator copper loss, for example, stray load loss is neither distinct in terms of location nor unique in terms of the phenomena that lead to it" [2]. However, despite the inherent difficulties in understanding stray load losses, they remain an important topic to the industrial and academic community because of the pressure industry is placing on induction machine designers to increase machine efficiency. Particularly, in reference to stray losses, "the subject of stray load losses in induction machines has been dominated in the past by the need to improve the efficiency of this machine by reducing or eliminating these losses" [11]. According to Williamson, Poh and Smith [12], "In order to achieve this goal, one must first understand the mechanisms by which losses are produced in induction motors, and this has led to a renewed interest in stray-load losses in general and in inter-bar losses in particular".

Jimoh [2] succinctly summarized the problems still prevalent regarding stray losses in induction machines as:

1. Addressing and contributing to the question of definition, origin, components and effects of stray load loss in induction machines.
2. Addressing and solving the problems of theoretical or analytical means of evaluation.
3. Addressing and solving the problem of measurement.
4. Based on the achievements in the foregoing, addressing the questions of understanding and hence loss reduction.

Until recently, the majority of the work contributed in the area of stray load losses has been with reference to the first two points above. Measurement has been particularly problematic because of the relatively small magnitudes of some measurement values, or physical constraints placed on instrumentation, but technological and procedural advancements have revitalized interest in this area of research.

Historical Content

Olin was the first to acknowledge a difference in the losses generated within an induction motor during full load and no-load operation in 1912. He eventually developed an empirical formulation for predicting the total losses incurred for all operating points from no-load to full load. At the time, little was known about stray losses, and his work was quite revolutionary, even though it did not accurately model or account for these losses. One of the most significant faults in Olin's work was that he assumed that losses were linearly related to the load. However, despite the shortcomings of his work, he pioneered interest in discovering the true nature of induction machine losses.

Christophides was one of the first authors to mathematically model stray load losses specifically, defining them as the difference between the total power loss of an induction machine and the losses calculated using the loss segregation method. His definition is broad and acknowledges that although losses are known to exist, the exact origin, cause and effect of some losses remain unknown. The segregated losses are defined as:

(i) Friction and windage loss $P_{F\&W}$

(ii) Stator core loss P_S as determined using the no-load test

(iii) Stator conductor loss $P_{SC} = I^2R$

(iv) Rotor conductor loss $P_{RC} = s\left(P_{Input} - 3I_S^2R_{SP} - P_S\right)$, where

s is the slip at full load

P_{Input} is the stator input power

I_S is the stator phase current

R_{SP} is the resistance per phase of the stator winding

Christophides work and the work of others such as Odok [13], Subba Rao and Buttler [14] and Schwarz [15][4] were eventually reflected in national standards. The American Standard Test Code for poly-phase machines, for example, defined stray load loss as, "that portion of the total loss in a machine not accounted for by the sum of friction and windage, stator I^2R loss, rotor I^2R loss, and no-load core loss" [3]. Despite the somewhat common definitions accepted by various regulating bodies, various authors view stray load losses from different perspectives influenced by their research interest. As noted by Jimoh [27],

> Some authors gave the definition [of stray losses] from a particular aspect of the subject. For example, that by Morgan et al [16] reflects the measurement aspect, Schwarz's [15] definition is in terms of the origin of these losses; and Odok's [13] and Christofides' [8] are from the calculation or prediction point of view.

The analytical work of Odok [13] and of Subba Rao and Butler [14] were the main reference for several decades [10]. New developments in technology and computational power have allowed the exploration of new techniques such as Finite Element Methods, revitalizing study in the field of stray load losses.

Origin and Components

Although stray load losses are a general term used to describe the unknown or unaccounted losses in an induction machine, the individual components are reasonably well established. One of the difficulties hindering research and progress in reducing the

---

[4] The work of several authors is discussed in detail in section 2.3.4, with particular reference to work in identifying and modeling losses due to inter-bar currents

effects of stray losses is that although the components are quite well known and discussed individually in literature, a standardized, universally accepted list does not exist [2]. A list of the components of stray load losses as given by Schwarz [15] in 1964 repeated by Jimoh [2]:

Component	**Origin**	**Type and Location**
Surface Losses	Gap leakage (harmonic) flux	Stator and rotor core losses
Tooth-pulsation losses	Gap leakage (harmonic) flux	Stator and rotor core losses
Tooth-pulsation, squirrel-cage, circulating current losses	Gap leakage (harmonic) flux	Rotor I^2 R loss
Stator-harmonic, squirrel-cage, circulating current losses	Gap leakage (harmonic) flux	Stator I^2 R loss
Stator-slot eddy-current losses	Slot leakage flux	Stator I^2 R loss
Rotor-slot eddy-current losses	Slot leakage flux	Abnormal rotor I^2 R loss at high slip only
Stator-overhang eddy-current losses	Overhang leakage flux	Stator core loss
Rotor-overhang eddy-current losses	Overhang leakage flux	Abnormal rotor core loss at high slip only

Table 2.1: Components of Stray Load Losses Given by Schwarz [15] from Jimoh [2].

In 1963 Chalmers and Wilson [17] defined the fundamental frequency components of stray load losses, summarized by Jimoh [18] as:

i) Eddy current losses in the stator and rotor conductors due to slot-leakage fluxes

ii) Eddy current losses in the end region conductors and eddy current plus hysteresis losses in the end region iron and other components due to end region leakage fluxes

iii) Losses, mostly in the iron, due to manufacturing imperfection – the most prominent is inter-bar rotor current losses in the rotor iron of a skewed rotor with finite resistance between adjacent bars

Chalmers and Wilson [17] defined the high frequency components, noted by Jimoh [18] as:

iv) Losses in the conductor and the iron of the stator due to rotor magnetomotive force (mmf) harmonics

v) Induced losses in the rotor close to the air gap due to the stator mmf harmonics produced by the stator load current

Even if the individual components of stray load losses are partially known, separating their effects and determining their causes is quite difficult. A study of related literature suggests there are three general explanations for the various components of stray-load losses. Jimoh [2] summarizes them succinctly as:

1. The magnetic property limitations of iron that lead to saturation at load current.
2. The geometrical structures, i.e. slots, windings, and air gap, around the active region of the machine that lead to:

   (i) Space harmonics due to such effects as ripple and tooth pulsations
   (ii) Leakage flux

3. Industrial imperfection – the most prominent of which is cross-bar currents due to imperfect insulation of the squirrel cage rotor bars

The realization that stray load losses occur as a consequence of practical requirements reveals that it is sensibly impossible to completely eliminate them. As such, when the issue of increasing efficiency arises, a designer can only expect to reduce the effects of stray load losses using compensatory techniques. For example, the magnetic properties of iron cause it to reach saturation at load current. A different material could be used with more ideal magnetic properties, yet would likely come at an increased cost, could be more difficult to work with during manufacturing, may have different thermal properties, or may affect the inertia of the machine during operation.

Of particular interest to this thesis argument are stray load losses caused by manufacturing imperfections. Glew [1] noted, "Poor design and lack of manufacturing control are the main contributors [of stray load losses]". In many cases, manufacturing and design imperfections are controllable, and occur as a result of either inconsistent processes or as cost minimization. For example, aluminum is often chosen as the material for induction machine rotors because of its light weight and relatively cheap cost. However, cast aluminum rotors often contain "bubbles" in the cast segments, a typical problem associated with aluminum casting, which decrease the effective cross-sectional area of the rotor cage conductors. The effects of manufacturing imperfections on stray load losses will be discussed in detail in subsequent sections[5].

Understanding the origin and causes of stray load losses is not sufficient to drive industry to reduce or eliminate them. Quantifying the magnitude and effects of stray load losses is necessary for industry and academia alike in order to provide the motivation for their reduction.

Effects on performance and ratings

One of the most notable effects of stray load losses is excess heat production, but stray losses also affect other performance ratings. According to Jimoh [2], "the principle effects of stray load loss are heating of various machine components, loss of output torque, acceleration and retardation effects, lowered efficiency, and, as a practical consequence of these, derating of the machine". Losses are particularly important to industry, because losses translate into extra costs for no incremental benefit. In addition, these losses can affect the useful life of a machine in operation. It was noted by Jimoh [2][11] that stray load losses could cause a rise in the operating temperature of an induction motor by as much as 10°C, which is sufficient to halve the life span of the machine insulation.

The issue of stray load loss is particularly interesting to academia, not only because there is still relatively little known about it, but because of issues with allocation during

---

[5] Manufacturing imperfections are discussed in section 2.3.3.iv

the design stage. It is suspected that the actual allocation for stray load losses is far below what induction machines experience in operation. The issues of measurement and allocation are somewhat complicated, and will be addressed individually in subsequent sections below[6].

Methods of stray load loss allocation in design

A significant motivation for the study of stray load losses is to discover a universally accepted method of allocating them during the design stage. The fact that stray load losses exist is well accepted, although frustrating to many designers. Furthermore, it is also acknowledged that an accurate determination of the magnitude of the losses is practically unknown until after the motor is constructed. It was discussed above that one of the effects of stray load losses manifests in the form of additional heat generation. It is clear that at the design stage a good understanding of the likely temperature rise within an induction machine is necessary [6]. If the actual operating temperature of the machine is not accurately known during the design stage, the machine may not perform to the ratings as stated in the specifications, and the life of the machine may be compromised.

Since the actual magnitude of stray load losses is difficult to determine in general, different methods have arisen in order to include them at the design stage. In Britain, the standard allocation for all induction machines is stated as 0.5% of total power input. According to Glew [1], "this statement is the most challenged assumption in the

---

[6] Measurement techniques will be discussed in Section 2.2.1, and different allocation methods will be discussed in the following section

industry", because many authors believe it to be exceedingly erroneous. Even as far back as the 1960's, several authors including Chalmers, Bird, Christophides & Adkins, Oberettl and Schwarz from industry agreed that the allocation of 0.5% was a great understatement, and that actual stray load loss contributed greater than 1.0% of input power [19]. Schwarz published a survey of stray load losses in squirrel cage induction motors, addressing issues of stray load and no load losses, and recommended a provision of between 0.5% and 10% of the total losses for various small machines [6]. Bird challenged the 0.5% allocation by stating that stray load losses could be twenty times the standard allocation [2] agreeing with Shwarz's estimations. More recently, several authors [1][2][20] have also concluded that the actual stray load loss in a squirrel cage induction machine far exceeds the standard 0.5% allocation. Some authors have noted that in addition to potentially misleading the end user by understating stray load losses, a fixed allocation for stray load losses does not offer designers any motivation to discover methods of reducing or eliminating them [20].

Although the academic community is interested in increasing the machine efficiency by understanding and reducing stray load losses, industry is most interested in using a machine that performs to specification. If there is truth behind the assertion that many induction machines suffer from higher losses than originally accounted for, then as stated by Glew [1], "it is even more surprising that the figure of 0.5% should have been assigned in the first place and survived so long!". It is even more surprising that the 0.5% allocation has been used for so long simply because the calculated losses will almost always be smaller than the true losses due to manufacturing imperfections, particularly in smaller induction machines with skewed die-cast aluminum rotors [1].

In North America allocations for stray load losses at the design stage are based on various tests that attempt to determine the total losses of the machine after manufacturing. Several of the most common tests will be discussed in detail in subsequent sections[7], but despite the varying usefulness of these tests, allocations are often made based on the designers experience or past values. Indeed, the reliability or practicality of many of the tests is also suspect. It is easy to state that allocations are blindly applied either by a fixed percentage or by designer experience, but in practice it is most often some sort of intuitive compromise between the two. Unfortunately, the actual allocation used at the design stage is rarely founded on any sort of rational analytic basis [2].

Methods of reducing stray load losses

Although stray load losses have been a significant topic of research for decades, there has been limited progress in terms of reducing or eliminating them. One of the most significant reasons for their lack of reduction is due to the fact that several stray load losses originate as a result of an attempt to reduce other more well-known or significant losses in squirrel cage machines. For example, squirrel cage aluminum rotors are skewed in some machines to reduce stator slot harmonics, or cogging, but this skew is considered

---

[7] Tests to determine the actual losses after manufacturing will be discussed in section 2.2.1

to be a cause of inter-bar currents. Under ideal circumstances, the general concept of reducing any form of losses is quite simple and straightforward.

According to Jimoh [2], there are five suggestions for increasing the efficiency of an induction machine:

1. Reduction of losses in conductors
2. Reduction of losses in the end region
3. Reduction of harmonics
4. Reduction of losses due to industrial imperfection
5. Effects of skew and slot combinations

The losses caused by industrial imperfections, most prominently from insufficient rotor bar insulation, will be the core topic of this thesis.

2.1.4 Introduction to Inter-bar currents

Inter-bar currents are the most significant stray load loss occurring in uninsulated rotor bar construction squirrel cage induction machines as a result of manufacturing imperfection and design conditions. When power is applied to a squirrel cage induction machine, particularly as it is running under full load, a voltage is induced on the rotor resulting in a potential difference between adjacent rotor bars. If the rotor bar insulation, or the effective resistance, between the bars and the core is not perfect, a path will exist for current to circulate from bar to bar through the rotor iron causing unnecessary heating and performance degradation [2].

The phenomenon of inter-bar current tends to predominantly exist in smaller induction machines, where the rotor cages are die-cast. In many cases, the rotor bars are not insulated on smaller motors, or the insulation is damaged during fabrication when the rotor bars are moulded. Conversely, for larger induction machines, the rotor is assembled manually, and care is taken during fabrication and assembly to ensure proper insulation. Even so, inter-bar currents still exist in larger machines where the rotor bar insulation is damaged. Without insulation, there may be current from bar to bar through the rotor iron [21].

There has been a recent resurgence of interest in inter-bar currents, and researchers are finding their effects to be quite significant [22]. Recently, Nishizawa et al. [23] noted that inter-bar currents can represent as much as one third of the total stray load losses [10]. Inter-bar currents occur as a direct result of poor rotor bar insulation, or more specifically as a function of the effective inter-bar resistance. Inter-bar currents can exist immediately after manufacturing due to a failure in the fabrication process, or can begin to appear over time as the machine ages and the effective bar to bar insulation begins to deteriorate [10].

2.2 Determination of Stray Load Losses

Before discussing inter-bar currents directly, it is necessary to understand the methods used in industry to measure and quantify losses, and in particular stray load losses in induction machines. The most popular methods of measuring load losses will be presented in the subsequent sections, with particular focus on the relative advantages and disadvantages of each method. Following the theoretical review is a brief discussion on key difficulties related to stray load loss measurement in general.

2.2.1 Theoretical Review

A variety of methods have been developed for measuring the efficiency, or the losses, of rotating machines. The three most common tests used in North American to measure total machine losses are the input-output method, the pump-back method, and the reverse rotation test [2]. All three tests have advantages and disadvantages associated with them, but in general are all simple to apply and universal regardless of motor size. These methods tend to be defined by their ease of implementation, practicality, accuracy of results, and repeatability. It is mainly due to the simple application and relative accuracy of these three methods that they are used in industry, despite their shortcomings.

For example, two common methods of determining losses are the input-output method and the loss segregation method. The input-output method provides an accurate measurement of the total losses in an induction machine, although it is difficult to perform in to achieve high accuracy. The loss segregation method, although easy to implement for conventional losses, is less accurate than the input-output method, yielding only the known losses [2]. The two methods, when used in conjunction with each other, yield the stray load losses of an induction machine[8].

---

[8] The input-output method and the segregated losses are thoroughly discussed in section 2.2.1.ii

The work of Behdashti and Poloujadoff [24] represents an important contribution on appropriate models for the analysis of these losses, and it also includes a comprehensive bibliography of other works on this aspect [2].

i. Input-Output Method

One of the first methods used to determine the efficiency of a squirrel cage induction motor was the input-output method. The input-output method is conceptually quite simple, involving only physical experimentation and ordinary measurement equipment, and gives the total losses of a motor. Due to its simplicity and relative ease of implementation, the input-output test is commonly used to determine the total losses of induction machines. However, this method can only be used to measure the actual losses of a single induction machine after the motor has been constructed, offering no predictive value.

By means of experimentation, the mechanical output power of the rotor is measured using a dynamometer, and converted to equivalent units of electrical power. The electrical power input to the induction motor is also measured using a wattmeter. The total losses of the machine are simply calculated as:

$$P_{TotalLoss} = P_{Input} - P_{Output} \tag{2.1}$$

Using the loss segregation method the known losses of the machine are then measured. From a no-load test, the core losses (P_{Core}) and the friction and windage losses

($P_{F\&W}$) are found. A full load test at rated output power reveals the stator copper loss (P_{SCu}) and rotor copper loss (P_{RCu}). The total known power loss as determined by the loss segregation method is then:

$$P_{SegLoss} = P_{Core} + P_{F\&W} + P_{SCu} + P_{RCu}$$

The stray load losses are then:

$$P_{Stray} = P_{TotalLoss} - P_{SegLoss}$$

The input-output method offers the advantages of being effective at determining the total stray load losses in an induction machine and being simple to perform. However, it does not identify the individual components of stray load losses, only yielding the total load losses. One of the most significant drawbacks of this method is that it requires sensitive instrumentation to accurately determine the losses. Even with very precise measurements, this method often relies on the subtraction of two numbers very similar in magnitude and order to obtain the relatively small value of stray losses [2]. In addition, the output power is measured using a dynamometer and then converted to electrical power, creating an additional source for error.

ii. Pump-back Method [2]

The pump-back method works on the same principle as the input-output method for measuring the total losses of an induction machine. Using an “identical” induction motor coupled to the output shaft of the first machine, power is applied to the first machine and the input power is measured with a wattmeter. The second motor is operated as a generator, from which the output power is measured at the output of the generator terminals using a wattmeter. In addition, measurements are taken of the voltage and current at the input and the output, and the winding temperatures and slip of both machines are noted. From these measurements, the core, friction and windage, stator copper and rotor copper losses can be determined for both machines as an aggregate total.

Using the measurements described above, the total power loss can be calculated as the difference between the input power and output power. Similar to the input-output method, the total stray load losses for both machines together are found as the difference between the total power losses of the two machines and the losses from the loss segregation calculations. The stray load losses for an individual induction machine are then approximated as half of the total stray losses calculated above.

The pump-back method attempts to create a larger difference in the total power loss and the losses as calculated by the loss segregation method by doubling all the power drops, reducing the required sensitivity of the instrumentation. In most cases the pump-back method suffers the same numerical disadvantages as the input-output method [2]. Of greater significance is that the pump-back method calculates the losses of two machines under the assumption of each machine being identical. Subsequently, the individual machine losses are calculated as exactly half of the total losses, although it is statistically improbable that any two machines will be identical under the required operating conditions. The pump-back method still gives good insight into the average losses of an induction machine.

iii. Reverse Rotation Test

The reverse rotation method allows stray load losses to be measured with two separate tests. The first test measures a fundamental frequency component of stray losses in the stator, while the second measures stray load loss in the rotor. The test is implemented with the following two steps [2][3]:

(i) Stator stray losses – Rotor removed

With the rotor removed from the stator, a balanced three-phase current is applied to the stator winding. The input power applied is measured, and the stator I^2R losses are calculated using the applied current and the measured winding resistance. The stator stray loss is the difference between the input power and the stator I^2R loss,

$$P_{StrayStat} = P_{In} - I^2 R_{Stator} \tag{2.2}$$

Ware [25] suggested that the stator stray losses in equation 2.2 be measured at the input current,

$$I = \sqrt{I_1^2 - I_m^2} \tag{2.3}$$

where I_1 is the stator load current and I_m is the magnetizing current [2].

(ii) Rotor stray losses – Reverse rotation test

The stator is excited with a balanced poly-phase voltage, and the rotor is mechanically driven by an external drive at synchronous speed in the opposite direction of the air gap rotating magnetomotive force [2]. The mechanical power required to drive the rotor while the stator is excited (P_{RSE}) and the stator input power (P_i) are measured at the input current of equation 2.3. The power required to drive the rotor when the stator is not excited (P_{RSnE}) is also measured. The rotor stray loss is then calculated as:

$$P_{StrayRotor} = P_{RSE} - P_{RSnE} - P_i + P_{StrayStat} + 3I^2R_S \tag{2.4}$$

where R_S is the resistance of a stator phase winding.

The total stray load loss is calculated as the sum of the stator and rotor stray load losses:

$$P_{Stray} = P_{StrayStat} + P_{StrayRotor} = P_{RSE} - P_{RSnE} - P_i + 2P_{StrayStat} + 3I^2R_S \tag{2.5}$$

iv. Calorimetric Method [2][26][4]

The calorimetric method of testing machine efficiency is based on the assumption that all losses in an induction machine manifest in heat production. To implement this method, a motor is placed inside an insulated container with a heat exchanger. The motor is excited under various loading conditions allowing the losses to generate heat. The generated heat is removed from the insulated container via a cooling fluid which is cycled through the heat exchanger. When the machine reaches a steady state, and assuming that the calorimetric chamber is perfectly insulated, the heat removed from the enclosure will be equivalent to the heat generated by the machine losses.

Assuming an ideal calorimeter exists, the steady state power loss is given as [26]:

$$P_{loss} = m_{cool} \cdot \left[h_{out} \cdot T_{out} - h_{in} \cdot T_{in}\right] \tag{2.6}$$

where m_{cool} is the mass flow per second of coolant (kg/s)

h_x is the enthalpy of the coolant (J/kg)

T_{in} is the temperature of the coolant at the input $(^\circ C)$

T_{out} is the temperature of the coolant at the output $(^\circ C)$

Although the calorimetric method offers the potential to accurately calculate losses, there are several problems associated with it. Initially, the assumption must be made that all losses are manifest in the form of heat, which is not true in general. Secondly, perfect insulation and heat exchange are required to correlate the heat gain through the heat exchanger to the heat production of the motor. The finite thermal properties of materials prevent a perfectly insulated calorimetric chamber from being constructed, and losses occur in the transfer of heat from the chamber to the fluid in the heat exchanger. Additionally, fundamental to this method is the accurate measurement of both the input and output temperatures. As such, the type of coolant used is critical. The use of air as the coolant is cheapest and easiest, while allowing the calorimetric chamber itself to be used as a heat exchanger, although it offers lower precision. The use of water as a coolant achieves much higher accuracy, yet requires a heat exchanger located at the top of the chamber and a circulating fan. The location of the heat exchanger impedes the insertion of larger motors by hoist or crane [26], decreasing the practicality of this test, and the fan introduces an additional source of heat. The use of different types of coolants also poses environmental concerns with spillage and leaks.

In terms of actual measurement, this method assumes there are no heat gradients across the diameter of the heat exchanger's input and output piping. Different types of coolants provide better properties of equal heat distribution, but thermal gradients can never be completely eliminated. Thermal gradients are often neglected to simplify measurements and calculations, decreasing the accuracy of the measurements.

Determining when steady state has been achieved can be complicated because the chamber is completely sealed. The proper determination of steady state is critical, and is the source of many errors in measurement and prediction using this method. The exponential nature of the temperature rise generated by the induction motor theoretically requires that infinite time pass before steady state is reached. In practice, this is unnecessary, but the sensitive nature of the calorimeter can introduce large errors if measurements are taken before steady state is actually achieved. Adding to the uncertainty of when steady state is reached are the requirements of keeping the excitation and operating conditions consistent on the motor over the duration of the test. Ensuring the operating conditions remain constant is essential to reaching a steady state, and is critical in order to keep the generated losses constant and stabilize the heat generation.

As stated by Jimoh, the calorimetric method can only be practically applied to larger machines, which generate significant amounts of heat [2]. For smaller induction motors, the heat generation can be relatively small, increasing the influence of thermal losses in the calorimetric chamber and skewing loss measurements. In addition, the calorimetric method does not offer any insight or improvement on the separation of stray load losses from the total losses, or in identifying the individual components of stray losses, although it can provide an accurate measurement of total machine losses.

v. Analysis of torque

Some researchers, [7][1][27] noting the relationship between torques (parasitic torques) and stray load losses considered the analysis of torque as the most appropriate channel through which stray load losses could be studied and best understood [2].

2.2.2 Discussion

i. Difficulties in measuring Stray Load Losses in general

Direct measurements of stray load losses are virtually impossible because in many cases the losses exist in locations that are unknown or inaccessible by current technology and instrumentation. Additionally, each of the most common stray load loss tests has fundamental disadvantages and assumptions that decrease the credibility of load loss results. For example, the calorimetric method assumes that all heat generated is a result of induction machine losses. Practically, heat is also generated from the mechanics of the motor such as in the bearings, and slip rings if using a rotating stator machine.

ii. Difficulties in determining rotor losses in particular

Much of the current research and historical work has been performed on the stator, using inferences and analytical work to account for the rotor losses. This is mainly due to the fact that the rotor is rotating around a fixed stator, and buried within the stator mechanics, and is therefore difficult to instrument and access. Direct measurement of the rotor of a standard induction machine is possible through the use of commutation rings at the cost of decreased measurement accuracy and additional instrument noise. For this reason, rotor load losses are often either estimated as a function of stator load losses or neglected outright. For example, in Bousbaine, Low and McCormick's analysis [6], rotor iron losses were assumed to be negligible due to the low slip frequencies, relatively high cage bar/lamination insulation, and large cage bar cross-sectional area.

iii. Difficulties in separating different Stray Load Losses

Even if an accurate, quantifiable value for the total stray load losses could be determined, such as from an ideal input-output test, an analytical or practical method of separating the individual components of load losses does not exist. Most of the published work on individual stray load losses uses analytical approaches that are based on various hypotheses. Limitations of these hypotheses might give rise to incorrect results [28], particularly when studying individual components of stray load losses using experimental methods that yield total aggregate load loss.

2.3 Inter-Bar currents as a Stray Load Loss

Building on an understanding of the difficulties related to stray load loss measurement presented in Section 2.2, a compendium of author's analytical, mathematical and experimental work in the area of inter-bar currents is now offered. The section begins with a definition of inter-bar currents, and continues with a description of the main causes, with a brief outline of physical conditions and design parameters required for their existence. The section concludes with a detailed outline of the most prominent theoretical methods of calculating inter-bar currents.

2.3.1 Definition of Inter-bar Currents

In squirrel cage induction motors, inter-bar currents have become more important in the last few years because of their significant contribution to stray load losses. Inter-bar currents are an element of stray load loss in skewed rotor squirrel cage induction machines that manifest, as the name implies, as a current circulating between rotor bars. Current is allowed through the rotor iron around the circumference of the rotor as a result of insufficient rotor bar insulation [29]. Inter-bar currents reduce the performance of the motor, and most notably, have the effects of increasing the operating temperature of the rotor iron and altering the current distribution within the rotor cage bars.

Inter-bar currents are common in smaller[9] squirrel cage induction motors because it is often not financially viable or physically practical to insulate the rotor bars. For most small motors, insulation of the rotor bars requires a design compromise because of space limitations and performance requirements. Additionally, the contact region between the rotor bars and the iron core creates a relatively high resistance between adjacent bars. For many years this contact resistance was assumed to be sufficient to prevent inter-bar currents from circulating without insulation.

Typically, the design and manufacturing process of larger squirrel cage induction machines prevents inter-bar currents from circulating between the rotor cage bars. During the manufacturing stage, larger machines are assembled manually ensuring proper insulation of the rotor bars in most cases. However, despite concentrated care during manufacturing, inter-bar currents can still exist in large induction machines where the cage insulation is insufficient or damaged during assembly. Additionally, the rotor bar insulation can degrade over time as the motor ages, providing a path for inter-bar currents causing further degradation of the insulation.

Odok [13] and Christophides [8] were two of the first authors to derive simple analytical models describing the flow of inter-bar currents as well as determine their origins and effects. More recently, authors such as Yamazaki and Haruishi [9], Williamson and Smith [21] and Jimoh [18] have extended early works attempting to model these currents. The models used to calculate inter-bar currents, as well as

---

[9] Induction motors under 10kw are considered small

techniques to measure them experimentally will be discussed in detail in subsequent sections[10].

2.3.2 Causes and Effects of Inter-bar Currents

The occurrences of inter-bar currents in squirrel cage induction motors are a consequence of imperfect rotor cage insulation, founded in either design neglect or manufacturing imperfection. Under normal operating conditions, a potential difference exists across any two adjacent rotor bars, and without perfect insulation, a path can exist for current to circulate along the circumference of the rotor. There are currents from bar to bar across the bar-iron contact region and through the rotor iron laminations generating excess heat, causing the existing bar insulation to deteriorate, and reducing motor output torque. Additionally, there are no inter-bar currents through the end-ring path, thereby creating a non-uniform current distribution along the length of the rotor bar [5].

Christophides [8] analytically presented that inter-bar currents only have the potential to exist in induction machines with skewed rotors. He postulated that the effects of these currents are closely related to both the amount of bar insulation and the skew angle. Christophides concluded that for a well-insulated machine, the load losses generated by inter-bar currents decrease as the skew increases. Conversely, for a poorly insulated rotor, the load loss decreases as the skew decreases. Christophides further postulated that inter-bar currents could not exist in a rotor without skew, regardless of the inter-bar

---

[10] The most prominent theoretical methods of calculating inter-bar currents are discussed thoroughly in section 2.3.5

resistance or presence of rotor bar insulation. Williamson and Smith [21] discovered that under starting conditions the presence of inter-bar currents drives the performance of a skewed rotor machine towards that of an unskewed rotor.

2.3.3 Parameters affecting Inter-bar Currents

Several key physical and design parameters affect the existence and magnitude of inter-bar currents. The most significant physical parameters are the inter-bar contact resistance, the presence of bar insulation, and the effective end-ring impedance. In addition to the physical parameters, two main design decisions also greatly affect inter-bar currents: the choice of a skewed or un-skewed rotor cage and the choice of the rotor cage manufacturing method.

i. Inter-bar Resistance/Contact resistance

In squirrel cage induction machines with skewed rotors, the presence and magnitude of inter-bar currents is partially determined by the effective resistance between rotor bars. A potential difference exists across adjacent rotor bars during machine operation, and there may be inter-bar currents if a low-resistance path exists. The magnitude of the inter-bar resistance is largely determined by the presence or absence of rotor bar insulation, the contact region between the rotor bars and rotor iron, and the temperature of the rotor iron. The effects of the contact region, rotor bar insulation and rotor operating temperature on inter-bar resistance has warranted the research of many authors, leading to several analytical models of the inter-bar resistance[11].

In addition to developing models to predict inter-bar currents, developing methods of experimentally measuring the true value of inter-bar resistance for comparison to the calculated values has proven difficult for researchers as well. Most measurement techniques are destructive in nature, requiring the removal of the rotor end rings to prevent their relatively low resistance from affecting the inter-bar resistance measurements. For example, the process used to remove the end rings invariably places stress on the contact regions between the rotor iron and rotor bars. The stress has the potential to disrupt the physical integrity of the rotor altering the inter-bar resistance.

The inter-bar resistance is considered to be a combination of the resistance of the rotor iron laminations and the contact resistance between the rotor bar and rotor iron [30]. Since the rotor iron has a finite, relatively low resistance, the contact junction between the rotor iron and the rotor bar contributes the majority of the effective inter-bar resistance. According to Dorrell et. al. [5], "the boundary resistance[12] is about 67 times higher than the resistance through the core". The actual contact region is composed of microscopic interstices and small contact points resulting from the imperfect crystalline structure of the materials, which reduce the effective contact area. In addition, a small layer of oxide and dust generated during the manufacturing and assembly processes

---

[11] Models derived to analytically calculate inter-bar currents will be discussed in detail in section 2.3.5

[12] The boundary region is defined as the junction between two different materials, that lack perfect contact with each other

creates a film of insulation, further reducing the effective metal-to-metal contact area and increasing the inter-bar resistance.

The actual contact area between the rotor bar and rotor iron is dependant on both the rotor skew and the slot type. Assuming a constant slot type along the length of the bar, a larger skew will increase the contact area of the rotor iron and the rotor bars. Additional to the rotor skew, different slot shapes and slot dimensions will affect the total contact area between the iron laminations and the rotor cage.

Temperature variations in the rotor can also have a significant effect on the effective inter-bar resistance. The resistance of the rotor iron increases as the temperature rises, causing the iron to expand resulting in an increase in the tightness of fit of the rotor laminations in the rotor slots and consequently an increase in the effective contact area. Despite the thermal expansion of the rotor iron, it was found by Dorrell et. al. [5] that as the temperature increased the inter-bar resistance also increased. Dorrell et. al. concluded that inter-bar resistance is dominated by the boundary resistance, which is not conclusively related to the tightness of fit. Furthermore, Gersh et. al. [30] determined that the inter-bar resistance is not constant along a rotor bar or across all rotor bars, which supports the belief that inter-bar resistance is dominated by the contact resistance.

ii. Rotor Cage Skew

Rotor skew was introduced in die-cast rotors of small induction machines to reduce high-frequency torque ripple and acoustic noise arising from slotting effects. Skewing the rotor exactly one stator slot will attenuate the electro-motive forces induced in the rotor cage due to stator slotting [31]. Although a skewed rotor is implemented in induction machines to reduce undesirable effects such as noise, and increase performance by reducing known losses, certain other losses are generated or enhanced by this design choice. This is exemplified by McClay and Williamson [31] who stated, "it is well known for example that skew promotes inter-bar currents and also causes an axial redistribution of the air-gap flux".

The research of Carlson et. al. [29][22] illustrates that in a squirrel cage induction machine with a skewed rotor, only perfect insulation of the rotor bars can prevent inter-bar currents. In all practical cases, for small induction machines, where the majority of rotors are die-cast, perfect insulation of the rotor bars is impossible. Consequently, for all practical skewed rotor induction machines, the losses created as a result of inter-bar currents cannot be avoided.

The understanding that inter-bar losses cannot be avoided in skewed rotor induction machines has focused the attention of researchers towards understanding the effects that both inter-bar resistance[13] and rotor skew have on inter-bar losses. Heller and Joki [32], extending the analytical work of Christophides [8], hypothesized that for low values of inter-bar resistance losses are proportional to the square of the skew, while for large values of resistance, losses are inversely proportional to the square of the skew [2].

Odok's [13] theoretical results assert that inter-bar currents cannot exist in the rotor of an induction machine without rotor skew if the end ring impedance is negligible. This

---

[13] Inter-bar resistance was thoroughly discussed in the preceding section 2.3.3.i

holds true even if the inter-bar resistance is finite, and paths exist for inter-bar current to circulate. However, although some authors consider the end ring impedance to be negligible to simplify calculations, in practice the end ring has finite impedance. Consequently, Odok [13] postulated that inter-bar currents can exist in a rotor without skew if the end ring impedance is not negligible.

iii. Bar Insulation

Insulating the rotor cage in a squirrel cage induction machine is a good method of reducing or eliminating inter-bar currents. However, there are difficulties and impracticalities associated with insulating the rotor bars sufficiently to eliminate inter-bar currents. Materials serving as good electrical insulators are typically effective thermal insulators as well. Insulating the rotor bars to decrease inter-bar current losses may also thermally insulate the rotor bars, causing a significant increase in the operating temperature of the rotor. Furthermore, the rotor bar insulation of die-cast rotors would need to be applied to the iron core before the moulding process. The insulation would need to withstand the extreme temperatures of the molten metal throughout the moulding process to properly insulate the rotor bars from the iron core.

For larger induction motors rotor bar insulation is more financially viable and feasible to apply during manufacturing. Larger induction machine rotors are commonly fabricated and assembled manually, in contrast to small induction motor rotors, which are mass-produced and normally die-cast. In a large induction motor, the rotor cage can be properly insulated from the iron core, and the insulation can be maintained during assembly. Even with proper care during assembly, it is difficult to perfectly insulate the rotor bars. In fabricated rotors contact between the bars and the iron is more localized, occurring where the insulation has been damaged, or degraded over time, and the inter-bar currents are more irregular as a result [30].

Despite the inherent difficulties in insulating the rotor bars for all sizes of induction motors, "industrial experience confirms the better performance of induction motors with insulated rotor bars. When the rotor bars are not insulated, inter-bar currents present in the rotor structure cause performance degradation" [29]. The difficulties encountered when directly insulating the rotor cage from the core have generated interest in developing different techniques to increase the inter-bar resistance[14].

iv. Manufacturing Method

The rotor of a squirrel cage induction machine is manufactured either by die-casting or fabrication and assembly, depending on the size of the motor and the quantity required. The majority of large induction motors are assembled mainly due to physical dimension. The practicality of casting large rotors is suspect, due to both the physical size, and problems related to consistency when casting large volume pieces. Larger induction motors are often designed and built according to specific industrial needs at low purchase volumes, warranting the additional cost of fabrication and assembly. For low volume

---

[14] Techniques and methods of increasing the inter-bar resistance, or equivalently reducing the inter-bar currents will be thoroughly discussed in section 2.3.3.iv

production, the capital investment involved in creating moulding equipment and automated processes for larger induction machines is often not financially feasible.

Conversely, the large majority of small induction machine rotors are cast to ensure repeatability in the production process and reduce production costs. Small induction machines are commonly mass-produced for general-purpose applications, rationalizing the use of die-casting to reduce unit costs at the sacrifice of flexibility. By nature of the casting process, a thin layer of oxide typically forms between the rotor bars and the iron core acting as an insulator, but it is typically insufficient to insulate the bars enough to eliminate inter-bar currents. Directly insulating the rotor iron from the cage bars during the casting process is difficult as well, because the insulation must withstand the extreme temperature as the molten metal is poured into the mould.

To overcome problems associated with insulating the rotor bars from the iron laminations in cast rotors, different methods have been developed to try and increase the inter-bar resistance instead. For example, after the moulding process, the rotors are either air cooled or quenched in a cooling medium. Air-cooling is economical, easy to implement, and requires little capital investment, yet studies have shown the benefits of quenching the rotor to reduce losses, particularly inter-bar current losses. Rapidly cooling the rotor after moulding tends to cause the cage bars to crack away from the iron core slightly, decreasing the contact area between the rotor bars and the iron core, effectively increasing the inter-bar resistance. Williamson, Poh and Smith's [12] experimental results have also confirmed that quenching does indeed increase bar-to-bar resistance, by approximately one order of magnitude.

Despite the popularity of die-cast rotors used in small induction motors, casting the rotor also introduces other manufacturing imperfections, such as bubbles in the cast members and weak points where metal alloys are used and homogeneity is not assured. These limitations are almost always offset by a significant decrease in manufacturing cost as a result of standardization and economies of scale achieved with casting and moulding.

2.3.4 Theoretical Review: Methods of Calculating Inter-bar Currents

A fundamental requirement to efficiently design an induction motor is the ability to predict stray load losses during the design stage. Rossmaier derived several expressions analytically modeling various components of stray load loss. In reference to inter-bar currents, several authors have developed analytical methods for calculating or modeling inter-bar currents. Many recent techniques and approaches expand on historical concepts developed during the infancy of inter-bar current investigation. For example Odok [13][15] later expanded on Rossmaier's work, focusing specifically on inter-bar currents. Other authors such as Christophides [8][16], and Sub Rao and Butler [14] derived more succinct expressions. More recently, authors such as Carlson et. al. [10][22][29], Yamazaki and Haruishi [9], and Ho et. al. [28] developed models to calculate cross-bar currents using a 2-D and 3-D Finite Element Method[17]. Other authors, such as Jimoh [11][18] have developed thermal models to predict stray load losses and inter-bar currents[18].

---

[15] Odok's derivations are outlined in section 2.3.4.i

[16] Chrisophides expressions for inter-bar currents are discussed in section 2.3.4.ii

[17] Current 2-D and 3-D finite element models are described in section 2.3.4.iii

[18] Thermal models are discussed in section 2.3.4.iv

i. Odok's Expression

Adnan Odok [13] was one of the first authors to derive a simple expression relating the inter-bar currents to the bar currents in squirrel cage induction motors without insulated rotor bars. Odok began his analysis with the currents induced in the rotor by the various harmonics of the stator field, including the cross currents between adjacent rotor bars. Figure 2.1 shows a vector representation of both the bar currents and the inter-bar currents in a section of a squirrel cage rotor as defined by Odok.

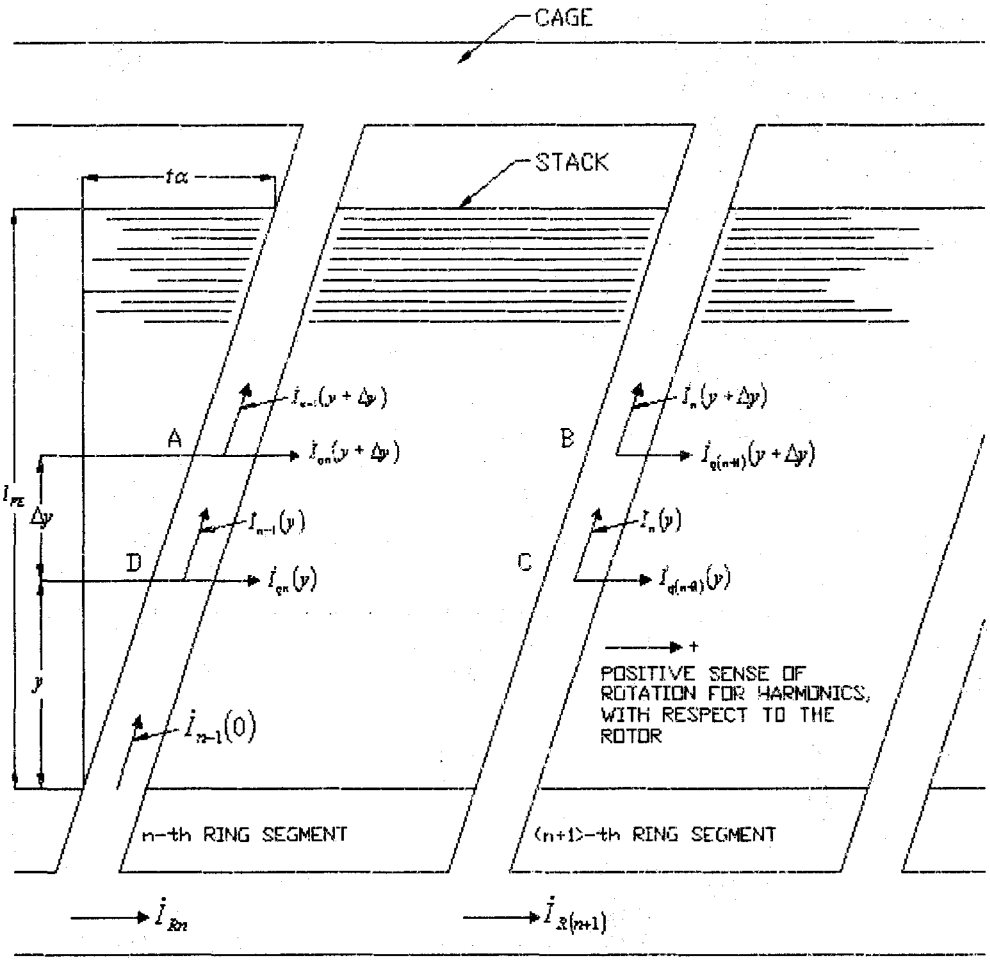

Figure 2.1: Cross-section of a Rotor with Bar and Inter-bar Currents

For his derivation, Odok defines the symbols:

$\dot{I}_n(y)$ = bar current in the n^th^ bar at distance y from one end of the rotor stack

$\dot{Z}_{ll}$ = $r_l + jX$ = bar impedance per unit length

$\dot{I}_{qn}(y)$ = cross current per unit length in the n^th^ rotor segment

$\dot{Z}_{q_q}$ = $r_q + jX$ = cross-impedance per unit length between adjacent rotor bars

δ = phase angle between two adjacent rotor bars

$\dot{V}$ = voltage drop

$\dot{E}$ = induced voltage

Applying Kirchhoff's second law to the mesh ABCD in Figure 2,1 yields:

$$\sum_{ABCD}\dot{V} = \sum_{ABCD}\dot{E}$$

The sum of the voltage drops around the path ABCD is:

$$\begin{aligned}\sum_{ABCD}\dot{V} &= \dot{I}_{n-1}(y)\dot{Z}_l\Delta y + \dot{I}_{qn}(y+\Delta y)\Delta y\frac{\dot{Z}_q}{\Delta y} - \dot{I}_n(y)\dot{Z}_l\Delta y - \dot{I}_{qn}(y)\Delta y\frac{\dot{Z}_q}{\Delta y} \\ &= \left[\dot{I}_{n-1}(y) - \dot{I}_n(y)\right]\dot{Z}_l\Delta y + \frac{d\dot{I}_{qn}}{dy}\Delta y\dot{Z}_q\end{aligned} \tag{2.7}$$

Using the symmetry of the rotor, Odok further defined relations between the currents of adjacent bars and adjacent rotor segments as:

$$\dot{I}_{q(n+1)}(y) = \dot{I}_{qn}(y)e^{-j\delta} \tag{2.8}$$

$$\dot{I}_{n-1}(y) = \dot{I}_n(y)e^{-j\delta} \tag{2.9}$$

Applying Kirchhoff's first law to point B:

$$\frac{d\dot{I}_n}{dy} = \dot{I}_{qn}\left(1 - e^{-j\delta}\right) = 2j\sin\frac{\delta}{2}e^{-j\delta/2}\dot{I}_{qn}$$

Solving for the inter-bar current:

$$\dot{I}_{qn} = \frac{d\dot{I}_n}{dy}\frac{e^{j\delta/2}}{2j\sin\delta/2} \tag{2.10}$$

Taking the first derivative of (2.10) with respect to y gives:

$$\frac{d\dot{I}_{qn}}{dy} = \frac{d^2\dot{I}_n}{dy^2}\frac{e^{j\delta/2}}{2j\sin\delta/2} \tag{2.11}$$

Substituting (2.11) and (2.9) into (2.7) gives an expression for the voltage drops:

$$\begin{aligned}\sum_{ABCD}\dot{V} &= \left[\dot{I}_n(y)e^{-j\delta} - \dot{I}_n(y)\right]\dot{Z}_l\Delta y + \frac{d^2\dot{I}_n(y)}{dy^2}\frac{e^{j\delta/2}}{2j\sin\delta/2}\Delta y\dot{Z}_q \\ \sum_{ABCD}\dot{V} &= \dot{I}_n(y)2j\sin\delta/2e^{j\delta/2}\dot{Z}_l\Delta y + \frac{d^2\dot{I}_n(y)}{dy^2}\frac{e^{j\delta/2}}{2j\sin\delta/2}\Delta y\dot{Z}_q\end{aligned} \tag{2.12}$$

The induced voltage in the bar element CB from the v^{th} stator field harmonic B_{lv} is

$$E_{CB} = \frac{1}{\sqrt{2}}B_{1v\max}\upsilon_v\Delta y \tag{2.13}$$

where

$$B_{1v\max} = \sqrt{2}\frac{\mu_0 m_1\dot{I}_{1Ph}Z_1k_{wv}}{g\pi p v}$$

μ_0 = magnetic permeability of vacuum or air

g = air gap

m_1 = primary-phase number

I_{1PH} = primary-phase current

Z_1 = number of series conductors per phase in the primary

p = number of poles for the main field

k_{wv} = winding factor of the primary winding for the v^{th} harmonic

$\upsilon_v = \frac{2t_p f_{2v}}{v}$ = the relative velocity of the v^{th} harmonic with respect to the stator

t_p = the pole pitch for the main field

f_{2v} = frequency of the induced voltage in the rotor

Substituting B_{1max} into (2.13)

$$E_{CB} = \frac{\mu_0 m_1 \dot{I}_{1Ph} Z_1 k_{wv}}{g\pi p v} \frac{2t_p f_{2v}}{v} \Delta y \tag{2.14}$$

Using the relations

$$\dot{E}_{DA} = \dot{E}_{CB} e^{j\delta}$$

$$\ddot{\upsilon}_v = (m_1 Z_1 k_{wv})/S_2 \qquad \text{(turns ratio)}$$

$$X_{2hv} = 2\frac{\mu_0}{\pi}\frac{S_2 t_p}{g p v^2} f_{2v} \quad \text{(magnetizing reactance per unit length of rotor bar)}$$

Substituting into (2.14), Odok derived an equation for the sum of the induced voltages

$$\sum_{ABCD} \dot{E} = jX_{2h} 2j\sin(\delta/2) e^{j\delta/2} \Delta y \dot{I}_{1PH} \ddot{\upsilon}_v e^{j\alpha y} \tag{2.15}$$

In (2.15), Odok uses the term $e^{j\alpha y}$ to compensate for the effects of skewing on the induced voltage. He defines α as the skew per unit stack length, measured as an electrical angle for the v^{th} harmonic. Setting equation (2.12) equal to (2.15) gives a differential equation for the bar current

$$\frac{d^2 \dot{I}_n(y)}{dy^2} \dot{Z}_q^* + \dot{I}_n(y) \dot{Z}_l = \dot{E}_1 e^{j\alpha y} \tag{2.16}$$

where $\dot{Z}_q^* = \dot{Z}_q / 4\sin^2 \delta/2$

$$\dot{E}_1 = jX_{2hv} \dot{I}_1 \ddot{\upsilon}_v$$

Odok derives the voltage across adjacent rotor bars at an arbitrary point y along the length of the bars, parallel with the end rings as

$$\dot{V}(y) = \dot{I}_{qn}(y) \dot{Z}_q = \frac{d\dot{I}_n}{dy} \dot{Z}_q \frac{e^{j\delta/2}}{2j\sin\delta/2} \tag{2.17}$$

Solving equation (2.16) using the boundary conditions at $y=0$

$$\dot{I}(y=0)=\dot{I}_1 \quad \text{and} \quad \dot{V}(y=0)=\dot{V}_1$$

yields

$$\dot{V}_v^*(y)=\dot{V}_{1v}^*\cosh\gamma y-\dot{I}_{1v}\dot{Z}_v\sinh\gamma y+\left(\frac{\dot{Z}_v\sinh\gamma_v y}{\dot{Z}_{qv}^*\beta_v^2}+\frac{j\alpha_v\cosh\gamma_v y}{\beta_v^2}-\frac{j\alpha_v e^{j\alpha_v y}}{\beta_v^2}\right)\dot{E}_{1v} \tag{2.18}$$

$$\dot{I}_v^*(y)=\dot{V}_{1v}^*\frac{\sinh\gamma_v y}{\dot{Z}_v}+\dot{I}_{1v}\dot{Z}_v\cosh\gamma_v y-\left(\frac{\cosh\gamma_v y}{\dot{Z}_{qv}^*\beta_v^2}+\frac{j\alpha_v\sinh\gamma_v y}{\dot{Z}_v\beta_v^2}-\frac{e^{j\alpha_v y}}{\dot{Z}_{qv}^*\beta_v^2}\right)\dot{E}_{1v} \tag{2.19}$$

where $\dot{Z}_v=\sqrt{\dot{Z}_{lv}\dot{Z}_{qv}^*}$ (surge impedance)

$\dot{\gamma}_p=\sqrt{\dot{Z}_{lv}/\dot{Z}_{qv}^*}$ (propagation constant)

Odok asserted that in most practical cases the end-ring impedance is sufficiently small in comparison to the inter-bar resistance, setting it to zero for his calculations

$$\dot{V}^*(y=0)=\dot{V}^*(y=l_{FE})=0 \tag{2.20}$$

Two rotor cage configurations were considered by Odok with particular reference to inter-bar currents. The first scenario was a rotor with no skew and the second was a rotor with a skew relative to the stator slots.

No Rotor Skew

Under the constraints of (2.20), equations (2.18) and (2.19) yield

$$\dot{I}_v(y)=\frac{\dot{E}_1}{\dot{Z}_l}=\text{constant}$$

In equation (2.10), Odok derives a relationship between the bar and inter-bar current as

$$\dot{I}_{qn} = \frac{d\dot{I}_n}{dy} \frac{e^{j\delta/2}}{2j\sin\delta/2} \rightarrow \dot{I}_q(y) \propto \frac{d\dot{I}_n(y)}{dy} = 0 \tag{2.21}$$

Odok concluded for the case where the rotor cage has no skew relative to the stator slots and the end-ring impedance is negligible, inter-bar currents do not exist.

Skewed Rotor

For a rotor with a skew relative to the stator slots, Odok further defined two possible cases. The first case occurs if high inter-bar impedance exists between adjacent rotor bars, where Odok derives the losses as

$$\frac{4\left|\overline{BC}\right|^2 \sin^2\delta/2}{\dot{Z}_q^2} r_q \propto \frac{\left|\overline{BC}\right|^2}{r_q^*} \tag{2.22}$$

Equation (2.22) illustrates that reducing the cross voltages BC will reduce the losses, which can be accomplished by increasing the rotor skew. According to Odok, increasing the skew N times will reduce the inter-bar losses proportional to the square of the skew $1/N^2$.

To model the case where the inter-bar impedance is low, Okok examines the extreme case where the cross-bar resistance is zero, and assumes the current distribution remains unchanged for low finite values. With zero cross-bar resistance, the rotor can be divided into independent slices, thus Odok derives the bar current for each slice at position y as:

$$\dot{I}(y)=\frac{\dot{E}_1 e^{j\alpha y}}{\dot{Z}_1}$$

Solving for the inter-bar current using equation (2.10)

$$\dot{I}_{qn}=\frac{d\dot{I}_n}{dy}\frac{e^{j\delta/2}}{2j\sin\delta/2}=\alpha\frac{\dot{E}_1 e^{j\alpha y}}{\dot{Z}_1}\frac{e^{j\delta/2}}{2\sin\delta/2} \tag{2.23}$$

If the inter-bar losses are assumed to be primarily resistive, then the losses will be proportional to the square of the inter-bar current. According to equation (2.23), the inter-bar current is directly proportional to the skew angle α. Odok concluded that for the case of low inter-bar resistance, the inter-bar losses are directly proportional to the square of the skew.

ii. Christophides Simplified Model for Inter-bar Losses

Christophides, basing his methodology on the earlier works of Rossmaier and Odok [13][19], derived a more simplified model for analytically calculating losses due to inter-bar currents. Applying Kirchhoff's second law to the path ABCD of Figure 2.2

$$E_{DA}=I_{bvn}Z_b dy-\frac{\partial^2 I_{bv}}{\partial y^2}\left[\frac{r_{bb}}{4\sin^2\delta/2}\right]dy \tag{2.24}$$

where

I_{bvn} = bar current in bar n

Z_b = bar resistance per unit length

r_{bb} = inter-bar resistance per unit length

---

[19] Odok's work is discussed in detail in the previous section

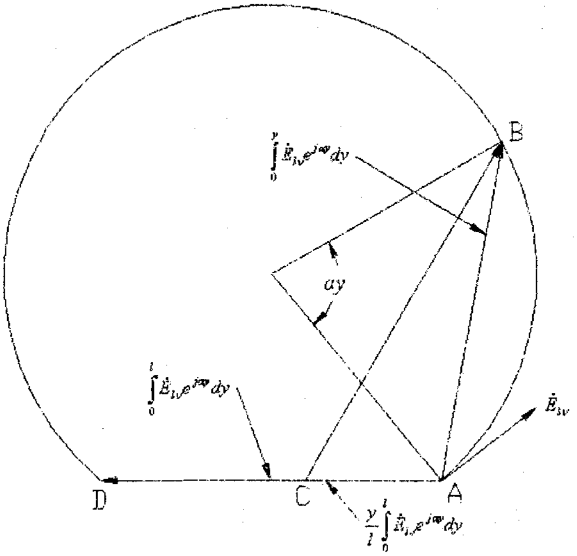

Figure 2.2: Induced Voltages and Drops in Rotors with High Crosspath Impedance

In equation (2.24), E_{DA} is the voltage induced in section DA of the rotor bar, given by

$$E_{DA} = E_0 \Delta y e^{j\alpha y}$$

where

$$E_0 = \frac{\mu_0 \dot{I}_{1Ph} Z_1 k_{wv} 2 m_1 t_p f_{2v}}{g \pi p v^2} \tag{2.25}$$

From equations (2.24) and (2.25), Christophides solves for r_{bb}

$$r_{bb}^{'} \frac{\partial^2 I_{bv}}{\partial y^2} = I_{bv} Z_{bv} - E_0 e^{j\alpha y} \tag{2.26}$$

where

$$r_{bb}^{'} = \frac{r_{bb}}{4 \sin^2 \delta/2}$$

The solution to equation (2.26) is then

$$I_{bv} = A\cosh\gamma_v y - B\sinh\gamma_v y + \frac{E_0 e^{j\alpha y}}{\left(Z_{bv} + \alpha_v^2 r_{bb}'\right)} \tag{2.27}$$

In equation (2.27), Christophides solves for the constants A and B using the condition that at $y = \pm l/2$ the inter-bar voltage is $V_{bb}' = 0$. The total losses in the rotor caused by the v^{th} stator harmonic are then given by

$$P_{2v} = S_2 \,\mathrm{Re}\left\{ \int_{-l/2}^{l/2} I_{bv} E_{bv}^{*} dy \right\} \tag{2.28}$$

where E_{bv}^{*} is the conjugate of the voltage E_{bv}. The equation for the total losses in the rotor due to inter-bar currents is found by integrating equation (2.28) and yields

$$P_{2v} = \frac{E_{0v}^2 S_2}{r_{bb}'} \mathrm{Re}\left\{ \frac{1}{\alpha_v^2 - \gamma_v^2} - \frac{2\alpha_v^2}{\left(\alpha_v^2 + \gamma_v^2\right)^2} \frac{\cosh\gamma_v l - \cosh\alpha_v l}{\gamma_v \sinh\gamma_v l} \right\} \tag{2.29}$$

Using equation (2.29), Christophides develops a simplified model of the power loss due to inter-bar currents for two possible cases: low inter-bar resistance and high inter-bar resistance.

Low Inter-bar Resistance

In the scenario where the inter-bar resistance is low enough that

$$\alpha_v^2 << \left|\gamma_v^2\right|$$

or equivalently

$$\left|\frac{Z_{bv}}{r_{bb}'}\right| << \alpha_v^2$$

and

$$\gamma_v \rightarrow \infty$$

equation (2.29) can be simplified by using the relationship

$$\sinh \lambda_v l = \cosh \lambda_v l >> \cos \alpha_v l$$

The total losses generated by inter-bar currents in the rotor, modeled by equation (2.29), then simplifies to

$$P_{2v} = E_{0v}^2 S_2 \operatorname{Re}\left\{ \frac{1}{Z_{bv}} + \frac{2\alpha_v^2 r_{bb}'}{\gamma_v Z_{bv}^2} \right\} \tag{2.30}$$

High Inter-bar Resistance

Christophides defines a case where the inter-bar resistance is considered high if the subsequent relationships are true

$$\alpha_v^2 >> \left|\gamma_v^2\right|$$

or equivalently

$$r_{bb}' >> Z_{bv}$$

and

$$\sinh \gamma_v l \rightarrow \gamma_v l$$
$$\cosh \gamma_v l \rightarrow 1$$

If the above conditions exist, Christophides simplifies expression (2.29) as

$$P_{2v} = E_{0v}^2 S_2 \operatorname{Re}\left\{ \frac{1}{\alpha_v^2 r_{bb}'} + \frac{r_b}{\left|Z_{bv}\right|^2} \left(\frac{\sin \alpha_v l/2}{\alpha_v l/2} \right)^2 \right\} \tag{2.31}$$

Christophides notes that in equation (2.30), the first term represents the losses due to inter-bar currents since it contains $r_{bb}^{'}$, while the second term represents the losses generated by the harmonic currents in the bars.

iii. 2-D and 3-D Finite Element Method (FEM) Models

The magnetic field distributions of unskewed rotor induction motors can be accurately modeled using a two-dimensional time stepping finite element method because of recent advances in numerical methods and computational ability. However, since it is widely accepted that introducing rotor skew can reduce some conventional losses in an induction motor, two-dimensional (2-D) multi-slice time stepping finite element methods (FEM) have been developed to study the distribution of the magnetic fields in skewed rotor machines. Carlson et al. [22][29] have used a methodology based on 2-D FEM in conjunction with the Circuits Theory (Independent Currents Method) to model and analyze inter-bar currents in skewed rotor induction motors.

Ho, Fu and Wong [28] have extended the 2-D FEM models to a 3-D time stepping FEM model to more accurately model inter-bar currents, rotor movements and other non-sinusoidal quantities, stating that 2-D FEM models cannot accurately represent inter-bar currents. However, three-dimensional FEM models suffer in execution because of their high computational requirements. Yamazaki and Haruishi [9] have developed a combination 2D-3D model to utilize the advantages of a 3-D model in analyzing inter-bar currents and end effects, while reducing computational requirements for other simpler analysis using 2-D FEM where possible. Both the 2-D and 3-D FEM models suffer based on the fact that they rely heavily on computation and mathematical modeling, but are difficult to test experimentally.

iv. Calculating Inter-bar Resistance

Most mathematical expressions modeling inter-bar currents all assume that the equivalent resistance between adjacent bars is known. However, the measurement of bar-to-bar resistance can be difficult for three main reasons [5][20]:

1. The bar-to-bar resistance is often the same order of magnitude as the bar resistance itself
2. The implicit underlying assumption that the bar-to-bar contact resistance is uniform along the length of each bar
3. The rotor must be physically destroyed to remove the end-rings

According to Carlson et. al. [29], “the measurement of the rotor transversal resistance is without any doubt the challenge for the study of the problems associated to inter-bar currents”. Most conventional methods of experimentally measuring inter-bar resistance require the end-rings to be carefully machined off ensuring that the contact resistance has not been damaged as a result of the machining process. Once the end-rings have been removed, a DC current is injected into a single rotor bar and removed from an adjacent bar, while the DC voltage drop across the two bars is simultaneously measured [12]. This method requires extremely sensitive measurement instrumentation because the measurements must be performed with low currents to avoid damaging the bar-iron contact resistance yielding a small voltage differential across adjacent bars. It is almost impossible to obtain experimentally the value of the inter-bar resistances because their magnitudes are very low, in the order of the measuring instruments precision [10].

Despite the difficulties presented in measuring the inter-bar resistance, a true average value of the inter-bar resistance is necessary to predict inter-bar currents using most analytical methods. Several authors have chosen an arbitrary value of 40μΩ for the inter-bar resistance to be used in calculations; a value based on simple experimentation and educated approximation.

As discussed in Section 2.3.3, inter-bar resistance is predominantly a contact phenomenon, indicating that the contact area between the aluminum rotor bars and the laminated iron core is a significant consideration. Several authors have developed different equations to calculate the contact area between the rotor bars and the rotor iron. According to Williamson, Poh and Smith [12], the contact area is determined by the manufacturing method and skew angle. Each individual lamination has a finite thickness with the slot side of the laminations existing orthogonal to the plane of the lamination as a result of the process of punching, shown in Figure 2.3.

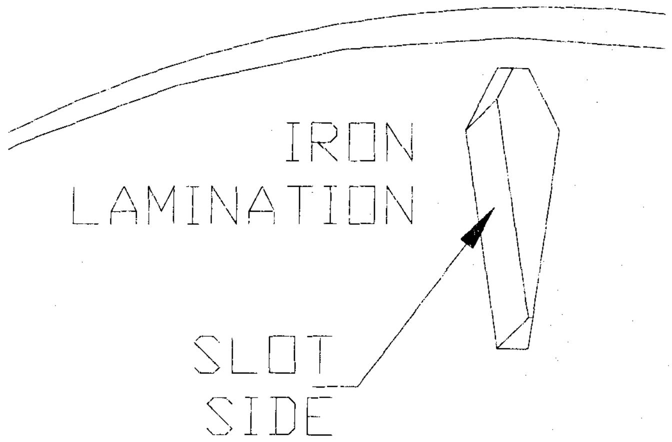

Figure 2.3: Slot Side of Iron Laminations

To create the rotor core the iron laminations are stacked, with each consecutive lamination rotated slightly to provide the required rotor skew. The result is that the slot side of each lamination contacts the rotor iron as shown in Figure 2.4, increasing the contact surface area with an increase in skew.

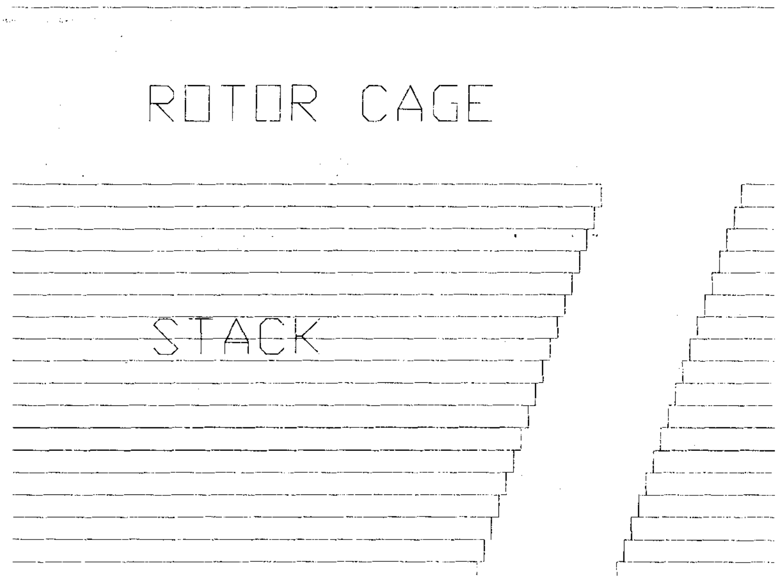

Figure 2.4: Bar-Iron Contact Area

According to Williamson, Poh and Smith [12] the total inter-bar contact area is then:

$$A = K \cdot S \cdot \left(1 + \frac{\gamma d}{2t}\right) \tag{2.32}$$

where K = a constant that depends on the shape of the slot

S = slot periphery (meters)

γ = angular displacement of adjacent laminations (radians)

t = lamination thickness (meters)

d = outer diameter of rotor (meters)

Gersh, Smith, and Samuelson [30] developed a simpler expression for the inter-bar contact area:

$$A = C_{bar} \cdot w \cdot n \cdot (1 + \tan(\alpha)) \tag{2.33}$$

where α = skew angle in degrees

C_{bar} = bar periphery

w = lamination width

n = number of laminations

Chapter 3

Motivation for Study

Much of the current research in the area of stray load losses, and particularly with respect to inter-bar currents, relies on theoretical calculations and mathematical modeling to predict or calculate the magnitudes of these losses. Direct measurement and instrumentation of inter-bar currents is difficult to facilitate because the rotor and drive shaft spin relative to the fixed stator and housing. This requires that any instruments or measuring tools affixed to the rotor must be commutated through slip rings or other similar devices before connection to an acquisition system. In most cases, the magnitude of signals generated by measuring instruments such as thermocouples and current transducers are very small, making direct measurements of voltages and currents from the rotor very sensitive. Passing these measurements through slip rings can generate significant noise, which may destroy low voltage readings or generate frequency components that interfere with sensitive readings.

Although difficult, it is desirable to obtain experimental data relating to inter-bar currents in the rotor of an induction machine. Regardless of the feasibility, the most obvious method of determining information about inter-bar currents is to attempt direct measurement by inserting custom current transducers around strategic sections of the rotor iron. A more indirect method of measuring the effects of inter-bar currents is by measuring the heat generated in select areas where inter-bar currents are most prevalent. The benefit of using temperature data to extrapolate data on inter-bar currents is that temperature sensors are easier to implement than custom current transducers, more robust and conceptually easier to understand as compared to direct measurement.

Unfortunately, the problem of commutating the signals from the rotor still exists, even if a good procedure for acquiring the data is possible. To overcome this difficulty, a special inverted three-phase induction machine was developed for this study. The motor has a stationary rotor and shaft fixed to the frame, and allows the stator to rotate around the rotor. Similar to the large majority of three-phase induction machines, the excitation is still applied to the stator coils, but for this motor it is commutated through slip rings. This allows direct instrumentation of the rotor, overcoming the disadvantages previously noted for a standard induction machine. As a supplementary benefit, the inverted motor suffers from a higher level of losses as compared to a normal induction motor because of design inefficiencies which will amplify any loss readings acquired from it.

It is the purpose of this thesis to use the custom inverted induction motor in order to determine the presence, distribution, magnitude and effects of inter-bar currents on the rotor of an induction machine, and compare the experimental results to the theoretical work of the authors discussed in Chapter 2. The motor will be instrumented with standard measurement tools, which will be connected to a PC-based data acquisition system for data logging, manipulation and analysis. Two general methodologies will be used to obtain and analyze data relevant to inter-bar currents from the motor. The first set of tests will exploit the fact that inter-bar current losses generate heat, and measure the temperature increase in the rotor iron, eventually relating this temperature rise to inter-bar currents through mathematical calculation. The second set of tests will directly measure the inter-bar currents through the use of custom current transducers, or search coils, wound around strategic areas of the rotor iron, yielding much faster response times at the cost of increased electrical interference.

3.1 Temperature Tests

For an ideal rotor, the iron core is perfectly insulated from the cast aluminum cage offering no path for inter-bar currents to flow. In practice however inter-bar currents do flow through the rotor iron generating heat in the rotors iron core. Measuring the rate at which the temperature of the rotors iron core increases when the excitation is applied to the stator is a good indication of the heat produced by inter-bar currents. In particular, during the first few seconds of stator excitation, the heat generated in the iron core will be almost completely a result of inter-bar current losses.

After time has passed, radiant heat from the bars will begin to contribute to an increase in temperature, and cooling effects from convection, conduction and radiation will act to reduce the heat gain until a steady-state is reached. However, assuming the inter-bar currents are constant when the excitation is applied, the rate-of-rise of temperature during the initial seconds of excitation will demonstrate the heating effects of inter-bar currents in isolation. Using this preposition, the RMS value of the inter-bar currents can be found from the initial rate-of-rise of temperature on the rotor.

Multiple thermocouples and Resistance Temperature Detectors (RTD's) will be affixed to the rotor at strategic points in order to gather the required thermal data. Once the data is gathered using the data acquisition system, the temperature data will be used in subsequent sections to calculate the actual RMS values for the inter-bar currents. However, since the thermal response of the iron core is much slower than the expected frequency of the electrical signals, this methodology will not yield any insight into the actual waveform and frequency components of the inter-bar currents.

3.1.1 Inter-bar Currents as a Function of Temperature

The fundamental principle behind the thermal tests previously outlined is that temperature data sampled from particular points on the motor can be mathematically correlated to the inter-bar current in that section of the rotor. Under a few simple assumptions, the RMS or average values of inter-bar currents at the temperature acquisition points can be expressed analytically as a function of the temperature and several material constants. Since the composition of the iron core and the manufacturing process are known for the motor, all relevant constants can be determined, leaving a direct relationship between the rate-of-rise of temperature and the RMS value of inter-bar currents. This process is discussed presently, with an outline of the general Ohmic heating relationship, a simplified discussion of specific heat capacity and the reliance on the rotor materials temperature resistivity.

Ohmic Heating

An electrical current in a resistive load generates power in the form of Resistive or Ohmic Heating. A simple equation governing the instantaneous generation of this power in watts is:

$$P = I^2 R \text{ Watts} \tag{3.1}$$

The actual heat generated over a period of time in Joules is then:

$$Q = \int_t P dt = \int_t I^2 R dt \text{ Joules} \tag{3.2}$$

Specific Heat

Since the heat is being generated in a solid mass of laminated iron, the relationship between the heat generated and the temperature is governed by:

$$Q = cm\Delta T \text{ Joules} \tag{3.3}$$

where

c = the specific heat capacity of the composite $(J/kg \cdot {}^\circ K)$

m = the mass of the material (kg)

ΔT = the change in temperature $({}^\circ K)$

Setting equations 3.2 and 3.3 equal, providing that there are no thermal losses such as through conduction, convection or radiation, yields an equation relating the temperature rise of the iron core to the inter-bar currents:

$$Q = \int_t P dt = \int_t I^2 R dt = cm\Delta T \text{ Joules} \tag{3.4}$$

Iron Core Resistance

To simplify the solution for the inter-bar current I in equation 3.4 we assume that the resistance of the iron core is constant over the temperature range of the experiment. A simplified linear equation governing the change in resistance of a material with respect to a change in temperature is:

$$R = R_o\left(1+\alpha\left(T - T_0\right)\right) \tag{3.5}$$

where

R_o = the resistance at T_o (Ω)
α = the temperature coefficient of resistance $\left({}^\circ C^{-1}\right)$
T_o = the initial temperature $\left({}^\circ C\right)$

For pure iron, the change in resistance over the maximum expected operating range of the experiment from 3.5 is then:

$$\frac{R-R_o}{R_o} = \frac{R_o\left(1+\alpha\left(T-T_0\right)\right)-R_o}{R_o} = \frac{R_o\left(1+0.005\left(40-20\right)\right)-R_o}{R_o} = \frac{R_o\left(1.1\right)-R_o}{R_o} = 0.1 \text{ or } 10\%$$

The iron core is actually composed of laminated iron which has a much higher temperature coefficient of resistance than pure iron, making the expected change in resistance much smaller than that calculated using pure iron as in equation 3.5. Additionally, the actual increase in temperature during the experiment is expected to be less than 20°C, further reducing the change in resistance of the iron core. For these reasons, and to simplify calculations using equation 3.4, the resistance of the iron core is assumed to remain constant over the operating range of the experiment.

Inter-bar Currents as a Function of Temperature

Moving the resistance R to the right side in equation 3.4 yields:

$$\int_t I^2 dt = \frac{cm\Delta T}{R} = \frac{cm(T - T_0)}{R} = \frac{cmT}{R} - \frac{cmT_0}{R} \tag{3.6}$$

Differentiating both sides of equation 3.6 with respect to time gives a solution for the inter-bar currents:

$$I^2 = \frac{cm}{R}\frac{dT}{dt} \rightarrow I = \sqrt{\frac{cm}{R}\frac{dT}{dt}} \tag{3.7}$$

From equation 3.7, the RMS value of the inter-bar currents can be calculated under the following assumptions:

1. The inter-bar currents are constant while the excitation is constant
2. The resistance of the iron core is independent of temperature over the operating range of the experiment
3. The temperature curve of the iron core is known and differentiable
4. The specific heat capacity of the iron core is known and uniform

3.1.2 Inter-bar Current Heat Distribution

In order to obtain temperature data pertaining to losses generated by inter-bar currents, the temperature sensors must be affixed to the rotor. Since the sensors can be attached in any desirable configuration, the instruments can be located to determine the temperature rise of strategic points to establish a three-dimensional thermal distribution between adjacent rotor bars. To achieve this distribution, the thermal sensors will be strategically placed throughout the geometry of the iron core between select adjacent rotor bars. Once the sensors are placed, the thermal data acquired will be compared for various points between the end rings, between the rotor bars and at various depths radially into the iron to develop a geometric heat distribution.

3.2 Direct Measurement Tests

Considering that inter-bar currents are relatively high-frequency alternating currents between adjacent rotor cage bars, it is theoretically possible to directly measure them by using current transducers or search coils. As dictated by Lenz's law, the inter-bar currents produce a magnetic field which will in turn induce current in search coils, provided a closed path exists, in some proportion to the original inter-bar current waveform. The performance of the search coils is based on the geometry of the windings, the number of turns, and the properties of the ferromagnetic iron core. Although the overall magnitudes will differ, a simple search coil can indicate the shape of the inter-bar current waveforms without consideration of the magnitudes. As a result of difficulties winding the search coils to directly measuring inter-bar currents, the search coils for this thesis were instead wound to measure the induced voltage due to the main rotating field flux. A detailed discussion of different search coil orientations is presented in Chapter 6. The two most significant limitations to physically implementing search coils are rotor construction and space restrictions.

A typical induction machine rotor is manufactured by casting the rotor cage around the iron core. The core consists of laminated iron sheets that are punched with the rotor cage geometry, and the core itself is used as the mould. The hot temperatures of the casting process make it extremely difficult to insert search coils prior to the rotor construction. Additionally, the test motor used for these experiments was manufactured prior to the decision to implement search coils. This required modification to the rotor after manufacturing to facilitate insertion of the search coils.

In order to contain the entire section of rotor iron between adjacent rotor bars, a portion of the search coil turns by necessity must be located along the surface of the rotor. In most small induction machines, the air gap is much less than 0.5mm or 20 thousandths of an inch, leaving little room for search coil leads. To allow the positioning of the leads along the surface of the rotor, an additional channel must be inset deep enough that the search coil leads do not interfere with the stator.

Using the changes outlined above, the rotor was modified to facilitate the insertion of four search coils evenly spaced around the rotor every 90°. Each search coil encompasses the entire portion of the iron core in an axial loop, located directly between the respective adjacent rotor bars. The modifications to the rotor compensate for the skew angle of the test motor to uphold the design specifications of the motor allowing the search coils to be wound parallel to the rotor bars. Figure 3.2.1 shows a general search coil winding on the rotor:

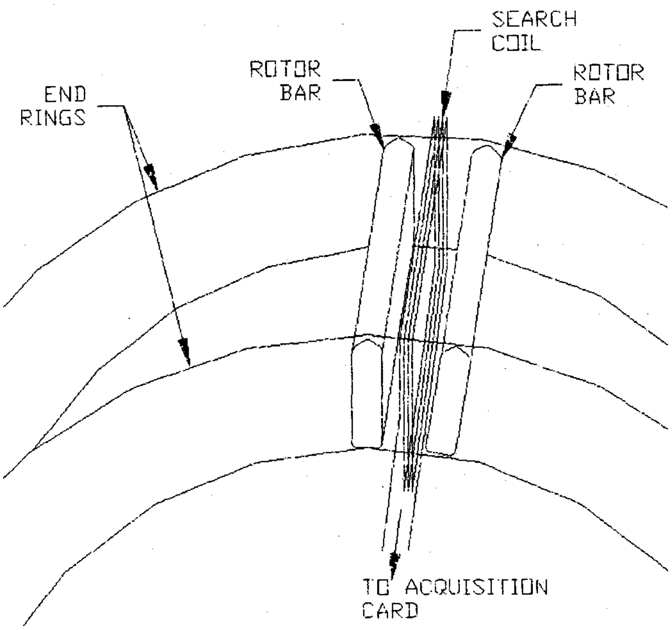

Figure 3.2.1: Search Coil Configuration

3.2.1 Frequency Components of Inter-bar Currents

Compared to direct measurement using the custom search coils, the thermal methodology is more robust, simpler to implement, and conceptually easier to understand. However, its major limitation is that temperature has a much slower response time than the true frequencies of the signals. The use of search coils will give much more insight into the actual shape of the inter-bar current waveforms, including the major frequency components that comprise the inter-bar currents. The most significant disadvantages of the direct measurement methodology are the difficulty in calculating the proportional relationship between the true inter-bar currents and the sensor output waveforms because of the complicated geometries involved, and winding the coils in the necessary configuration to measure the inter-bar currents rather than the flux.

3.2.2 Inter-bar Current Distribution

The search coils used in the experiment include the entire segment of rotor iron between adjacent rotor bars. Additionally, auxiliary search coils could be inserted around smaller sections of the rotor iron to obtain the three-dimensional distribution of inter-bar currents. Due to the nature of electrical currents, plotting the distribution along a plane between the two rotor end rings, extending radially outward from the motor shaft between the rotor bars is sufficient. The third dimension, defined circumferentially around the rotor surface using polar coordinates is irrelevant from the perspective of direct current measurement since the currents are by nature continuous and constant along the current path.

Chapter 4

Experimental Setup and Procedure

As discussed in Chapter 3, two main methods are used to experimentally measure the presence, distribution, magnitude and effects of inter-bar currents: Temperature Measurements and Direct Measurements. This chapter begins with a brief description of the custom built three-phase rotating stator induction motor used for all experiments. Following that, the physical and electrical setups are outlined, along with an outline of the instrumentation used. The chapter concludes with a detailed explanation of the experimental procedure used to generate the required test results for both the indirect temperature measurement tests and the direct search coil tests.

The motor was instrumented to facilitate two general sets of readings on the rotor:

1. Temperature readings using various types of thermocouples and RTD's, surface mounted and buried into the rotor iron on and between rotor bars
2. Proportional inter-bar current measurement using search coils wound around segments of rotor iron between adjacent rotor bars

The first section outlines the motor parameters and specifications. The second section discusses the physical setup of the motor and experiment. The third section shows the electrical setup of the experiment, as well as the data acquisition setup. The fourth section discusses the experimental procedures used to acquire data for analysis. Relevant physical dimensions are included in Appendix A.

4.1 Rotating Stator Induction Motor Specifications

Based on the nameplate data, the motor used for the experiments was a 575VAC, "wye" connected, three-phase 60 hertz rotating stator squirrel cage induction motor produced by Westinghouse is used. At no load the motor consumes 0.63kW, drawing 4.53A and is rated at 900RPM. The stator has eight full pitch poles, with the three-phase windings distributed over 48 slots with 98 wires per slot. Each coil has 24 turns, with 48 coils per set. The line-to-line resistance at 25 °C is 5.64Ω. The rotor cage is aluminum, cast around a stack of iron plates with a deep bar design punched out. The rotor cage has a total of 37 rotor bars, with a skew of 1 stator slot. All relevant mechanical and assembly drawings can be found in Appendix A.

4.2 Physical Setup

The stator coils are mounted on the inside of a cylindrical steel tube, which is contained on each end by circular endplates. The rotor is embedded in the stator, with the motor shaft extending through the stator endplates. The rotor shaft is fastened at each end to a steel frame to prevent the rotor from rotating. The stator endplates are allowed to rotate freely around the rotor shaft by bearings press-fit into bearing sleeves located at the center of the stator endplates. Slip rings are used to provide power to the rotating stator, and are mounted on a steel tube extending out from one of the stator endplates. The slip rings are isolated from the motor by a layer of Bakelite between the slip rings and the steel tube. The mechanical setup is shown in Figure 4.3.1 and Figure 4.3.2 below:

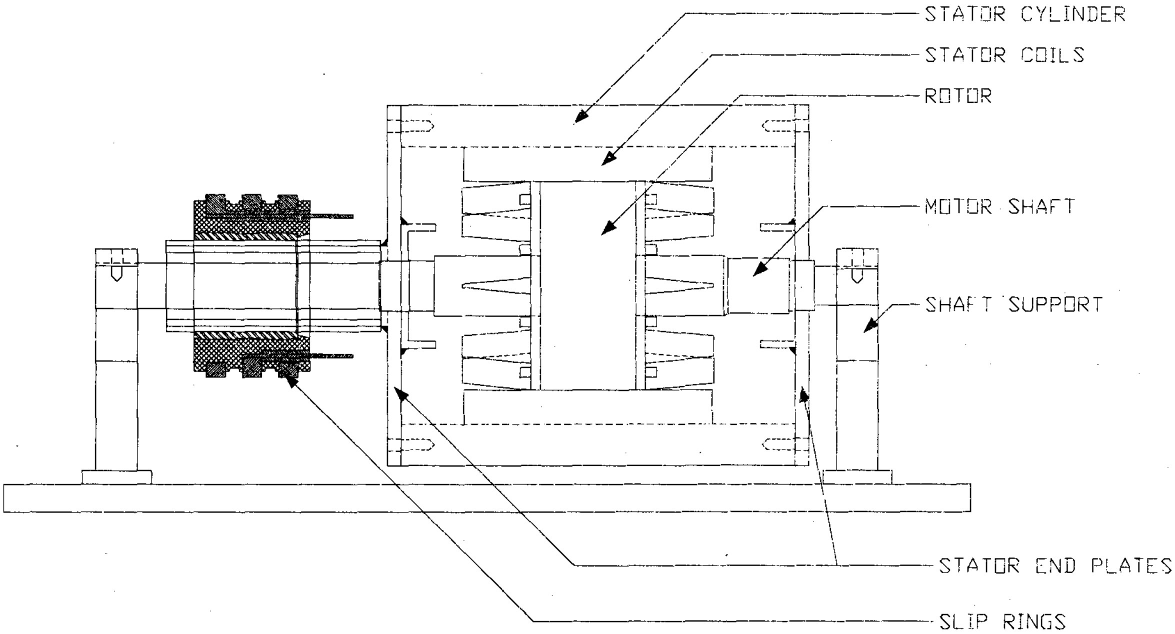

Figure 4.2.1: Physical Motor Setup

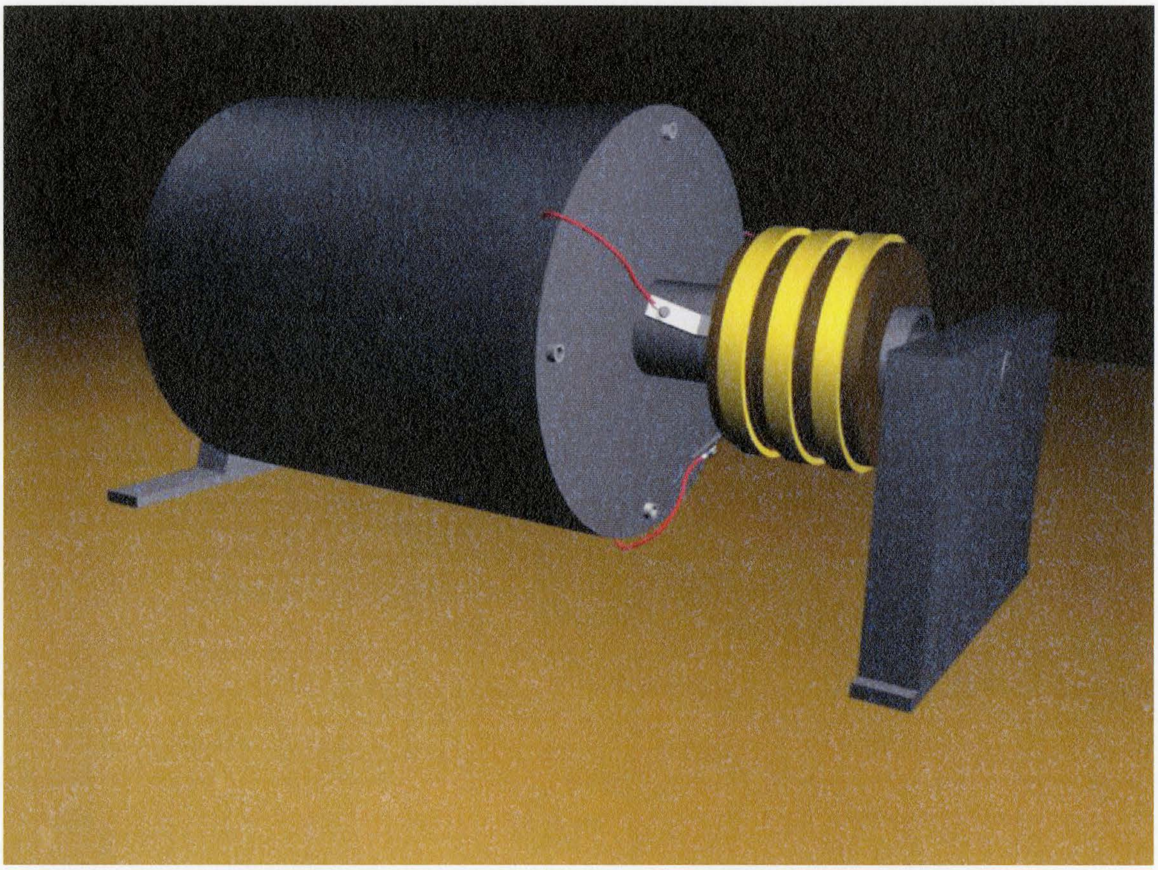

Figure 4.2.2: Physical Motor Setup

The individual components of the physical setup, including dimensioning and significant material properties can be found in the attached Appendix A.

To perform any experiments on the rotor the motor must be disassembled into individual components, instrumented, and then carefully reassembled to avoid damaging any instrumentation. The entire motor assembly, including the support frame weighs approximately 750 pounds. The stator/rotor assembly weighs approximately 300 pounds alone, requiring the use of an overhead pneumatic hoist to lift it off the support frame. To gain access to the rotor, the shaft supports are first disconnected from the support frame, and the entire stator, rotor, slip rings and shaft supports are lifted off the base and onto the floor using the overhead hoist. Once the shaft supports are removed, the stator/rotor assembly is tipped onto the outer end plate on two blocks to allow clearance for the shaft. Once on its side, the inner end plate can be removed, and finally the rotor can be pulled out of the stator.

4.3 Electrical Connections and Instrument Setup

Since the motor experiments were performed on the assembly floor of ATL Industries in Uxbridge, Ontario, the experimental apparatus was designed to be easy to assemble and disassemble electrically and mechanically without interrupting ATL's production. The motor support frame is mounted on castors, making it relatively easy to move around when necessary. The data acquisition system was also mounted on a cart allowing for easy relocation. All additional hardware was either mounted directly to the motor frame (for example the main electrical disconnect), or to the data acquisition cart (for example the analog instrumentation breakout board) and connected using quick-disconnect or simple terminal based connectors.

4.3.1 Power Connections

The electrical connection to the motor is made using a 600VAC Harding connector on a 5 meter lead through a 15A three-phase disconnect, which interfaces to 600VAC receptacles located in various locations around the ATL assembly floor. This creates the flexibility to move and connect the motor to a 600VAC supply anywhere in the building. To allow for convenient starting and stopping of the motor excitation, a simple three-phase motor contactor with a 120VAC start/stop pushbutton assembly was used. The electrical connections can be seen below in Figure 4.3.1

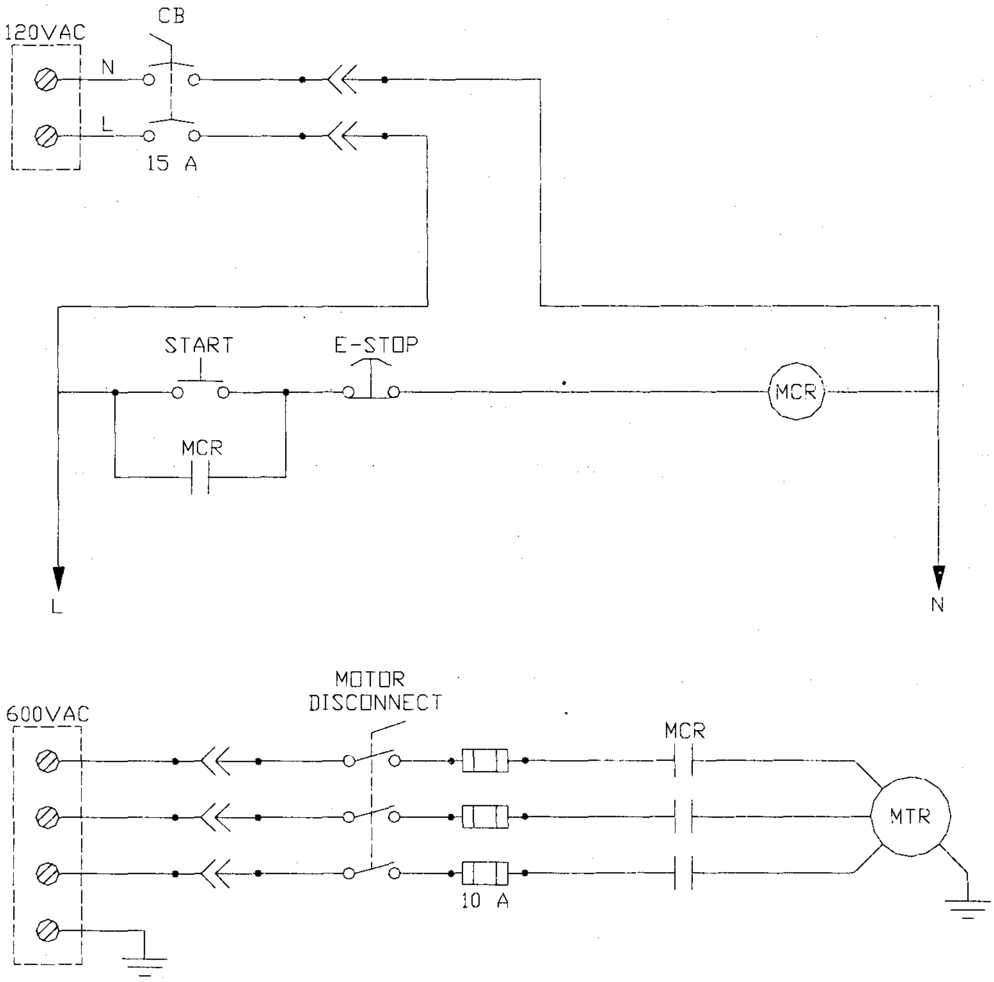

Figure 4.3.1: Power Connection

4.3.2 Thermocouple Placement

To acquire temperature data from the rotor, both thermocouples and RTD's were used. All thermocouples used are T-type because of their electromagnetic insensitivity and ideal temperature sensing range. T-type thermocouples are linear over a range from 0-300°C which includes the expected thermal operating range of the motor. RTD's were also implemented as a secondary option in case the thermocouples did not function adequately in the electromagnetic field of the motor. RTD's are more accurate than thermocouples and are more resistant to electromagnetic interference because a ground reference exists at the measurement junction, but are typically 5 to 10 times more expensive than a thermocouple and twice as large. As such, only a single RTD was purchased to test its performance compared to the thermocouples.

The placement of the sensing junctions of various thermocouples can be seen on the rotor schematic below in Figure 4.3.2. To attain the temperature distribution of the inter-bar current heat losses, four groups of four thermocouples were placed between adjacent rotor bars, and spaced evenly between the rotor end rings. Each group was then offset approximately 90 degrees around the axis of the shaft. Each group consists of four thermocouples; two placed on the surface and two placed in small blind holes drilled to approximately half the depth of the rotor bars. Of the two surface-mounted thermocouples, one is placed on a rotor bar, and the other at the midpoint between the rotor bars. The two remaining thermocouples are placed either adjacent to a rotor bar or again at the midpoint between rotor bars below the surface of the rotor. To attach the thermocouples to the rotor, a high-temperature thermal epoxy was used. The epoxy has a high thermal conductivity, is an excellent electrical insulator, has a rated operating range up to 500°F and offers good physical adhesion properties. As an auxiliary benefit, the epoxy takes approximately 4 hours to cure at 400°F, which allows delicate placement of the thermocouples without concern for immediate adhesion.

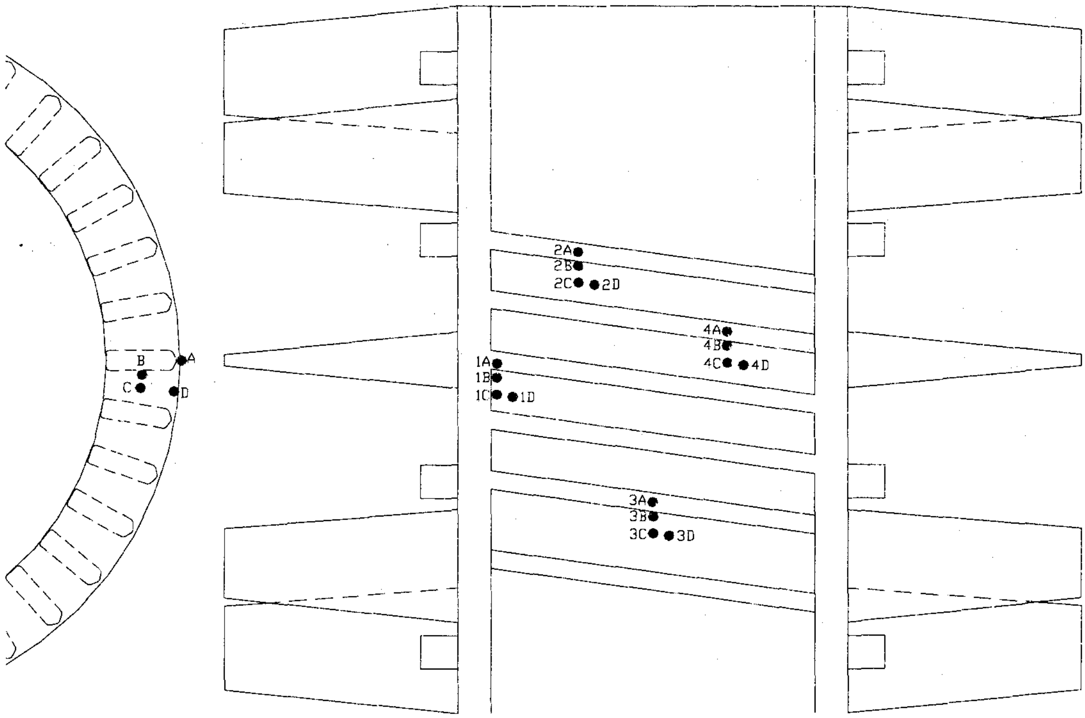

Figure 4.3.2: Thermocouple Placement on the Rotor

The thermocouple leads are located in small channels cut in the rotor surface. This was necessary because the clearance between the rotor and the stator coils (the air gap) is approximately 0.010 inches (0.25mm). The thermocouples (and RTD) are connected to transmitters serving to convert the low power voltage outputs of the instruments to 4-20mA signals. The 4-20mA signals are then wired to 250Ω resistors to convert the signals to 1-5V analog outputs for the data acquisition card.

4.3.3 Search Coil Setup

In order to measure the frequency components of the resulting flux in the rotor, which should be proportional to the inter-bar current frequencies, it is necessary to wind search coils around the segments of rotor iron located between adjacent rotor bars. As discussed in Chapter 3, the motor was manufactured by Westinghouse without any provision for such an undertaking, thus modifications to the rotor were necessary. It is desirable to include only the rotor iron in the turns of the search coils, but to carefully exclude any other current paths such as the end rings. To achieve this each search coil requires three holes to be drilled in the rotor as show in Figures 4.3.3a and 4.3.3b.

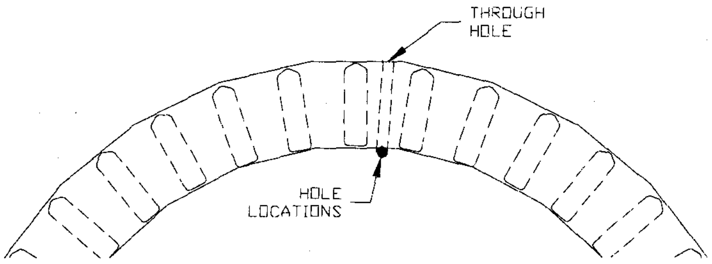

SIDE VIEW OF ROTOR

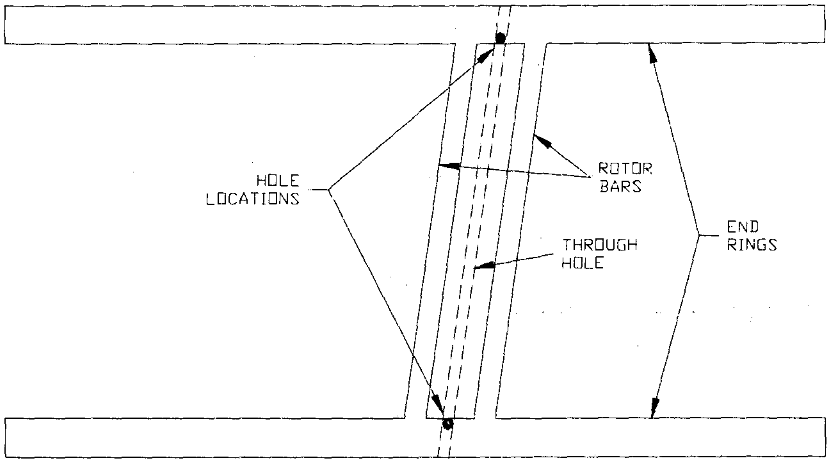

TOP VIEW OF ROTOR

Figure 4.3.3a: Search Coil Hole Locations

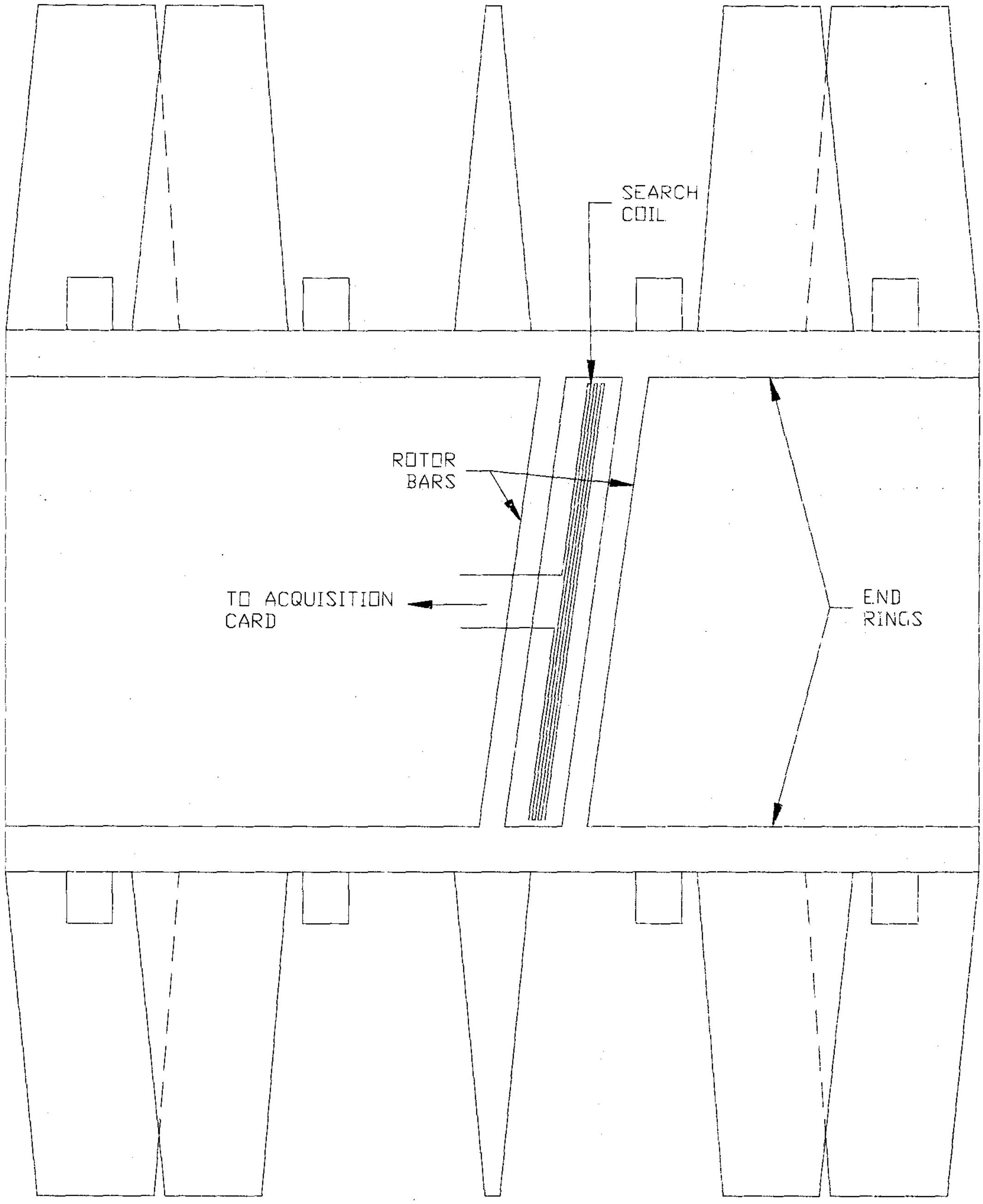

Figure 4.3.3b: Search Coil Location

For each search coil, one hole penetrates radially inward towards the rotor shaft through the each end ring directly adjacent to the rotor iron at the midpoint between adjacent rotor bars. Each hole is drilled to the depth of the rotor bars, just below the end rings. To facilitate the return path of the search coils below the rotor bars an angled hole was drilled parallel to the rotor bars along the plane of the rotor shaft, connecting the two radial holes. Finally, to allow clearance for the search coil windings between the rotor and stator, a shallow channel was cut between the radial holes[1]. These modifications were repeated four times at equal intervals 90 degrees apart around the rotor, allowing for four search coils to be installed. The coils were wound with 5 turns each, and the leads of the search coils were connected to resistors to provide a path for current. A three-dimensional representation of the hole and channel modifications on the rotor can be seen below in Figure 4.3.4.

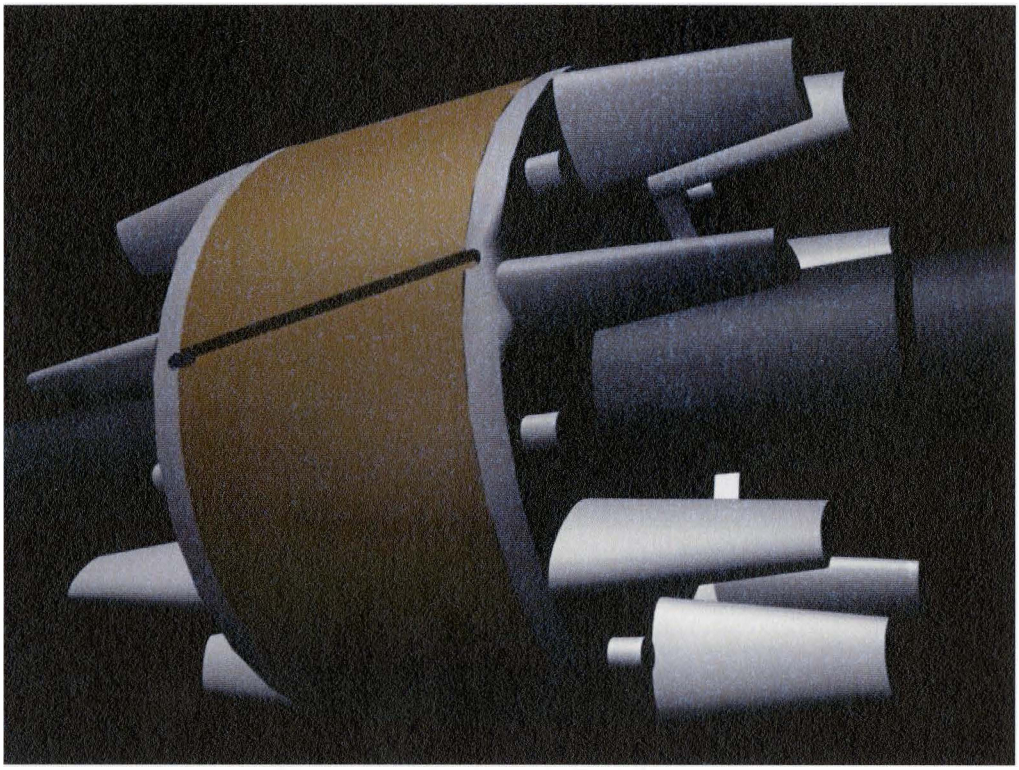

Figure 4.3.4: Search Coil Slots

---

[1] Any contact between iron laminations from the milling process will not affect inter-bar currents since the currents flow parallel to the laminations regardless

4.3.4 Data Acquisition System Setup

The physical data acquisition setup is outlined in detail in Appendix D. The accuracy and resolution of the analog sampling is determined by three factors related to the data acquisition system and measurement instruments:

1. Experimentation revealed that the direct analog input of the search coils was approximately ±5 V AC, requiring that the analog input channels used for search coils be set to accept bipolar signals in the range of ±10 VDC
2. T-type thermocouples used for the experiment give a valid output over a range of 0-300°C. This signal is converted to a 1-5VDC signal by the thermocouple transmitters, requiring that the analog input channels be set to accept unipolar signals in the range of 0-10 VDC
3. The DAQ card is a 16-bit Analog to Digital conversion card, which gives 65536 divisions of resolution. For the thermocouples, the analog card is set up to allow a 0-10VDC signal, but the input signal is conditioned to 1-5VDC by the thermocouple transmitters, which allows only 40% of the 65536 divisions of resolution on the thermocouple input. The resulting temperature resolution in degrees Celsius is then:

   $$\frac{(300-0)^{\circ}C}{(65536)(0.40)} = 0.011^{\circ}C \tag{4.1}$$

   For the search coils, the resolution is calculated over the entire range as

   $$\frac{(10-(-10))V}{(65536)} = 0.0003V \tag{4.2}$$

4.4 Experimental Procedure

In order obtain enough data to determine the inter-bar current distribution in two dimensions (radially outward and along the length of the rotor shaft) as shown in Figure 4.4.1, a total of 16 thermocouples were mounted as described in section 4.3.1. Additionally, to directly measure the inter-bar currents, four search coils were also installed. Ideally, a single test should be performed using all instruments to ensure the test conditions are the same for all data points. Unfortunately, due to several factors, one single test could not be performed to acquire all the data simultaneously because of the following factors:

1. Space limitations between the stator and rotor (air gap) prevented all the required thermocouples from being attached simultaneously
2. Clearance limitations with the instrument leads through the bearing assemblies allowed for approximately 10 devices to be fed from the rotor to the external acquisition hardware
3. Only two thermocouple transmitters and one RTD transmitter were used, limiting the number of concurrent temperature readings to three
4. The analog input card supports a maximum of eight differential analog inputs
5. The analog input card supports a maximum 200,000 samples per second over all inputs, which limited the number of inputs that could be used for the experiments that required faster sample rates

As a result of these limitations, multiple tests were required under similar conditions such as ambient temperature, excitation length, cooling time, etc. to ensure integrity of data. There were two general temperature tests using the thermocouples and RTD's which are outlined in section 4.4.1. The search coils were used for three general tests which are outlined in section 4.4.2.

4.4.1 Temperature Acquisition Tests

To properly capture the thermal effects of inter-bar currents on the rotor, a sample rate of 20 samples per second was used. It was experimentally determined through trial and error that a lower sample rate did not adequately illustrate the true response of the instruments, and that a higher sample rate over-sampled the thermal response, unnecessarily generating larger data sets. Two general temperature tests were performed on the motor to acquire data on the thermal effects of inter-bar currents when the motor speed has reached a steady-state and during start-up, named Start-up and Steady-State tests.

Steady-State Thermal Response Test

The first test was a simple test where the excitation was applied to the motor for 10 minutes in order monitor the heating effect on the rotor during prolonged operation. Figure 4.4.1 below shows a timing chart depicting the *predicted* temperature response of a general thermocouple. In particular, a rapid temperature rise is expected when the excitation is first applied, reflecting the finite amount of time for various cooling effects to take place. Additionally, the speed of the rotor and the status of the excitation are also shown on the figure. As the motor reaches a steady-state with respect to speed, the temperature of the rotor iron is expected to increase at a slower rate due to cooling via conduction, convection and radiation.

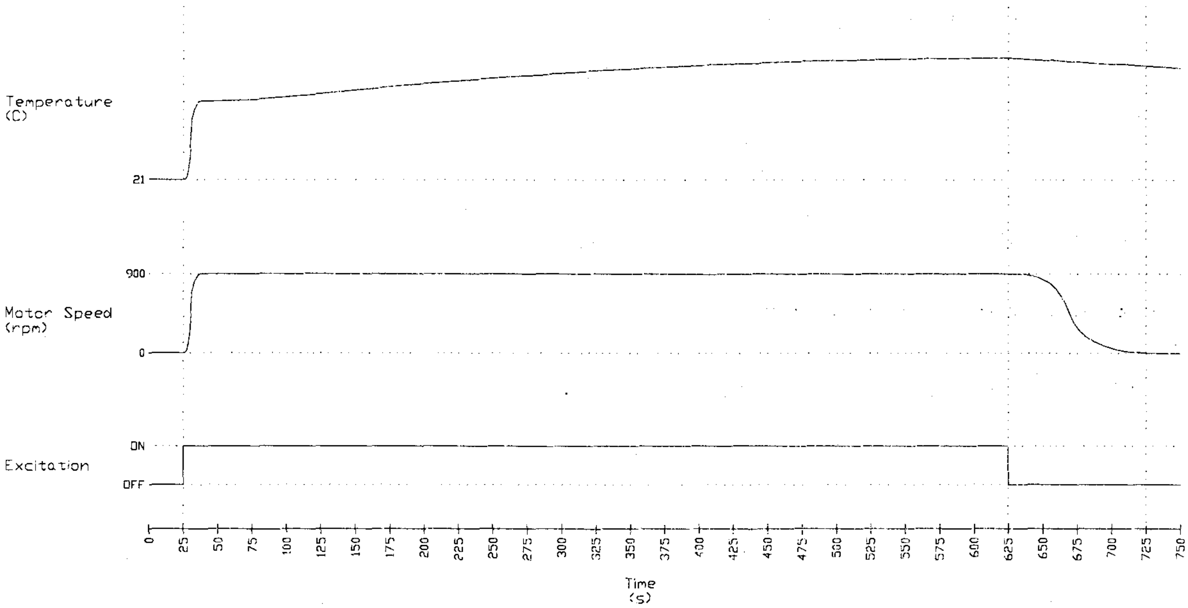

Figure 4.4.1: Timing for Steady-State Thermal Response Test

It is important to note that the thermal response curve in Figure 4.4.1 is only provided to show the general response of a thermocouple regardless of its location on the rotor iron with respect to the rotor bars and the depth from the surface. It is expected that the distribution of inter-bar currents is non-uniform along the length of the rotor bars, as well as radially outward from the rotor shaft. This will cause a change in the magnitude and rate-of –rise of the temperature spike during startup, as well as the slope of the curve approaching steady-state based on the location of the thermocouples.

Start-up Thermal Response Test

A second test was performed focusing on the rate-of-rise of temperature at various points on the rotor during startup. For this test, the motor excitation was applied to the motor for 10 seconds to ensure that the motor achieved full speed. Once at full speed, the excitation was removed. The motor was allowed to coast to a full stop, and then the same process was repeated a second time. When the motor stopped the second time, the excitation was reapplied for 10 seconds and then removed. However, this time the motor was only allowed to decelerate for a short period of time before the excitation was re-applied. This process was repeated two more times, allowing the motor to coast to a stop on the third. The complete timing of the motor excitation can be seen graphically below in Figure 4.4.2. This figure shows the speed of the motor and the expected thermal response of an average thermocouple in relation to the excitation status.

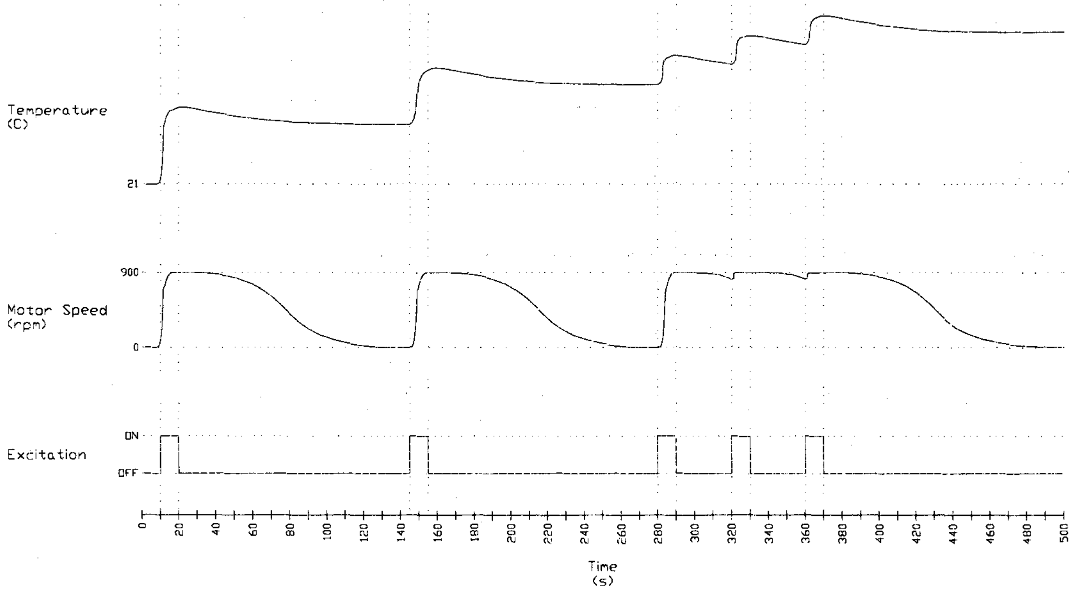

Figure 4.4.2: Timing for Start-up Thermal Response Test

The first portion of this experiment shows the effects of the inter-bar currents during startup while the motor is not moving, as well as the effects of radiant cooling while the motor is rotating. The second portion of this experiment highlights the heat produced by inter-bar currents during startup when the motor is already in motion.

4.4.2 Search Coil Acquisition Tests

Fundamentally, the search coil tests were similar in timing to the steady-state temperature tests. The data acquisition system was started, and then the excitation was applied to the motor for a fixed period of time. The length of time for each test was determined by the frequency component being measured.

Preliminary tests were performed using all four search coils to determine general information about their response during four separate stages of operation:

1. When the motor is idle and no excitation is present
2. Initial acceleration; when the excitation is first applied to the motor, to the point where the motor reaches full speed
3. Steady-State operation; when the motor has reached full speed, with continuous excitation
4. Deceleration of the motor; when the excitation is removed, with the motor remaining in motion

For the preliminary test, the data acquisition system was started at a sample rate of 20 samples per second. After 25 seconds, the motor excitation was applied and the motor was allowed to accelerate to full speed. The motor was left running at full speed for 30 seconds, at which time the excitation was removed and the motor freely decelerated to a stop at approximately 120 seconds. At 130 seconds, the excitation was reapplied to the motor. The excitation was removed at 160 seconds, and the data acquisition system was stopped at 170 seconds. The complete timing of the search coil tests, as well as the expected temperature rise of an average thermocouple and the expected average inter-bar current are shown below in Figure 4.4.3.

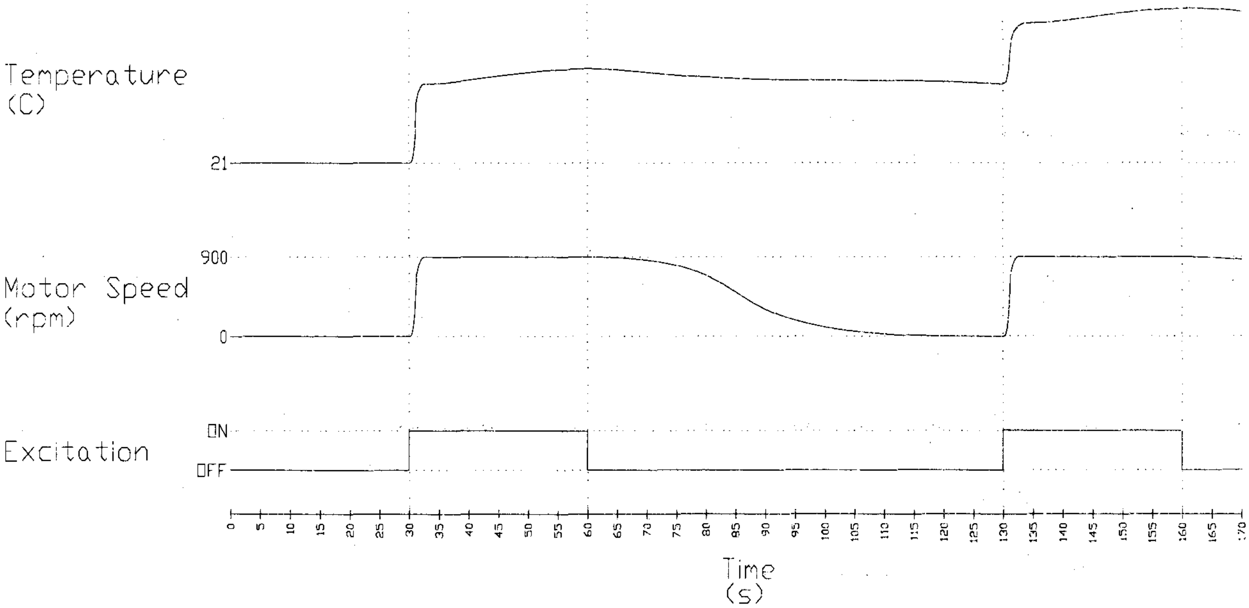

Figure 4.4.3: Timing for Search Coil Response Test

From the preliminary tests, it was discovered that the outputs of each search coil were signals composed of three sinusoidal waves superimposed at different frequencies. Three new sets of tests were performed to try to determine the frequencies of each component. For each set of tests, the sampling frequency was selected to ensure that a minimum of ten points per cycle of the output signal were captured. Additionally, the time duration of each test was selected to ensure enough total cycles were captured to perform a Fourier analysis on the signals.

4.5 Procedural Notes

A brief description of some important procedural notes developed during the experiments is provided in this section. Specifically, varying ambient conditions, manual motor excitation control and difficulties experienced with measurement instruments are discussed.

Temperature Datum

To provide a datum for all temperature data acquired over the multiple tests performed, the RTD was placed in ambient atmosphere and sampled simultaneously with the instruments on the rotor. The ambient temperature for each test was used as a reference point, and the entire temperature data for each test was shifted to move each data set to a reference temperature of 21°C.

Manual Motor Excitation

The motor excitation was controlled manually using a start/stop pushbutton controlling a power relay. Each individual experiment followed a set pattern as outlined in Section 4.4, but the individual experimental timing was slightly different for each experiment due to the manual control. This timing was only significant for the temperature tests however, since the search coil tests focused on the periodic nature of the signals, rather than the absolute data references. By inspection, experiments were rejected or repeated if the sampled curves did not comply with a window of ±10 samples (1 second) at each of the critical timing points.

Instrument Location and Failure

It was difficult to locate precisely each thermocouple in the exact positions outlined in Figure 4.3.1 because the motor was instrumented after manufacturing. The specific location of each rotor bar was difficult to determine without drilling several reference holes. Additionally, despite concerted efforts, it was extremely difficult to avoid any instrument damage during the instrumentation stage, assembly and disassembly of the motor, and even during operation largely due to the cumbersome and heavy construction of the motor.

Chapter 5

Experimental Results

Following the experimental procedures outlined in Chapter 4, multiple experiments were performed to gather data for both the thermal and the direct measurement search coil tests. In this chapter, the experimental test data will be presented in graphical form displaying the analog inputs versus time. The test data was acquired using the thermal tests outlined in Chapter 4, Section 4.4.1, and the direct measurement tests outlined in Chapter 4, Section 4.4.2.

A total of 12 thermocouples were originally affixed to the rotor for temperature acquisition, but several were damaged during the reassembly of the motor or during operation. In most cases, the thermocouples were damaged as a result of the tight clearance between the stator and the rotor, which allowed for little error in both the placement of the instrument leads and the motor reassembly. For the first set of tests, a total of 4 thermocouples were damaged or malfunctioned. The motor was disassembled, and an additional 6 thermocouples were attached to the motor. During the second set of tests, 3 of the new thermocouples failed, all due to damaged leads during the re-assembly of the motor. The result was a total of 11 successful individual thermocouple readings for the thermal tests.

After the second set of temperature tests were completed, the rotor/stator assembly was again disassembled and four search coils were wound around select rotor iron segments. The rotor iron segments were specifically selected to isolate the inter-bar current paths from other current sources such as bar currents and end-ring currents. Once properly wound and secured, the motor was reassembled to perform the proportional inter-bar current measurement tests. For the initial search coil test, a comparison of the performance of the following four different types of wire was performed:

1. 26AWG Stranded Copper Wire
2. 26 AWG Solid Copper Wire
3. 26 AWG Stranded Steel Wire
4. 26 AWG Solid Steel Wire

The resultant outputs of the four different wires were almost identical, so I chose to use this initial setup for all subsequent search coil experiments. Since a limited number of instrument leads can be fed through the bearing assemblies via the rotor shaft slots, only two thermocouple leads were attached to the acquisition system while the search coil leads were used. The remaining thermocouples were coiled to the rotor in the stator assembly for future experiments.

The results of the two thermal tests will be presented in section 5.1, both in raw form and using simple averaging to smooth the data sets. Additionally, polynomials will be fit to the raw data to represent the key features of the tests during analysis and discussion. The results of the proportional inter-bar current measurement tests will be presented in section 5.2, including a frequency domain analysis of the data.

5.1 Thermal Results

For the thermocouple experiments, the raw data acquired from the system was not suitable for direct analysis. Instead the raw data required conditioning to remove the inherent noise. The temperature tests yielded results corrupt with noise for two reasons:

1. The electrical sensitivity of the thermocouples to electromagnetic interference was represented as voltage spikes. In particular, thermocouples placed close to the rotor bars were susceptible to noise, especially during startup.
2. The data acquisition system sampled data from the analog input channels to three decimal places. This sampling resolution was not user-adjustable, causing the temperature readings to have an associated acquisition noise. This noise occurred as a result of the relative accuracy of the thermocouple transmitters with respect to the sampling resolution. As outlined in Chapter 4, Equation 4.1 the thermocouple transmitters, paired with T-type thermocouples provided an analog temperature accuracy of 0.011°C, which is significant to two decimal places. The analog input card, sampling to three decimal places, generated a somewhat random value in the third decimal place, creating somewhat choppy outputs in need of conditioning.

The results of the steady-state thermal test will be presented in section 5.1.1, followed by the results of the startup thermal test in section 5.1.2. For each section, the raw data as obtained by the acquisition system will first be presented. Simple filtering and smoothing will be applied to each raw data set. Using the filtered data sets, key features of the output waveforms will be highlighted. The raw data with then be fit with a polynomial which will be used for analysis and computations.

5.1.1 Steady-State Thermal Test Results

The purpose of the steady-state thermal test is to obtain data on the temperature rise of select points on the rotor core during acceleration and steady-state operation. The thermocouples are positioned on and in the rotor iron to measure the direct heating effect of inter-bar current, and isolate the effects of other factors that generate heat in an electric motor. The steady-state tests emphasize the heat produced during a single startup and during continuous operation of the motor.

In conformance with the experiment outlined in Chapter 4, Section 4.4.1, sampling of the analog inputs is started at 0 seconds. The motor excitation is then applied at 25 seconds, and the motor reaches full speed approximately 3 seconds later. The motor is allowed to run continuously for 10 minutes, at which time the excitation is removed.

Raw Results: Steady-State Test

The raw results of three thermocouples taken from the steady-state thermal test can be seen below in Figure 5.1.1. The results are too noisy to include the outputs of all the thermocouples on a single graph, and clearly require significant smoothing to reveal the true reaction of the thermocouples.

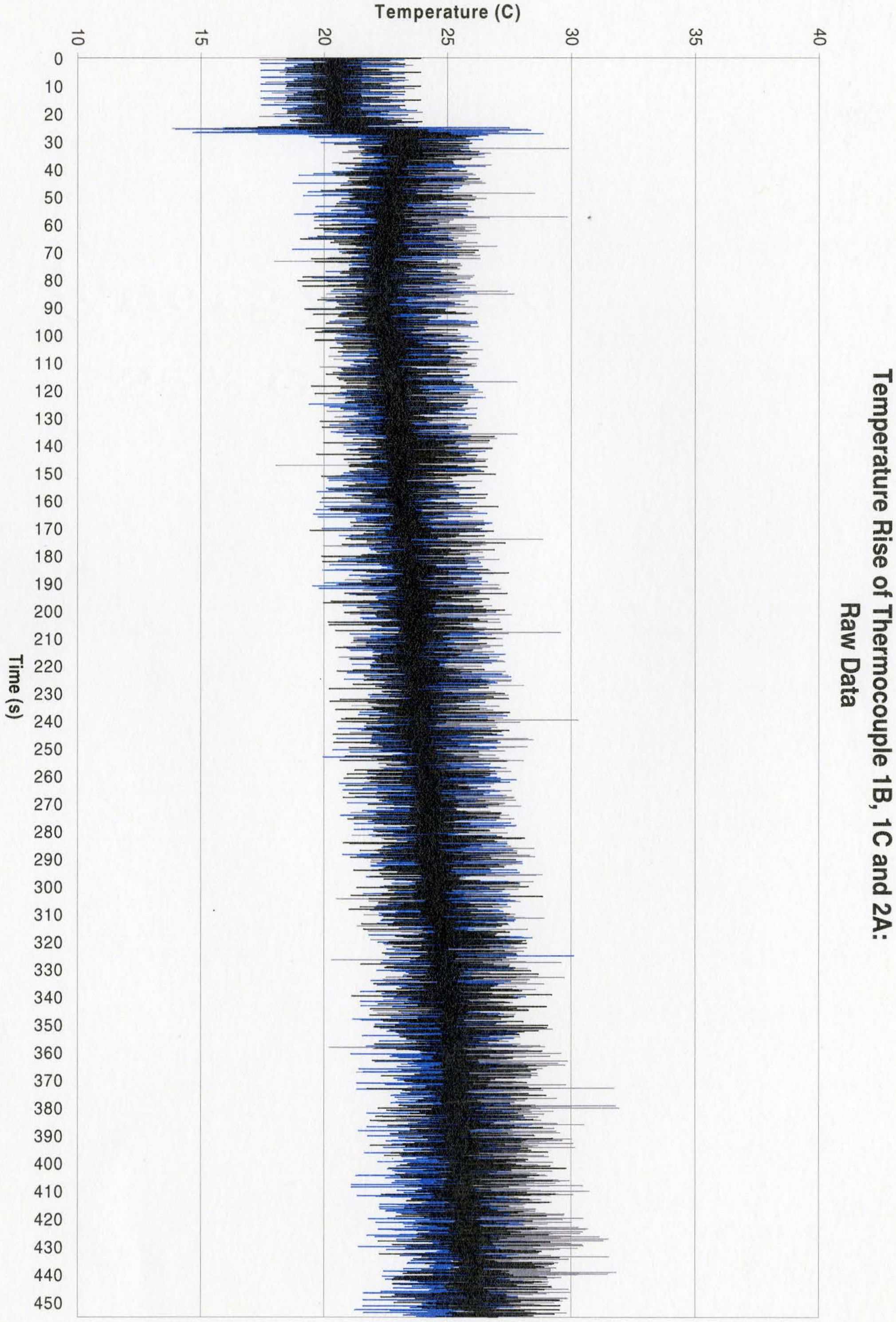

Figure 5.1.1: Steady State Test: Raw Data output for thermocouple 1B, 1C and 2A

Filtered Data: Steady-State Test

To filter the noise and smooth the raw data, a forward moving average was used on the raw data set, acting as a simple low-pass filter. Since the noise is normally distributed around the expected true readings, a simple moving average should sufficiently filter the high-frequency components from the raw data and reveal a good estimate of the true temperature values existing at the rotor. The moving average for the data set is defined as:

$$f_i = \frac{1}{n}\sum_{j=i}^{i+n-1} r_i \qquad (5.1)$$

where

f_i = the value of the ith filtered data set point

r_i = the value of the ith raw data set point

n_i = the period of the averaging

To filter the high-frequency noise from the signal, a value of $n = 250$ was used in equation 5.1, with the results shown in Figure 5.1.2. The results are much smoother and more distinguishable than the raw data and the initial averaging. However, a direct result of the averaging is a slight skewing of the original waveform. The graph in Figure 5.1.1 shows a sharp rise in temperature corresponding to the application of the excitation at 25 seconds. In Figure 5.1.2, this initial rise happens almost 10 seconds sooner; a direct result of the averaging. The skewing of the data means the averaged data is not directly useful for understanding the true response of the thermocouples. However, they are relevant since they offer a simple representation of the response of the thermocouples.

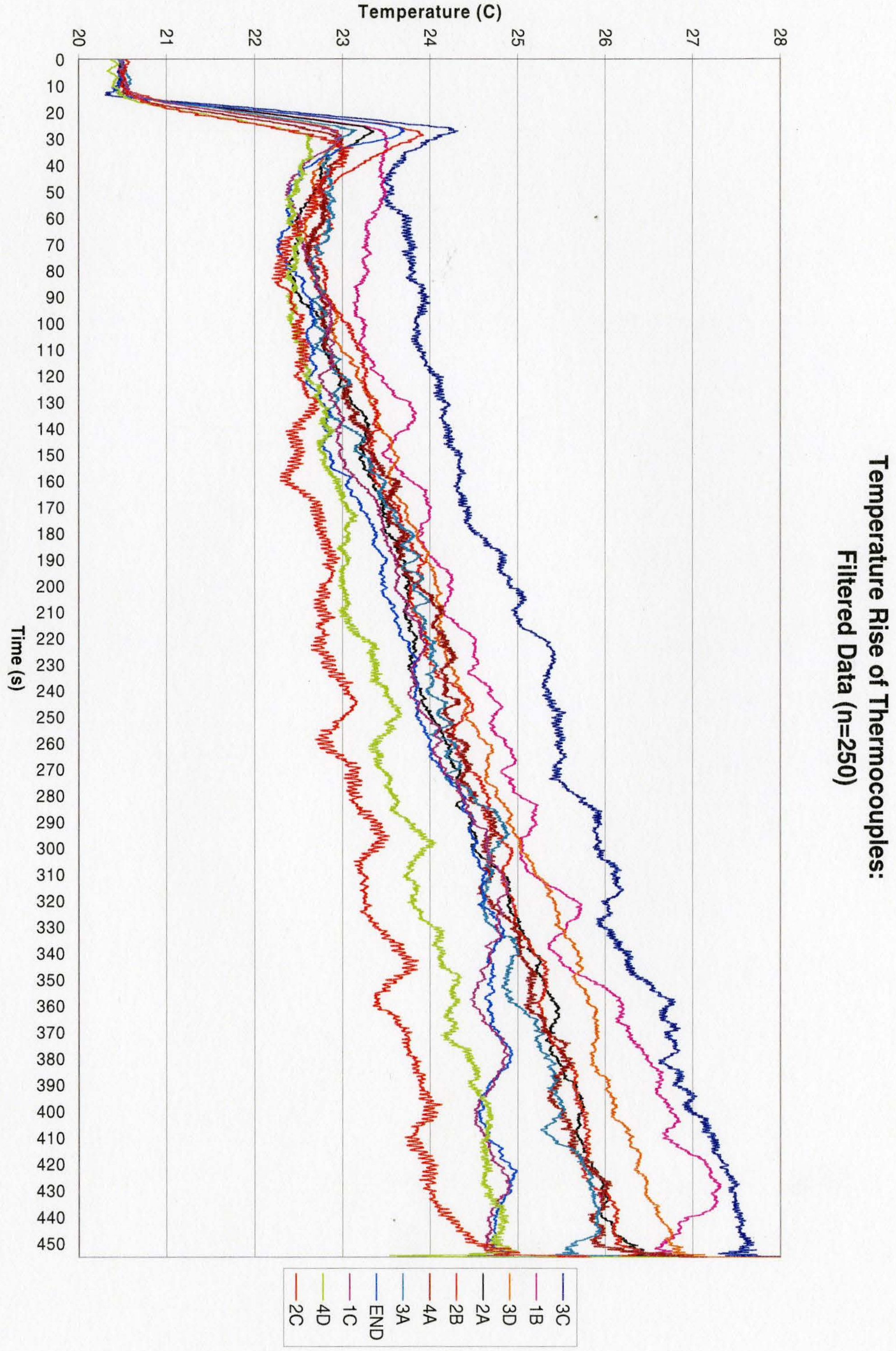

Figure 5.1.2: Steady State Test: Simple Moving Average of Raw Data (n=250)

Critical Features: Steady-State Test

The two most critical features of the thermocouple responses during the test are the rate-of-rise of temperature during motor acceleration and steady operation. The start-up response is significant because it essentially isolates the reaction of the thermocouples to inter-bar current heat generation from other heat sources and cooling effects. When the excitation is applied to the stator, there are inter-bar currents through the rotor iron causing ohmic heating. Simultaneously, heat is generated in other areas of the rotor, such as heat generated in the rotor cage bars by the bar currents. However, it takes a finite amount of time for the heat generated in other areas of the rotor to influence the thermal readings in the rotor iron at the point of the thermocouples. Additionally, any cooling effects by convection, conduction and radiation also take a finite amount of time to begin drawing heat away from the iron. As such, studying the initial temperature rise during start-up at different locations in the rotor iron should give a good indication of the heating effects of inter-bar currents.

Figure 5.1.3 shows a smaller portion of the averaged thermocouple data displayed in Figure 5.1.2, focusing specifically on the startup period of the motor when the excitation is first applied. Although the averaged data is not accurate, it does indicate that the initial rate-of-rise of temperature is different depending on the thermocouple location with reference to the rotor bars and end rings. It also clearly shows that the rotor points heat up very quickly (a direct result of inter-bar currents), then cool slightly (due to radiation, convection and conduction), before heating again as a result of external heating.

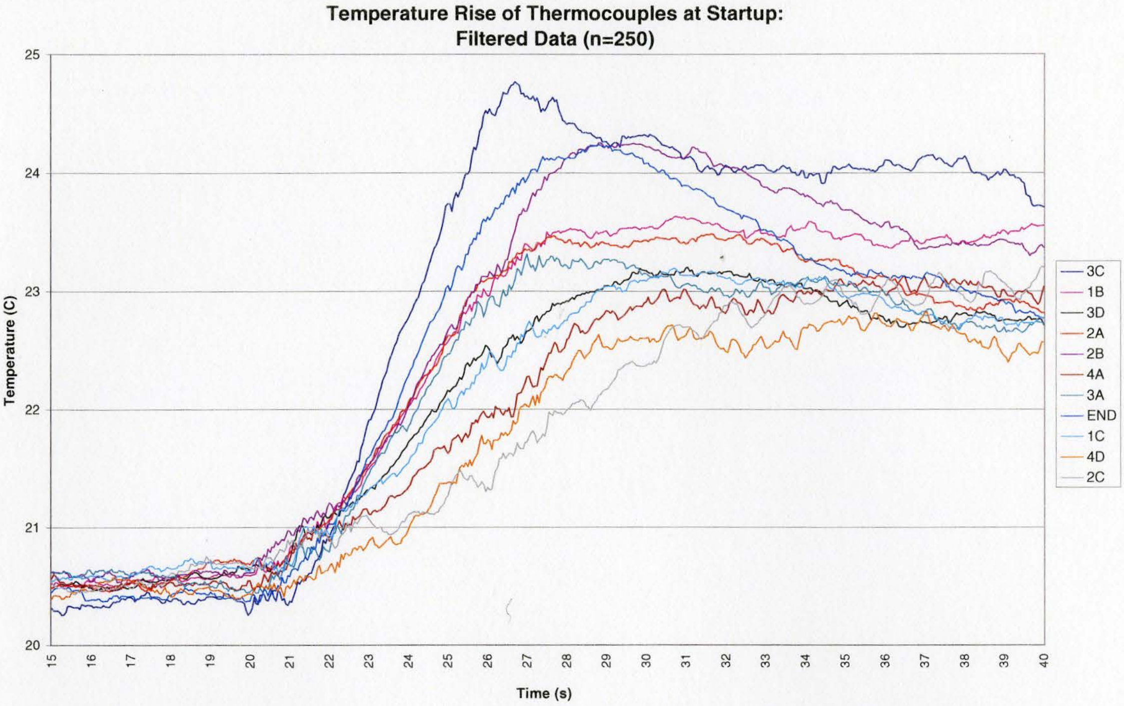

Figure 5.1.3: Steady State Test: Startup - Average Data (n=250)

The rate-of-rise of temperature during steady operation is important because it shows the net heating of the rotor iron, including heat loses due to radiation, conduction away from the rotor and convection. The rate-of-rise of temperature during steady operation can be seen in Figure 5.1.4, which is simply a segment of the averaged data in Figure 5.1.2. This graph reveals that during steady operation different areas of the rotor heat at different rates, depending on their location relative to the rotor bars, rotor surface and end ring. In this case, the rate-of-rise of each line is relatively constant, lending feasibility to the averaged model.

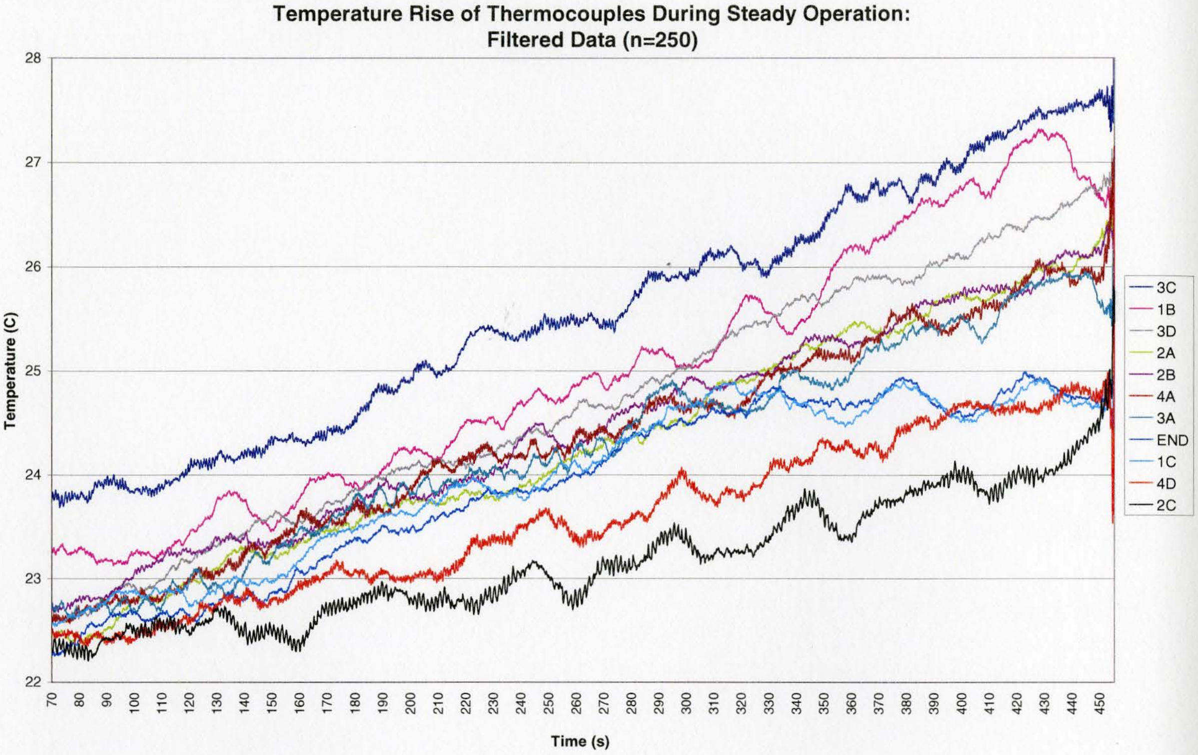

Figure 5.1.4: Steady State Test: Steady Operation - Averaged Data (n=250)

Curve Fitting: Steady-State Test

Although easy to apply to the data set, the most significant limitation of forward averaging was a skewing or modification of the data set. The simple averaging was still useful in finding a general trend in the data sets, and viewing the relative performance of the thermocouples because each dataset was skewed equally. Since a general trend does exist in the data sets, polynomial least-squares regression was used to fit polynomial curves to the data sets. The assumption is that the true instrument readings are distorted with normally distributed noise generated by the hardware precision and experimental conditions, making least-squares regression a simple and effective solution.

Each raw data set was individually used to generate a polynomial of the form

$$P(t)=c_0+c_1x+c_2x^2+\cdots+c_nx^n \tag{5.2}$$

The orders n of the polynomials for each individual set was determined iteratively by evaluating the significance of additional terms. For all data sets a polynomial of degree 20 was sufficient to capture the profile of the thermocouple responses over the relevant range, and any terms over the 20th order were negligible. Figure 5.1.5 below show the raw data sets over the first 120 seconds of the experiment with the best-fit polynomial curves overlaid. The coefficients produced for each polynomial are included in Table A.B.1 in Appendix B.

Since the data sets resemble exponential curves, least-fit models were fit to the data presented on a logarithmic scale in order to try to reduce the number of coefficients in the best-fit polynomials, and then transformed back to a linear scale. The order of the best-fit polynomial for each set was found to be n=18 using equation 5.2, with the terms beyond order 18 considered negligible. The raw data sets overlaid by these best-fit polynomials can be seen in Figure A.2.3 in with the coefficients calculated for each best-fit curve shown in Table A.B.2 in Appendix B. The most significant improvement over the direct polynomial fitting is a reduction in the order of the polynomial by two.

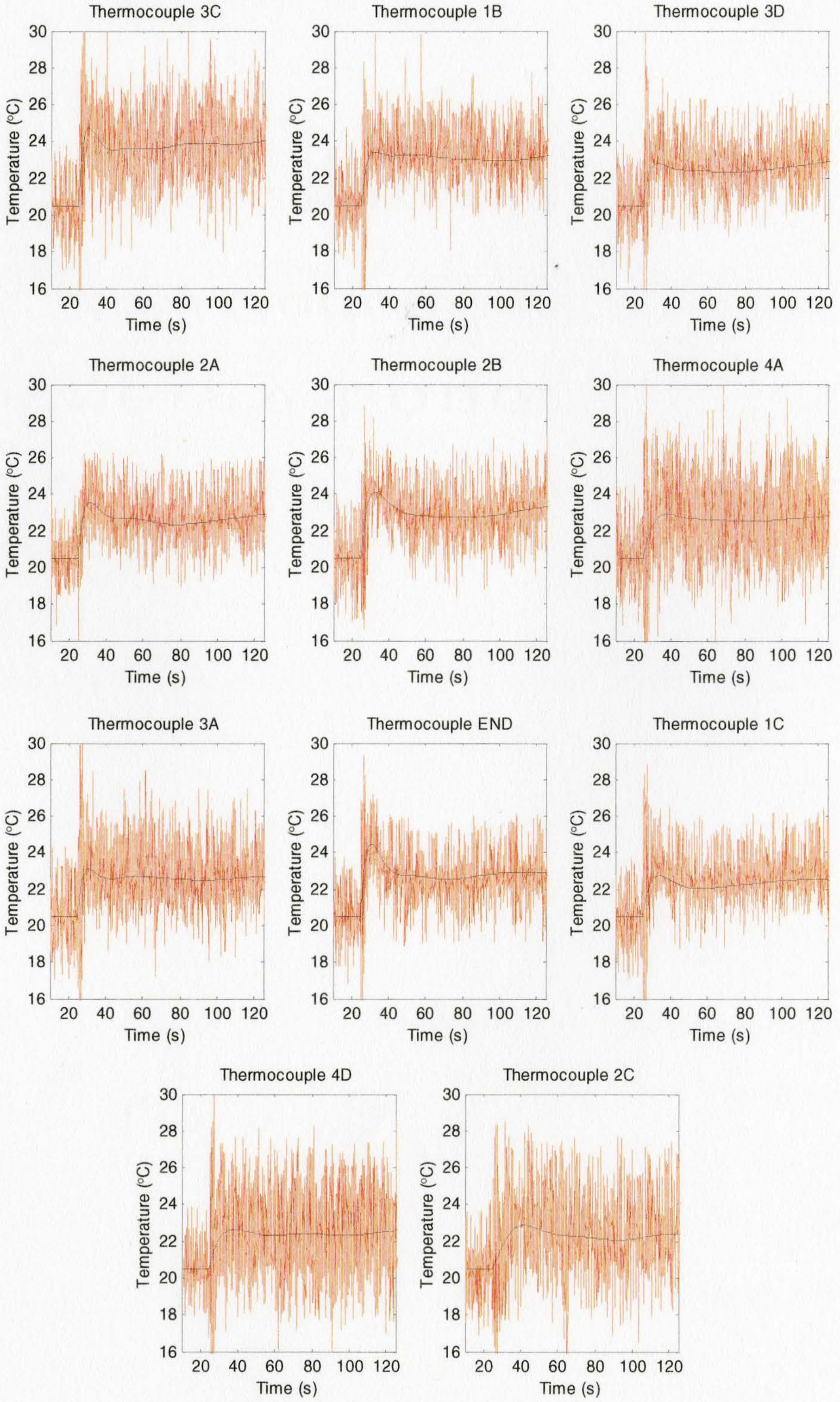
Thermocouple 3C

Thermocouple 1B

Thermocouple 3D

Thermocouple 2A

Thermocouple 2B

Thermocouple 4A

Thermocouple 3A

Thermocouple END

Thermocouple 1C

Thermocouple 4D

Thermocouple 2C

Figure 5.1.5: Steady State Test: Polyfit Curves Overlaying Raw Data Sets

5.1.2 Start-up Thermal Test Results

The start-up thermal test focuses on the temperature rise generated by inter-bar currents at various points on the rotor core specifically when the motor is accelerating. To ensure consistency and isolate the heating effects of inter-bar currents from other sources of heat the same thermocouple setup is used as in section 5.1.1 above. For the start-up test, the excitation is applied three times while the motor is at rest and two more times when the motor is rotating at speeds slightly less than full speed, as outlined in Chapter 4, Section 4.4.2. The intention of the start-up test is to capture the instantaneous rate-of-rise of temperature immediately following the generation of inter-bar currents before any other heating or cooling effects begin to affect the thermocouples.

Raw Results: Start-Up Test

The raw results of the five thermocouples used in the start-up thermal test can be seen below in Figure 5.1.6. The first three applications of the excitation to the idle motor are evident by dramatic increases in the temperatures indicated by the thermocouple. However, the temperature increase caused the final two times the excitation is applied is hardly visible in the noisy signals. Much like the raw results of the steady-state test, the data is noisy and requires smoothing or modeling to reveal the thermal trend more clearly.

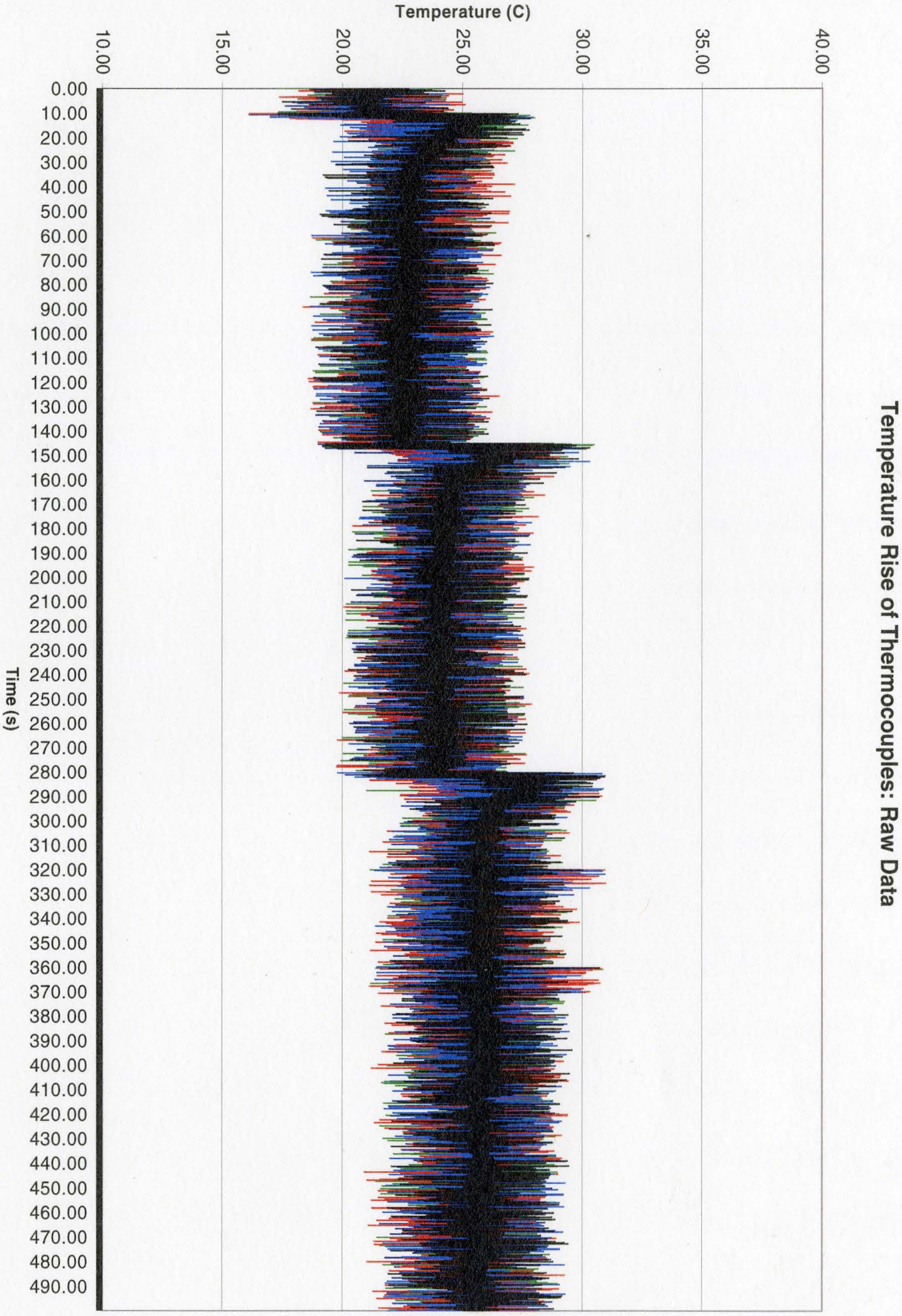

Figure 5.1.6: Start-up Test: Raw Data Output

Filtered Data: Start-Up Test

To smooth the thermocouple outputs from the start-up test and reveal the overall trend, a simple moving average dictated by equation 5.1 was used on the raw data set as a low-pass filter. Again, the assumption was made that the noise is normally distributed around the true data. Although it is known that the averaging will skew the data set slightly, a simple forward moving average will help filter the high-frequency noise from the raw data and give a good initial estimate of the true temperature values at the thermocouple locations. Since the start-up test is focusing specifically on the rate-of-rise of temperature in the rotor iron during acceleration, higher period averaging will not be considered because of the increased skewing on the data sets.

A value of $n = 250$ was used in equation 5.1 to smooth the raw data without skewing the results too significantly. The results of the averaging can be seen in Figure 5.1.7, clearly differentiating the five outputs. The variations in the rate-of-rise of each thermocouple during the first three accelerations of the motor, as well as the variation in cooling during the deceleration stages are clearly visible. Additionally, a slight response is also visible during the final two stages of the test, where the excitation is applied while the motor is decelerating. Since the averaged model is not directly useful in the analysis of the outputs because of the skewing of the initial rate-of-rise of temperature, a more accurate polynomial representation will be developed in the subsequent sections, after some of the more critical features of Figure 5.1.7 are highlighted.

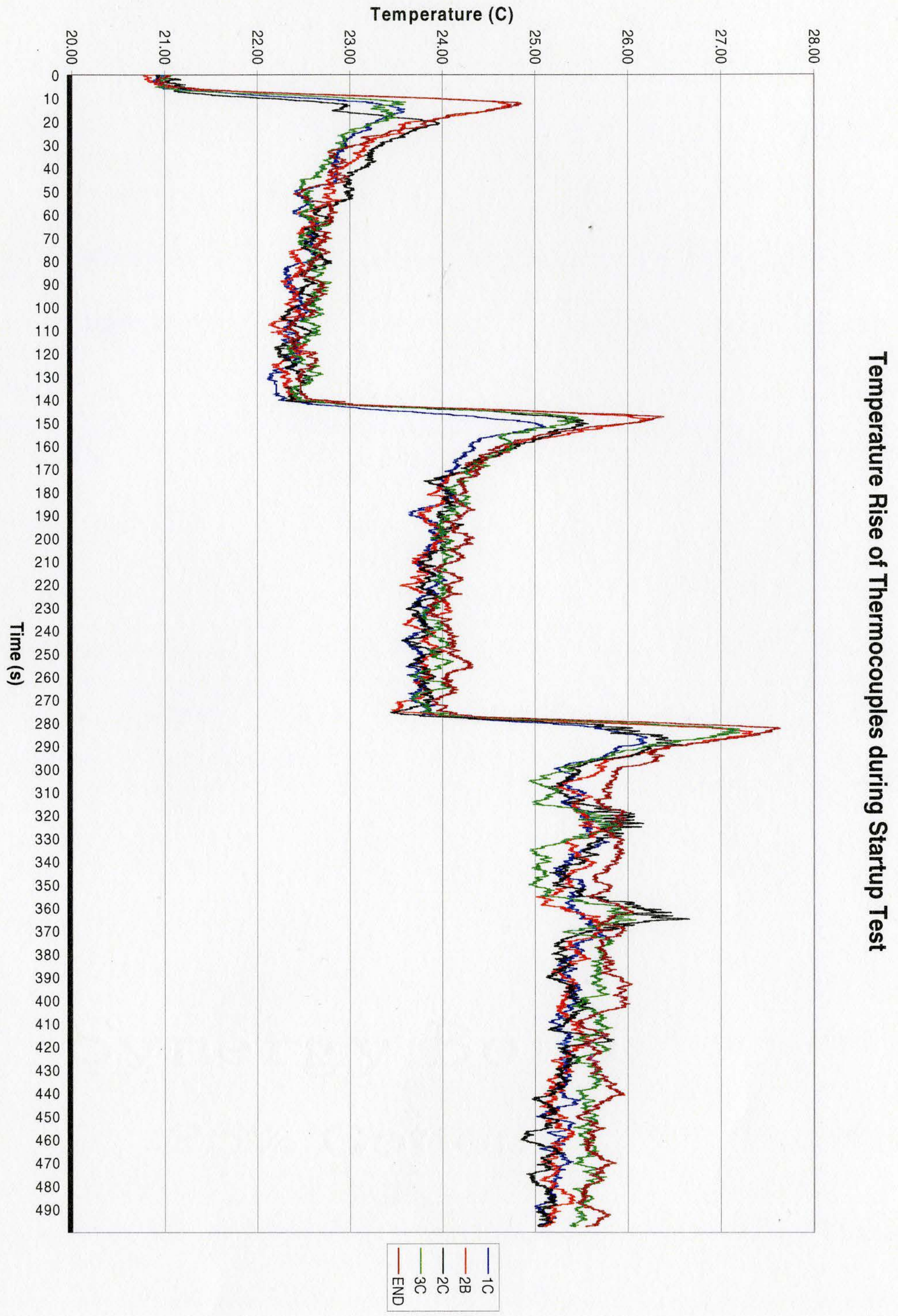

Figure 5.1.7: Start-up Test: Average of Raw Data (n=250)

Critical Features: Start-Up Test

In performing the steady-state test, the excitation was applied once allowing the motor to accelerate to full speed, and remained constant for the length of the experiment. The test emphasized the initial heat generated during start-up in comparison to the steady-state cooling effects while the motor was under power. Conversely the start-up test attempts to isolate the rate-of-rise of temperature in the rotor iron during start-up, both during full acceleration from rest and partial acceleration when the motor is rotating with some velocity.

The purpose of the start-up test is to experimentally determine whether the heat measured by the thermocouples is predominantly due to inter-bar currents, assuming that the inter-bar currents are constant during operation. If the heat rise is primarily due to inter-bar currents, the temperature rise indicated by thermocouples should be consistent regardless of the speed of the stator when the excitation is applied. If the temperature rise varies based on the speed of the motor, than two options are possible:

1. The inter-bar currents are a function of the motor speed. In particular, inter-bar currents are much higher when starting the motor from rest as compared to accelerating the motor when it is already turning.
2. The temperature rise indicated by the thermocouples is not only due to inter-bar currents.

Figure 5.1.8 below shows the five start-up stages of the experiment. The first three panels show the start-up of the motor from a complete stop. The final panel shows the last two start-up stages, when the motor was still spinning.

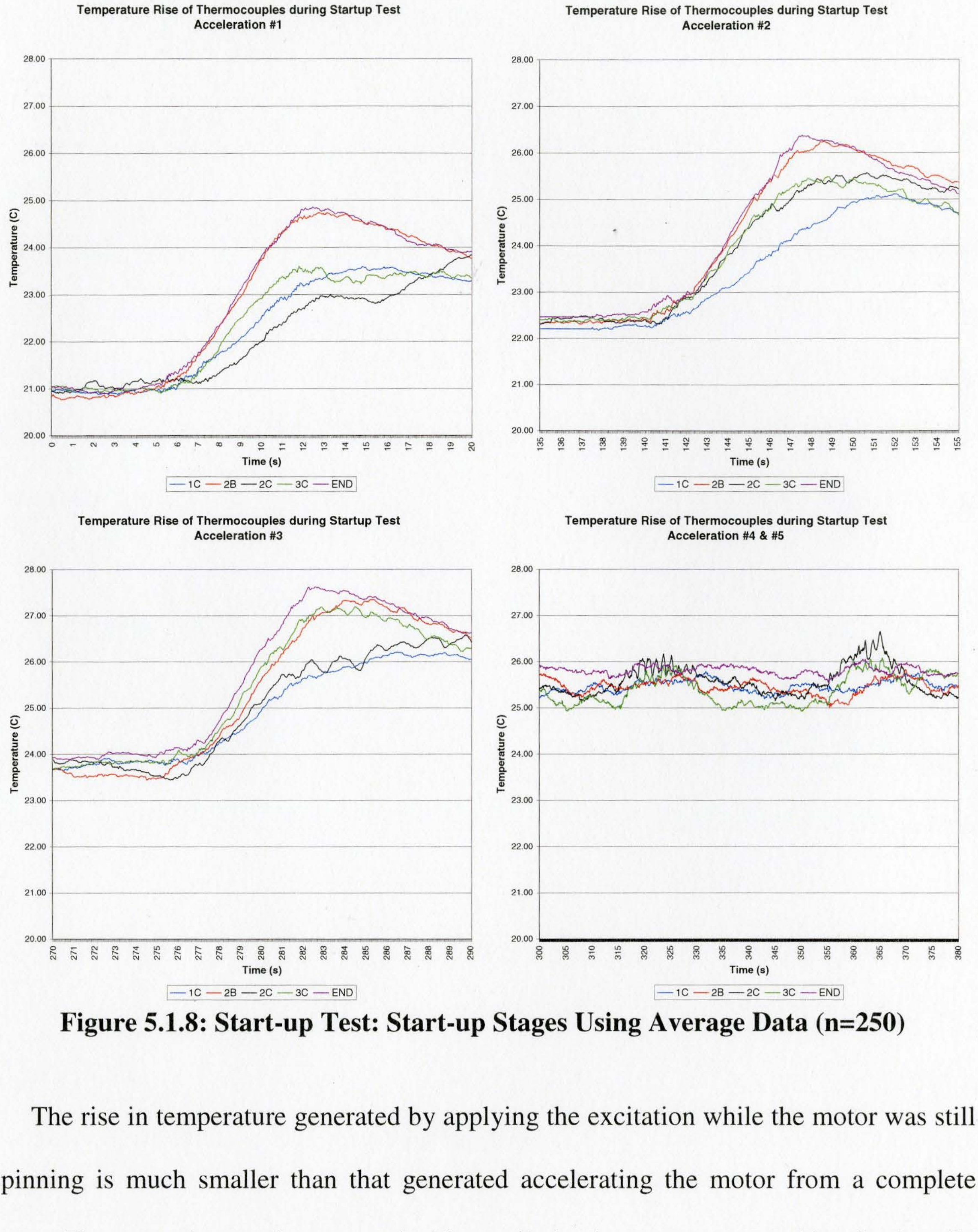
Temperature Rise of Thermocouples during Startup Test Acceleration #1

Temperature Rise of Thermocouples during Startup Test Acceleration #2

Temperature Rise of Thermocouples during Startup Test Acceleration #3

Temperature Rise of Thermocouples during Startup Test Acceleration #4 & #5

Figure 5.1.8: Start-up Test: Start-up Stages Using Average Data (n=250)

The rise in temperature generated by applying the excitation while the motor was still spinning is much smaller than that generated accelerating the motor from a complete stop. The averaging tends to smooth this small rise in temperature making it virtually indistinguishable in the fourth panel.

Curve Fitting: Start-Up Test

As with the steady-state test, the forward averaging adequately revealed the general trend in the data sets, while skewing the true response of the thermocouples. Again a polynomial least-squares regression was used to develop a polynomial that will be more useful in the analysis of the data. Since there was only a slight improvement in the logarithmic scale polynomial curve fitting as compared to the direct polynomial fitting, only the polynomial fitting was used for the start-up test. A polynomial was generated at each start-up section of the experiment for each raw data set, of the same form as equation 5.2,

$$P(t) = c_0 + c_1 x + c_2 x^2 + \cdots + c_n x^n$$

For the start-up test, the polynomials were fit over a dataset of 10 seconds, from the time the excitation was applied to the time the excitation was removed; a much smaller number of samples than used in the steady-state test. Consequently, the order of the polynomials for each startup was much lower than in the steady-state test. For the first three start-up stages, an order of *n*=9 was sufficient to capture the change in temperature over the relevant time range. Figure 5.1.9 below shows the response of each thermocouple over the first three start-up stages, overlaid by the best-fit polynomial curves. The temperature scales have been shifted to align each polynomial to the same starting datum in order to show the similarities between each starting stage. Additionally, the coefficients of the best-fit polynomials for each start-up stage for each thermocouple reading are included in Table A.B.3 in Appendix B.

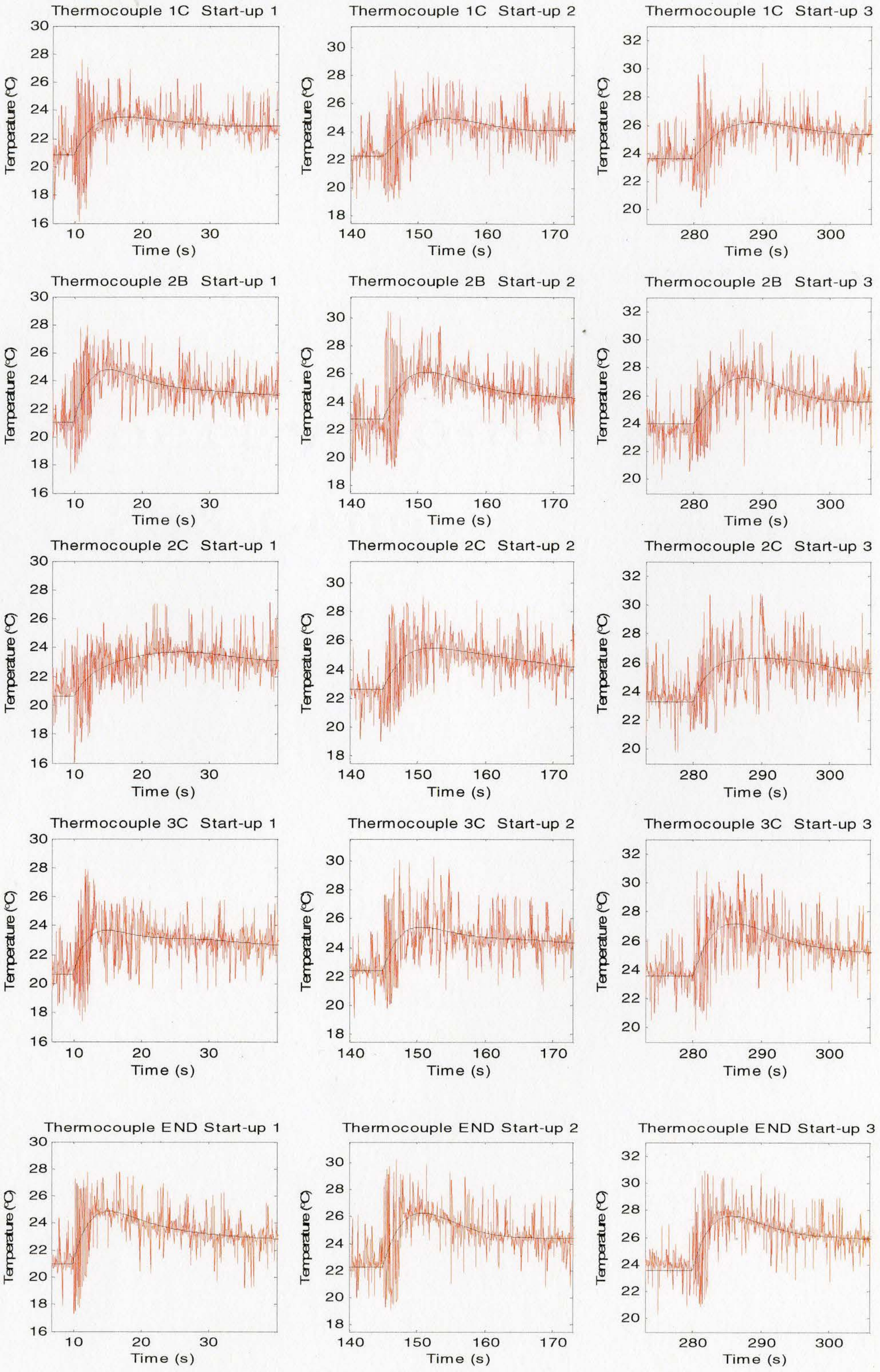

Figure 5.1.9: Polyfit Curves Overlaying Raw Data Sets

5.2 Search Coil Results

The results obtained through the thermal tests using thermocouples indirectly illustrate the effects of inter-bar currents through the heat they generate. In comparison, search coils were wound around various segments of rotor iron between adjacent rotor bars to directly measure the inter-bar currents during startup and steady-state operation. The coils were wound in such a way as to exclude the bar-current and end-ring current, only looping around the iron core.

As discussed in Chapter 4, Section 4.4.2, initial testing indicated that each search coil output was comprised of three separate sinusoidal signals at three different frequencies. Using the relative terms, low-, mid- and high-frequency, each component of the output waveform will be discussed in the subsequent sections. Additionally, the startup period of the motor will be thoroughly investigated. The signals will be displayed graphically on a time-voltage scale, and in the frequency domain on a frequency-amplitude scale.

5.2.1 Test for Low-frequency Component

The results of the preliminary tests were not sufficient to determine the low-frequency component because the sampling rate of 20 samples per second was too slow and not enough full cycles were sampled. It was necessary to increase the sampling rate of the acquisition system and the duration of the excitation. A second test was performed at 100 samples per second, where the motor excitation was applied at 5 seconds and removed 10 minutes later. The raw output of a single search coil for the first 50 seconds of this test is shown below in Figure 5.2.1.

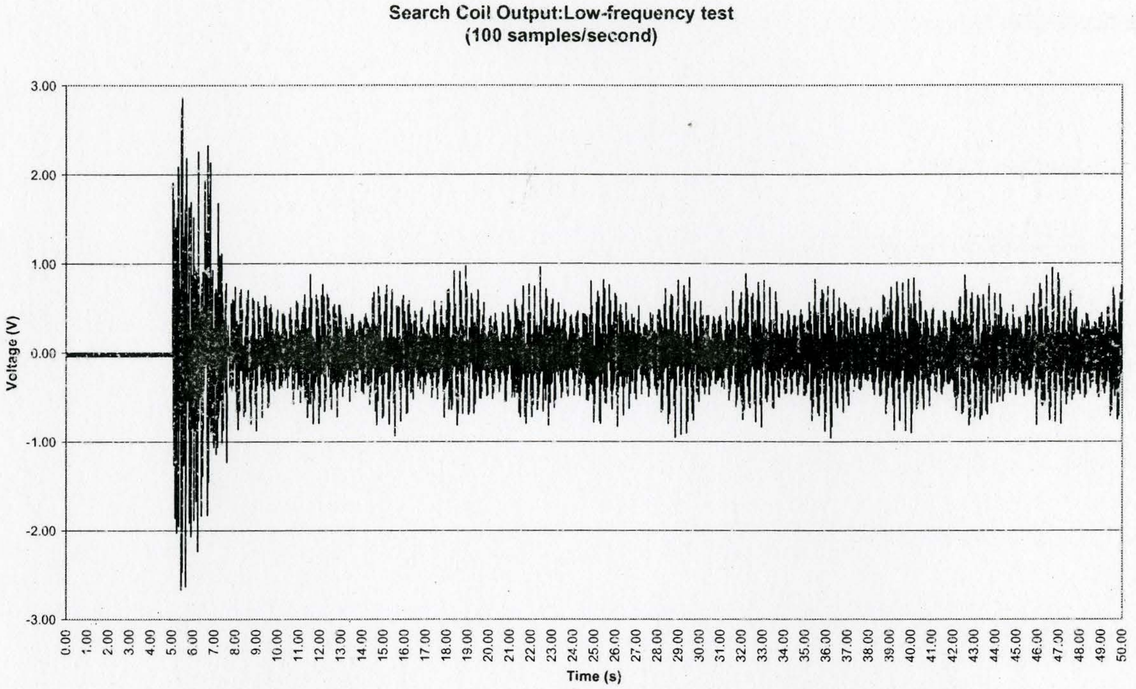

Figure 5.2.1: Low-Frequency Component of Search Coil Output

Fourier Transform for Low-Frequency Component of Signal

The test results in Figure 5.2.1 clearly indicate that the search coil output contains at least two independent frequencies. The most distinct is the low frequency sinusoid enveloping a second, less distinguishable higher frequency component. The frequency of the envelope sinusoid can be calculated using the Fourier Transform, assuming the data set contains a sufficient number of oscillations, and is sufficiently periodic. The duration of the test was 10 minutes which includes approximately 150 cycles of the envelope sinusoid; a sufficient number for the Fourier transform. Invoking the Fast Fourier Transform function for the 60000 point data set gives a frequency domain output displayed in Figure 5.2.2 over a relevant frequency range. The Fourier Transform reveals that the main modulating frequency occurs at 0.2565 hz.

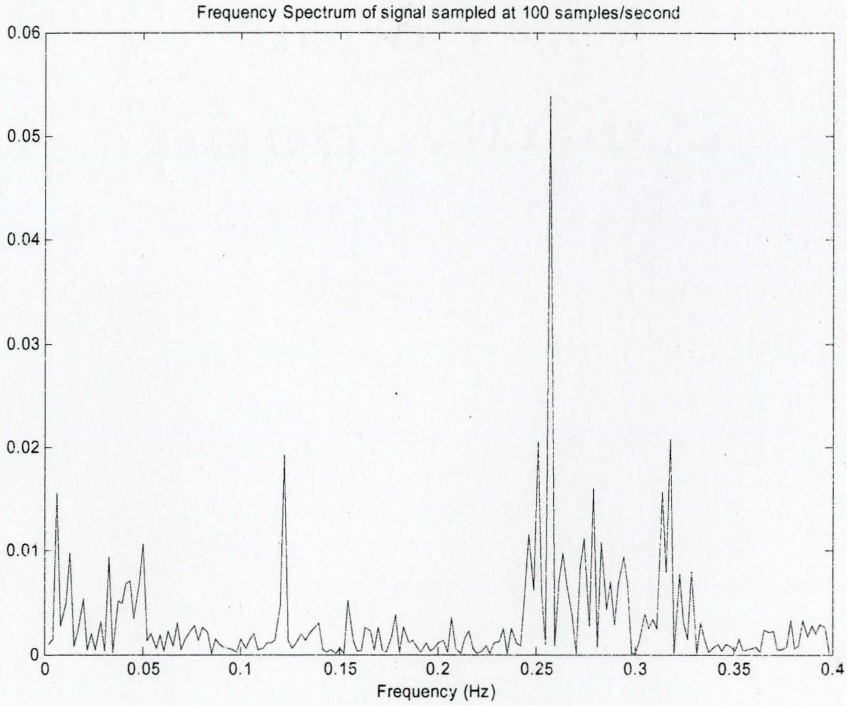

Figure 5.2.2: Fourier Transform for Low-frequency Component

5.2.2 Test for Mid-frequency Component

Figure 5.2.1 indicated that a second, higher frequency component exists in the search coil outputs. Expanding Figure 5.2.1 over a shorter time scale in Figure 5.2.3 reveals that another higher-frequency sinusoid does exist. However, the modulated component in

Figure 5.2.3 is not completely constructed and periodic, indicating that the sample rate is not sufficient to capture the full signal.

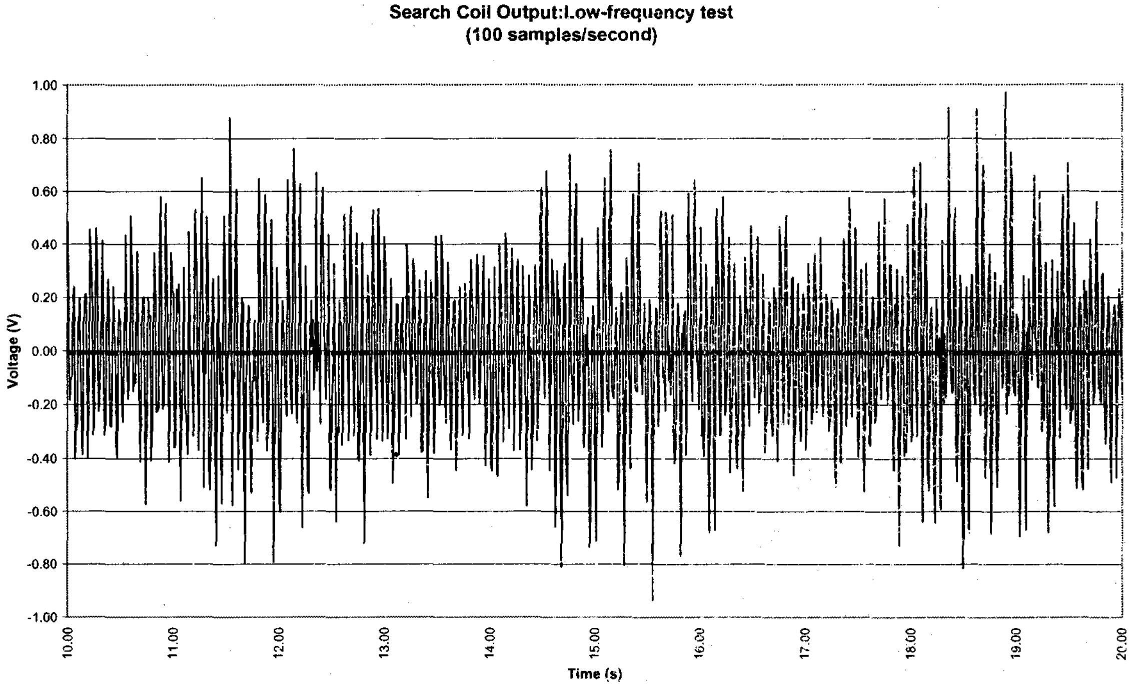

Figure 5.2.3: Test Results for Low-frequency Component of Signal

A third test was performed at 2000 samples per second to get better resolution on the modulated signal. The output of this test can be seen in Figure 5.2.4, over one half period of the low-frequency 0.2565 hz signal. In this plot, the oscillations of the higher-frequency signal are much clearer and more well-defined. Additionally, the plot of Figure 5.2.4 shows that this signal modulates another high-frequency component.

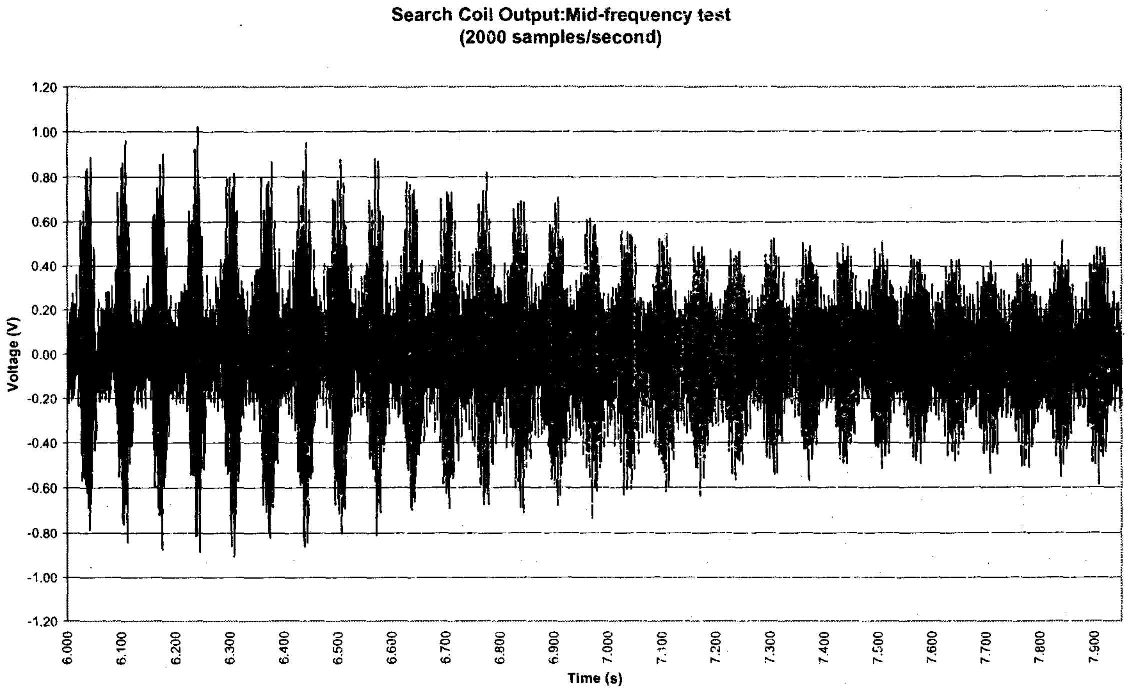

Figure 5.2.4: Test Results for Mid-Frequency Component of Search Coil Output

Fourier Transform for Mid-Frequency Component of Signal

To obtain the exact frequency of the signal, a Fast Fourier Transform was invoked on the 20,000 point data set, excluding the start-up portion of the experiment. The frequency spectrum, plotted over a relevant frequency range, is shown below in Figure 5.2.5. The frequency domain plot indicates that the mid-frequency component exists at 14.89hz. In this case, the frequency domain plot of Figure 5.2.5 shows a very definitive spike at because the data set contained several clearly defined oscillations of the component.

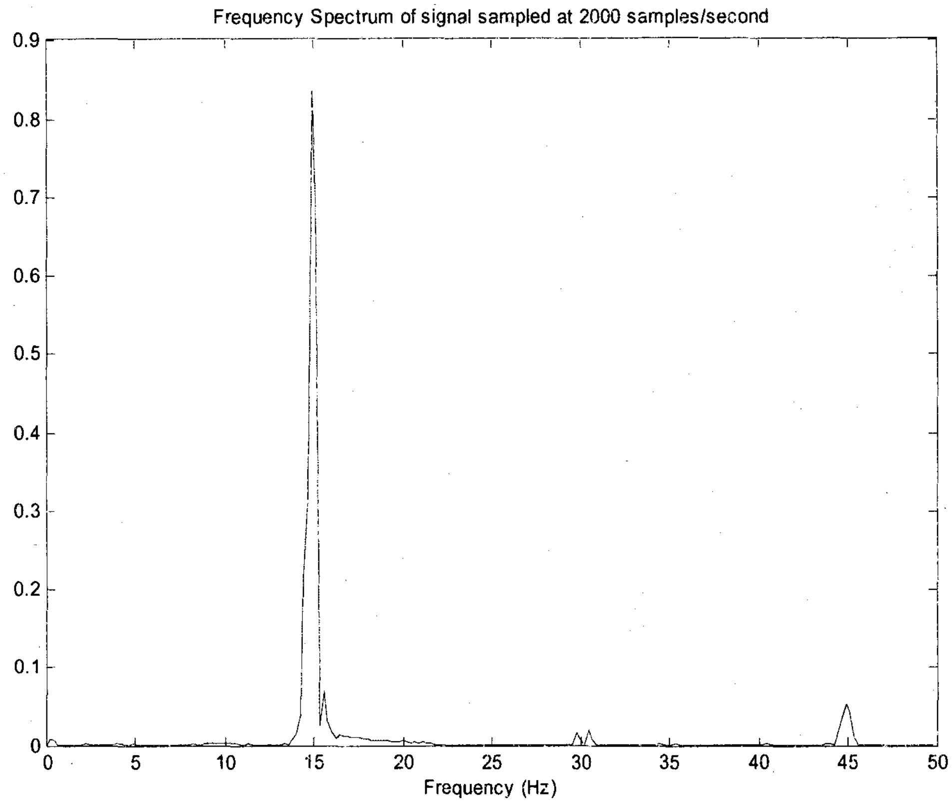

Figure 5.2.5: Fourier Transform for Mid-frequency Component

5.2.3 Test for High-frequency Component

Figure 5.2.4 indicated that a third, high-frequency component exists in the search coil outputs, modulated by the mid-frequency component. To resolve the component more clearly, Figure 5.2.4 is expanded over the time range of 6.010 to 6.070 seconds in Figure 5.2.6, encompassing one full cycle of the mid-frequency component. The high frequency component can be seen in this plot, although the signal looks distorted and irregular, indicating that the sampling frequency is not sufficient to capture the signal.

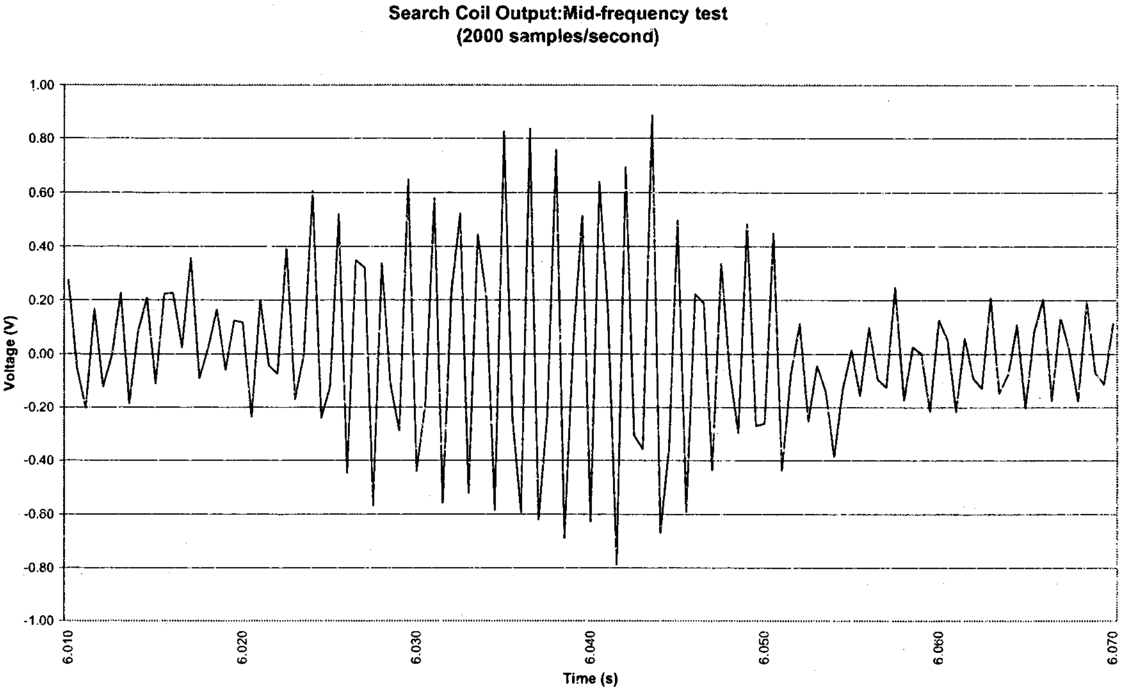

Figure 5.2.6: Test Results for Mid-frequency Component

A test was performed at 10,000 samples per second to get better resolution on the high-frequency signal. The motor excitation was applied before the data acquisition system was started because of the extremely fast sampling rate. Once the motor reached full speed, the acquisition system was turned on for 6 seconds, generating a 60,000 point data set. The output of this test can be seen in Figure 5.2.7 over one entire period of the mid-frequency signal.

The high-frequency sinusoid is clearly visible in this plot. The high-frequency components deviation from an ideal sinusoid is most likely a combination of sampling noise in the acquisition system, as discussed in Chapter 4, section 4.3, and a sample rate that is still too low. At a sample rate of 10,000 samples per second, the acquisition system samples the high-frequency component approximately 15 times each cycle partially explaining the variation from an ideal modulated sinusoid.

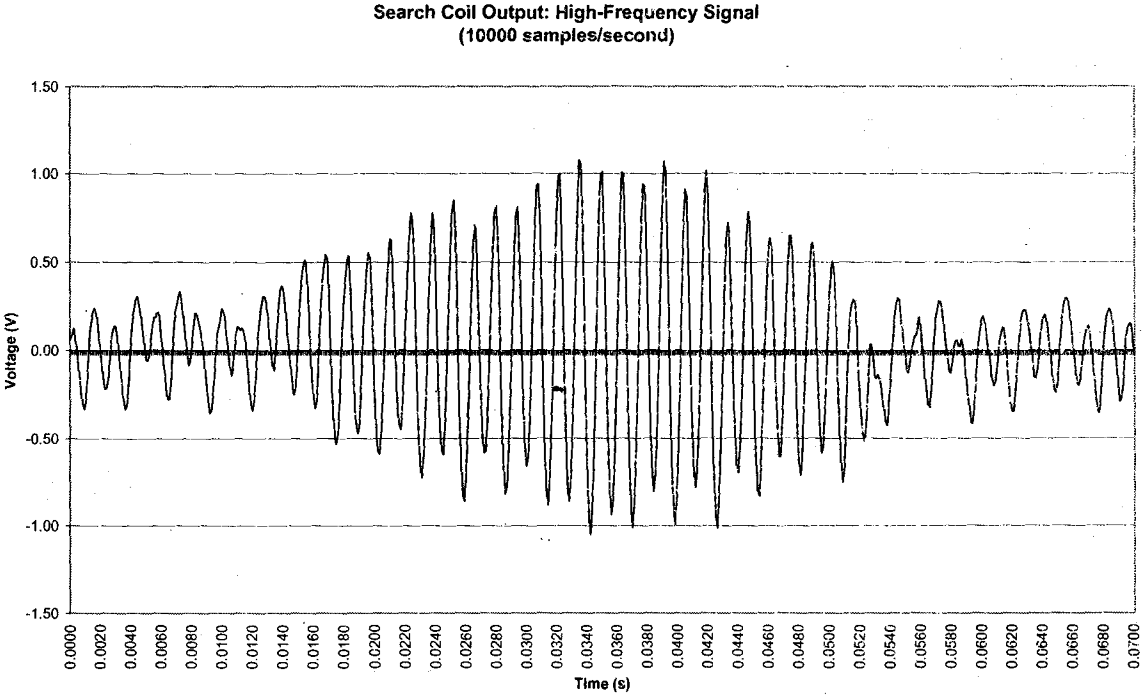

Figure 5.2.7: Test Results for High-Frequency Component of Search Coil Output

Fourier Transform for High-Frequency Component of Signal

Again, a Fast Fourier Transform was invoked on the 60,000 point data set to obtain the exact frequency of the high-frequency sinusoid. The frequency spectrum, plotted over a relevant frequency range, is shown below in Figure 5.2.8. According to the Fourier Transform, the high-frequency component exists at a frequency of 718.60hz. The smaller frequency spikes around 700hz and 740hz are result of the sampling rate and acquisition system noise, but are much smaller in magnitude than the main spike at 718.60hz.

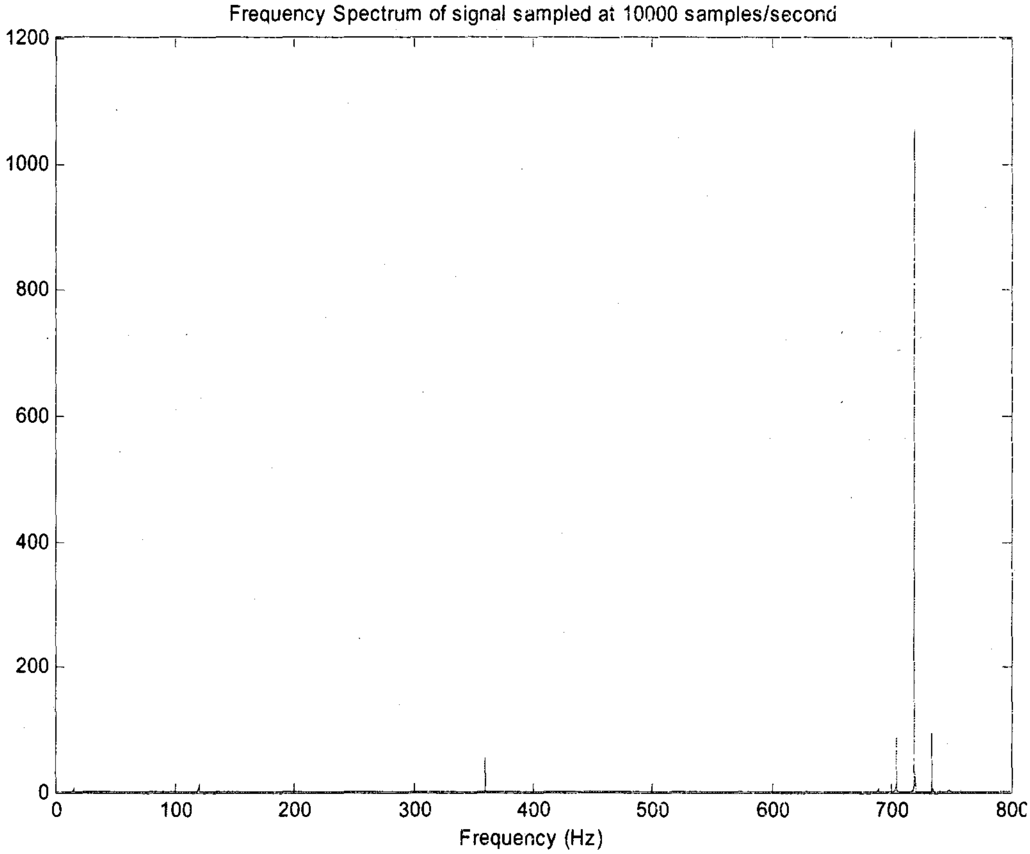

Figure 5.2.8: Fourier Transform for High-frequency Component

5.2.4 Direct Measurement Results During Acceleration

During acceleration, the values acquired from the search coils differ from those obtained during steady-state operation. Figure 5.2.9 below shows the readings from a single search coil for the first three seconds after the excitation is applied to the motor.

Note the composition of the waveform changes as the motor accelerates indicating the search coil output is a function of the motor speed. The magnitude of the waveform for the first 2.5 seconds of start-up is also approximately 3 times the steady state value, reflecting the high starting current required to accelerate the stator, and that inter-bar currents are indeed a function of the motor speed.

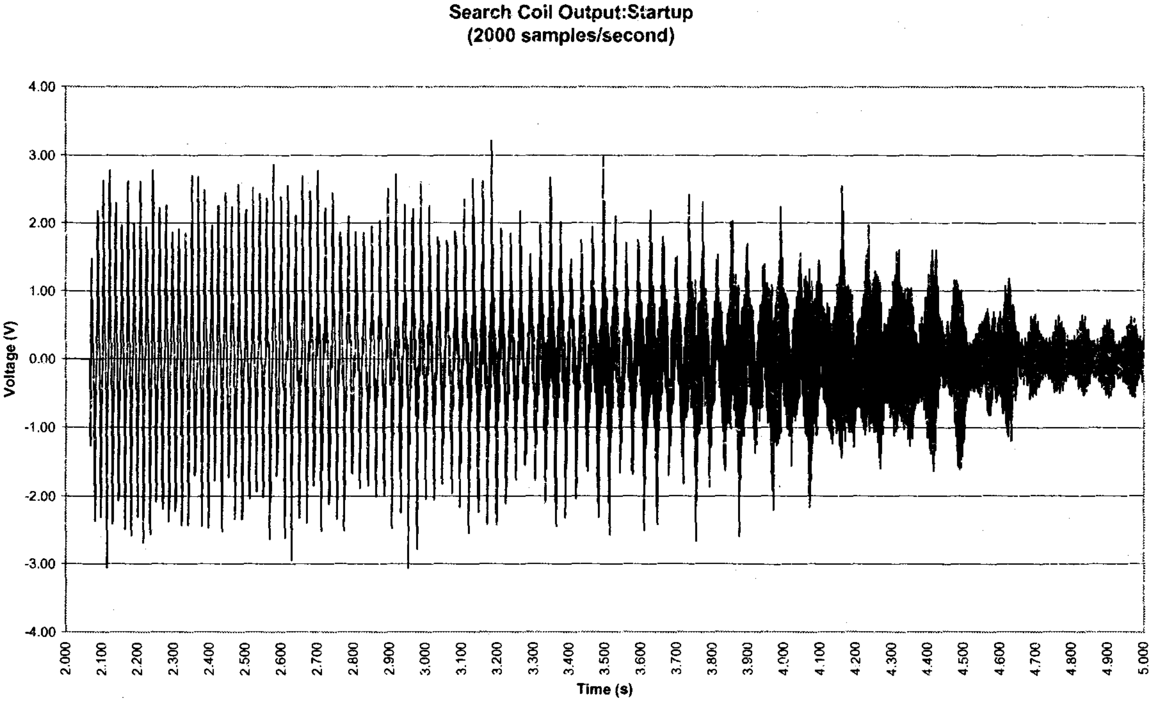

Figure 5.2.9: Search Coil Readings During Startup at 2000 samples/second

To present the search coil outputs more clearly, Figure 5.2.9 is dissected into three separate graphs; from 2.000 to 3.000 seconds, from 3.000 to 4.000 seconds, and finally from 4.000 to 5.000 seconds in Figures 5.2.10, 5.2.11 and 5.2.12 respectively.

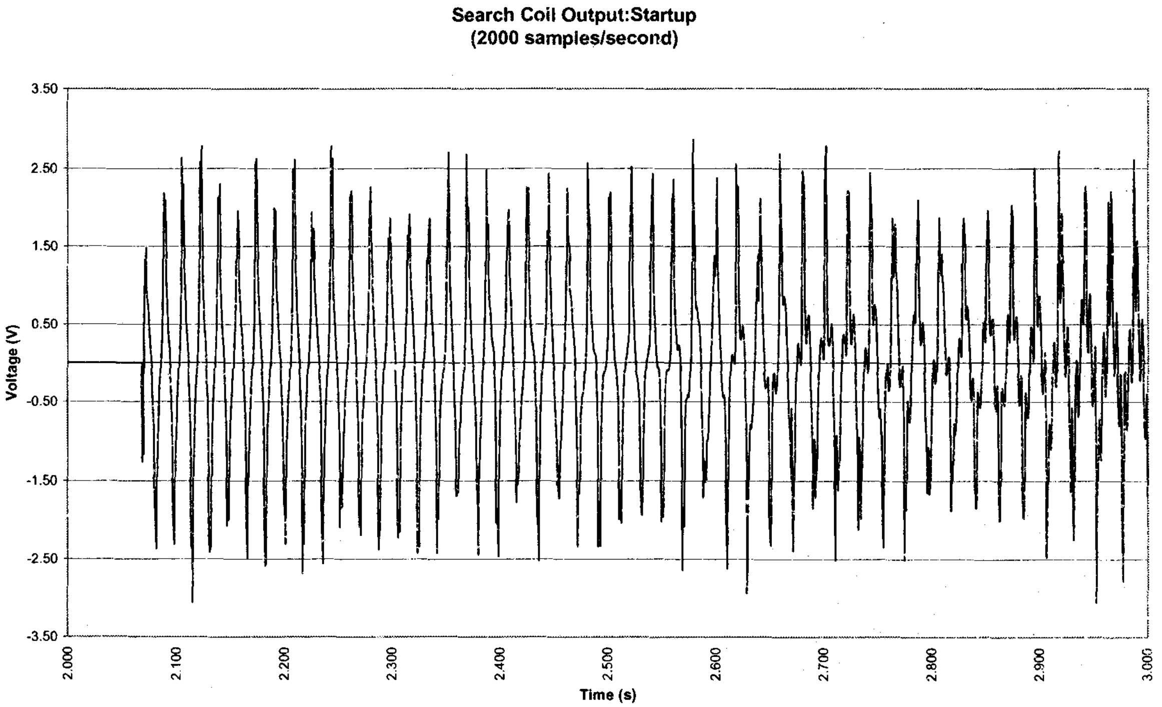

Figure 5.2.10: Search Coil Output: 1st Second of Startup (2000 samples/second)

Figure 5.2.10 shows the output of a single search coil during the first second of startup. During the first half second, from 2.050 to 2.505 seconds, the waveform cycles approximately 25 times, yielding a frequency of 50hz. At this point the motor begins to accelerate, corresponding to the visibility of a second, higher-frequency component. As the motor gains speed, the higher-frequency wave becomes more visible, and the original 50hz wave begins to slow down.

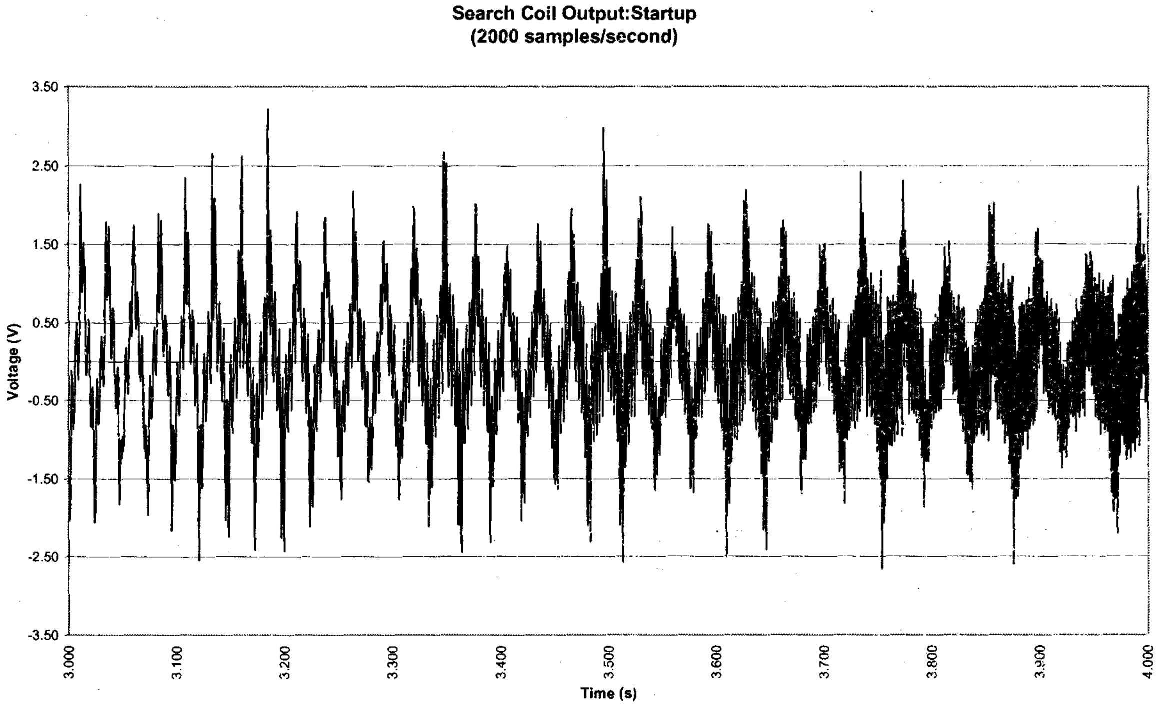

Figure 5.2.11: Search Coil Output: 2nd Second of Startup (2000 samples/second)

Figure 5.2.11 is a continuation of Figure 5.2.10 from 3.000 to 4.000 seconds. The higher-frequency wave becomes more prominent at around 3.200 seconds, and the original low-frequency 50hz component continues slide to a lower frequency. From 3.500 to 4.000 seconds, the low-frequency component oscillates 13 times, at an average frequency of 25hz. However the higher-frequency wave at 4.000 seconds has a higher amplitude than at 3.000 seconds. Both the original component and the higher-frequency component become clearly enveloped by a slow 6hz component.

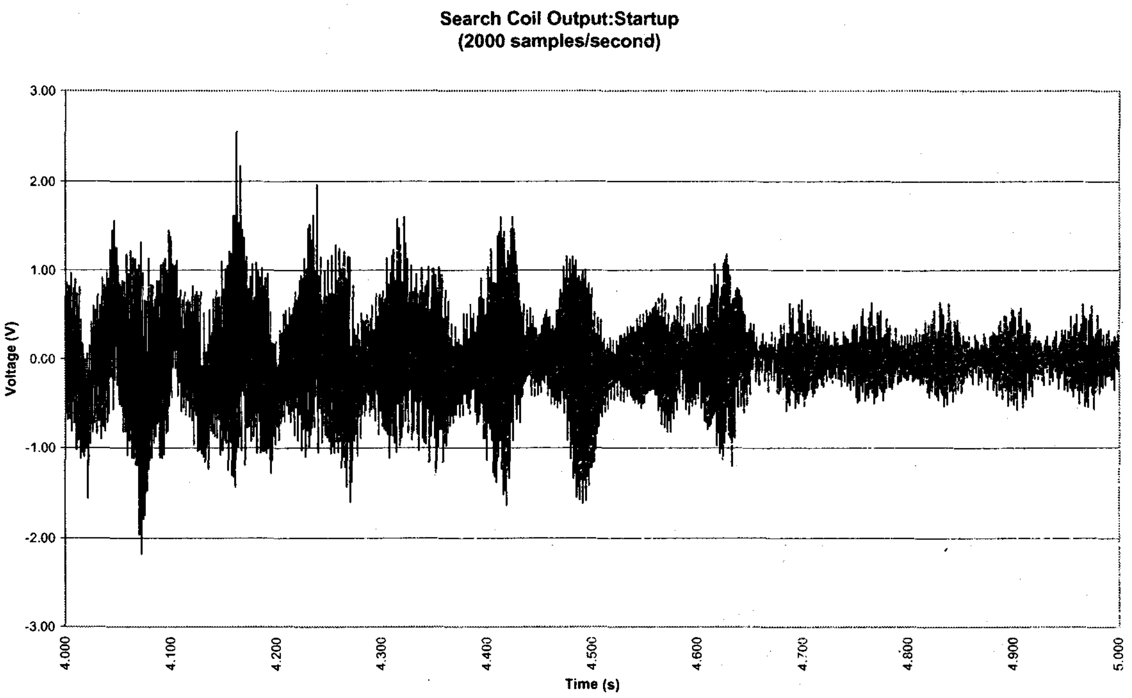

Figure 5.2.12: Search Coil Output: 3rd Second of Startup (2000 samples/second)

Figure 5.2.12 illustrates the final half second of startup, a continuation of Figure 5.2.11. The search coil output begins to resemble the steady state waveform, as the slow 6hz envelope approaches the steady-state 15hz signal modulating the high-frequency 715hz component. Considering the results from the search coil indicate sliding frequencies during acceleration, this portion of the data is not directly useful to the analysis of inter-bar currents, at least within the scope of this body of work. In order to capitalize on the Fourier Transform and analyze the results in the frequency domain, a stable, repeatable and periodic data set is required.

Chapter 6

Analysis of Experimental Results

The results presented in Chapter 5 established a datum for experimentation related to the heating effects of inter-bar currents and the frequency components of the main field flux. An analysis of the results of both the thermal and direct measurement tests will be presented in this chapter with respect to inter-bar currents. In the case of the thermal tests, the responses of thermocouples in different locations will be used to postulate the inter-bar current distribution, and from that develop a thermal distribution in the rotor iron. Additionally, using the polynomials fit to the raw thermal data, inter-bar currents will be mathematically calculated using the rate-of-rise at start-up. An analysis of the individual frequency components of the search coil outputs will also be presented. After each test, a discussion of experimental constraints and data anomalies will be presented.

The two thermal tests and the direct measurement test used fundamentally different principles to try to experimentally determine the presence, magnitude, distribution and effects of inter-bar currents. In regards to the thermal tests, their design was intended to correlate the heat generated in strategic areas of the rotor iron to inter-bar currents using ohmic heating equations. In particular, the rate-of-rise of temperature of the rotor iron during the initial seconds of acceleration gives a good indication of the heat produced by inter-bar currents independent of other heat sources. As a supplementary benefit, the thermal instrumentation is electrically and magnetically robust; ideal for placement in the motor's strong electromagnetic field. Unfortunately, although the thermal tests can indicate the effects of inter-bar currents, the true current path, frequency components and current waveform are difficult to determine because of the relatively slow thermal response of the acquisition system.

To complement the thermal tests and compensate for the disadvantages with the thermal tests presented above, custom search coils were wound around rotor iron segments to directly measure the induced voltage due to the magnetic flux,

$$e_{\phi} = N\frac{d\phi}{dt} \tag{6.1}$$

where

e_{ϕ} = Induced voltage (V)

ϕ = Flux (Wb)

N = Number of turns

When properly wound around the rotor core, the search coils act like current transformers, creating secondary output signals proportional to the inter-bar currents, based on the number of turns of the coils. The search coil outputs have an extremely fast response time, limited only by the sampling speed of the acquisition system, and provide insight into the waveform and frequency components of inter-bar currents. Additionally, the true current distribution between adjacent rotor bars can be determined by dissecting the iron core into smaller pieces with individual search coils. However, search coils are also extremely susceptible to electromagnetic noise and interference, making it challenging to isolate desired components from other induced quantities.

6.1 Thermal Test Results

Two general thermal tests were performed: the steady-state and start-up tests. The two different thermal tests were designed to compare the thermal response of the rotor during six different operating stages:

1. Acceleration from rest
2. Steady-state operation
3. Acceleration at approximately 75% full speed
4. Multiple consecutive accelerations from rest
5. Cooling during deceleration
6. Cooling while at rest

The raw results of the steady-state tests show a sharp rise in temperature correlated to the application of the excitation when the motor is at rest. During steady operation, when the excitation is maintained and the motor is allowed to spin freely, the temperature of the rotor rises at a much slower rate than during initial acceleration until a steady-state temperature is reached. The rate-of-rise of temperature is much smaller during steady-state operation because various cooling effects draw heat away from the rotor core, and sources of heat are relatively small because the motor is not under load. When the excitation is removed, there is little difference in the rate of cooling during deceleration compared to when the motor is at rest, likely because the rotor is stationary reducing the effectiveness of the end-ring cooling fins and other cooling mechanisms.

The start-up test reveals that the rate-of-rise of temperature during multiple consecutive acceleration stages from rest all result in a dramatic increase in temperature of approximately the same magnitude, regardless of the initial starting temperature.

However, the temperature increase resulting from the application of the excitation while the motor was rotating at approximately 75% of full speed generated very little increase in temperature. These results indicate that the rate-of-rise of temperature during acceleration is a function of the motor speed, suggesting that inter-bar currents may not be constant during motor operation.

6.1.1 Rate-of-Rise Calculations

The fundamental principle behind the thermal tests is that the rate-of-rise of temperature in the rotor iron during acceleration is primarily due to inter-bar currents. This is because the ohmic heating generated by the inter-bar currents flowing through the rotor iron occur relatively fast compared to the cooling effects. The primary sources of cooling are conduction through the rotor iron and rotor bars, convection through the air gap and radiation, which all have a significantly slower response time than the initial heating effects from inter-bar currents. Additionally, the resistive and inductive heat generated in other areas of the rotor such as in the rotor bars and stator will also affect the iron core through convection, conduction and radiation at a much slower rate than from the inter-bar currents directly. Consequently, the rate-of-rise of temperature at various points in the rotor iron during acceleration will give a good indication of the magnitude of inter-bar currents, assuming the bar-to-bar resistance is known.

Graphical Rate-of-Rise Results

The raw thermal data sampled by the data acquisition system was too noisy to be used directly for analysis, so least-squares polynomials were fit to the data for analysis. Using the best-fit polynomials calculated directly from the data sets, a plot was generated focusing specifically on the rate-of-rise of each thermocouple for the first several seconds after the excitation was applied to the motor. Figure 6.1.1 shows a plot of the best-fit polynomials during first 15 seconds of the experiment, starting just before the excitation was applied, continuing through the three seconds of acceleration and eventually reaching full speed.

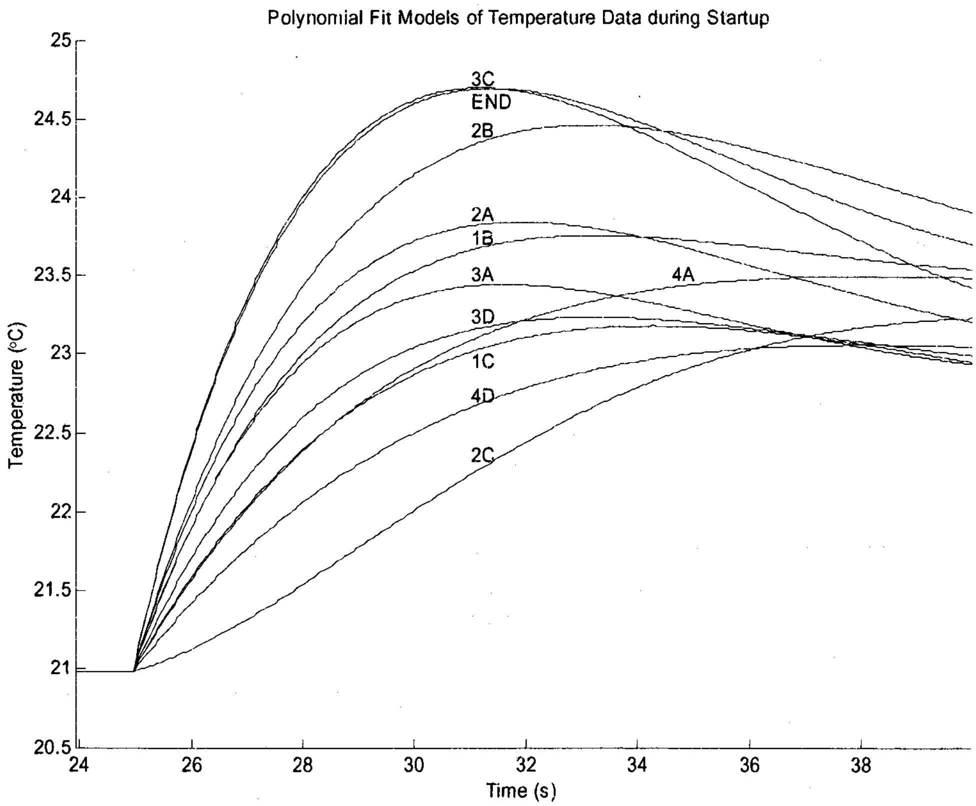

Figure 6.1.1: Rate-of-Rise of thermocouples during startup: Steady-state test

The results in Figure 6.1.1 clearly show that the rate-of-rise of temperature during acceleration is drastically affected by the thermocouple locations, indicating that the presence and magnitude of inter-bar currents are dependent on geometric position. To give a better understanding of the varying thermocouple responses, the physical locations of the eleven thermocouples are shown in Figure 6.1.2, highlighting their positions relative to the rotor bars, the end-rings and the rotor iron surface.

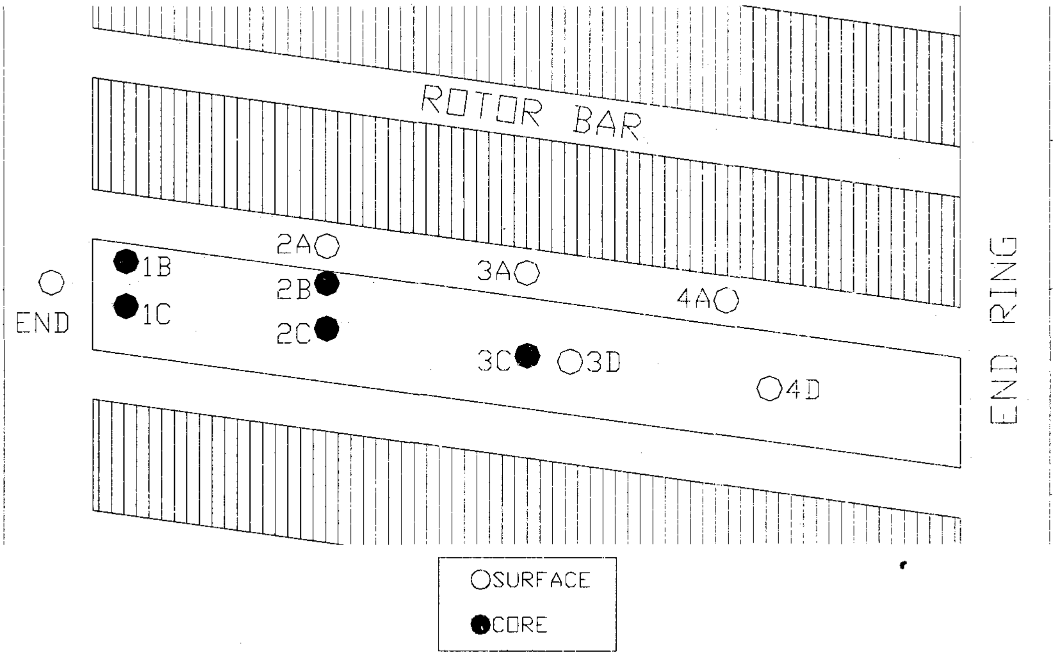

Figure 6.1.2: Rotor Thermocouple Locations

The responses of the thermocouples during the first three stages of acceleration during the start-up test are included in Appendix B for comparison to the steady-state test. The responses consistently agree with the results of Figure 6.1.1 for the steady-state test, indicating that the location of the thermocouples in the rotor iron considerably affects its response during start-up. In both the steady-state and start-up tests, for almost all thermocouples the temperature rise during acceleration reached a high peak value approximately 5 seconds after the excitation was applied. At this point, the various cooling effects began to draw heat from the thermocouple locations, cooling the rotor down. Approximately 15 seconds after the excitation is applied, the temperature begins to rise again, as a result of the additional heat generated by other heat sources in the rotor.

Figure 6.1.1 reveals that in general, during acceleration the thermocouples located directly adjacent or above the rotor bars, namely the *A* and *B* positions, experience the fastest increase in temperature. In comparison, the thermocouples located in the rotor iron or on the iron surface directly between adjacent rotor bars, namely the *C* and *D* positions, have a lower rate-of-rise of temperature during start-up. The most significant exception to this in all cases is thermocouple 3C which consistently experiences a rapid increase in temperature compared to the other *C* and *D* position thermocouples. Thermocouple 3C is embedded directly in the rotor iron at a depth of approximately half the rotor bar height, at the mid-point between two rotor bars.

Thermocouple Rates-of-Rise Based on Experimental Results

Using the polynomials developed to model the thermocouple responses, a mathematical expression for the rate-of-rise of each thermocouple can be obtained by taking the first derivative of the expressions. A plot of the first derivatives is included in Appendix B. The maximum rate of change of temperature occurs at the instant the excitation is first applied. The actual peak value of the rate-of-rise of temperature for each thermocouple is shown in Table 6.1.

	Thermocouple										
	3C	**End**	**2B**	**2A**	**3A**	**1B**	**3D**	**4A**	**1C**	**4D**	**2C**
Rate-of-Rise (°C/s)	2.135	1.882	1.357	1.331	1.220	1.209	0.862	0.690	0.687	0.538	0.489

Table 6.1: Maximum Rate-of-Rise of Temperature

The average value of the inter-bar current can be directly related to the rate-of-rise of temperature at any given point through equation 3.7:

$$I^2 = \frac{cm}{R}\frac{dT}{dt} \rightarrow I = \sqrt{\frac{cm}{R}\frac{dT}{dt}}$$

c = the specific heat capacity of the composite $(J/kg \cdot {}^\circ K)$

m = the mass of the material (kg)

R = the electrical resistance between adjacent rotor bars

For iron, the specific heat capacity is 450 $J/kg \cdot {}^\circ K$, the mass is approximately 7500 kg/m^3, and the volume of iron between adjacent rotor bars is $19.9x10^{-6}$ m^3. Equation 3.7 is then:

$$I = \sqrt{\frac{cm}{R}\frac{dT}{dt}} = \sqrt{\frac{450 \cdot 7500 \cdot 19.9x10^{-6}}{40x10^{-6}}\frac{dT}{dt}}$$

However, since the thermocouples are only measuring the temperature increase at a single point, the actual volume of material being heated is much less than the total volume of iron between adjacent rotor bars. An approximate volume of 0.5cm^3 will be used as the volume of mass affecting each thermocouple. Equation 6.1 then becomes:

$$I = \sqrt{\frac{450 \cdot 7500 \cdot 125x10^{-9}}{R}\frac{dT}{dt}} = \sqrt{\frac{0.422}{R}\frac{dT}{dt}}$$

Using an industry assumption that the inter-bar resistance is 40μΩ across a potential inter-bar current path, equation 6.2 is then:

$$I = \sqrt{\frac{3.375}{40x10^{-6}}\frac{dT}{dt}} = \sqrt{10547\frac{dT}{dt}} = 102.7\sqrt{\frac{dT}{dt}}$$

Using the rate-of-rise of temperature values presented in Table 6.1, the magnitude of inter-bar currents required to achieve the temperature are presented in Table 6.2 below:

	Thermocouple										
	3C	**End**	**2B**	**2A**	**3A**	**1B**	**3D**	**4A**	**1C**	**4D**	**2C**
Rate-of-Rise (°C/s)	2.14	1.88	1.36	1.33	1.22	1.21	0.86	0.69	0.69	0.54	0.49
Current (A)	150.1	140.9	119.6	118.5	113.4	112.9	95.3	85.3	85.1	75.3	71.8
Power (W)	0.90	0.79	0.57	0.56	0.51	0.51	0.36	0.29	0.29	0.23	0.21

Table 6.2: Inter-bar Current Magnitudes and Electrical Power

The values in Table 6.2 are only valid for the initial few seconds after the excitation is applied, while the heating effects of inter-bar currents are isolated. The effects of inter-bar currents become masked by other heating and cooling effects after approximately three seconds.

6.1.2 Current and Thermal Distribution

Based on the different rates-of-rise of temperature at various points in the rotor iron, the proposed inter-bar current paths during acceleration are shown in Figure 6.1.3. The figure highlights that inter-bar currents are most prevalent in the middle section of the rotor iron, based on the thermal data acquired through the thermal experiments. In the regions close to the end rings, inter-bar currents seem to have a lesser effect based on the thermal rise in those areas. This is most likely because the path of least resistance in this region is through the end-rings as opposed to the rotor iron.

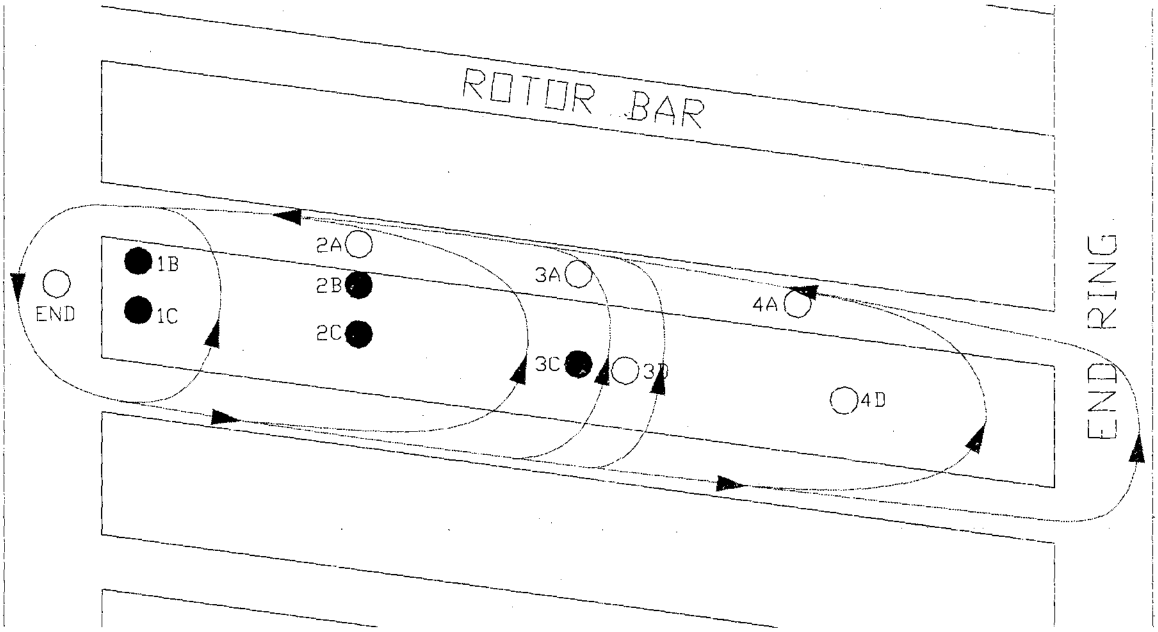

Figure 6.1.3: Inter-bar Current Distribution as Determined From Experiments

Based on the rate-of-rise of temperature during acceleration obtained at various locations around the rotor iron, a general thermal distribution during start-up is shown in Figure 6.1.4. The fastest temperature rise at start-up occurs in the center of the rotor iron at the mid-point between adjacent rotor bars and the end-rings. This occurrence is primarily due to inter-bar currents. The rotor iron close to both the rotor bars and the end-rings experienced a moderate increase in temperature most likely resulting from the heat from the bar and end-ring currents. The rotor iron at thermocouple 2C and 4D had the slowest rate-of-rise of temperature during start-up.

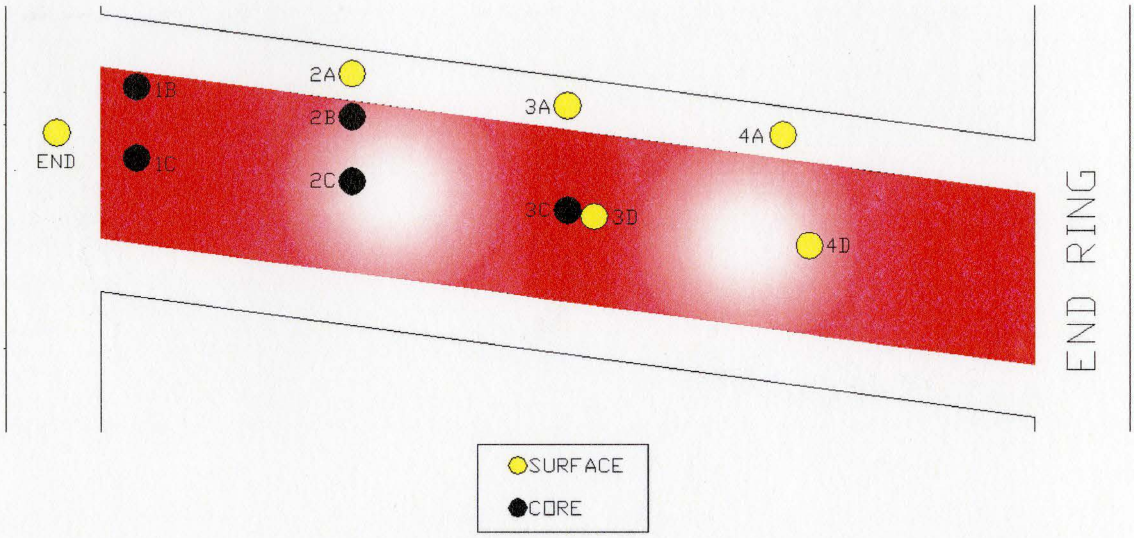

Figure 6.1.4: Rotor Iron Thermal Distribution Based on Experimental Rate-of-Rise

The thermal distribution in Figure 6.1.4 is only representative of the initial heating effects of inter-bar currents acting in isolation. The results in Figure 6.1.3 and Figure 6.1.4 indicate that the inter-bar current distribution is not uniform across the length of the rotor bar. Additionally, the experimental results indicate that the thermal response is dependent on the location relative to the rotor bars and the end-rings, but relatively independent with respect to the rotor surface.

6.2 Analysis of Direct Measurement Test Results

The results obtained by the acquisition system for the direct measurement tests yielded signals composed of three frequencies. Since the individual components varied significantly in frequency, three specific tests were performed at different acquisition rates to capture the individual components. The results of the search coil test are summarized in Table 6.3 along with the derived causes of each component.

Component	**Frequency (Hz)**	**Rate (samples/s)**	**Cause**
Low-Frequency	0.2565	100	Low frequency induced voltage generated by stator slip relative to the supply frequency. Determined primarily by the mechanical slip, and likely proportional to the motor's load
Mid-Frequency	14.8872	2,000	Fundamental induced voltage in the rotor bars resulting from the primary source voltage. A function of both the primary supply frequency and the number of pole pitches of the stator windings.
High-Frequency	718.60	10,000	High frequency component caused by stator slots passing over the rotor at rated speed. A function of the stator speed and the number of stator slots

Table 6.3: Search Coil Frequency Component Summary

6.2.1 Frequency Analysis

The resultant waveforms obtained from the three direct measurement tests were composed of three overlaid frequency components. Although the instruments were installed to measure the frequency of inter-bar currents indirectly by utilizing their proportional relationship to the resulting flux in the rotor, it is likely that all three frequency components are generated by physical or geometric phenomenon rather than inter-bar currents. In particular, the geometry and placement of the search coil windings relative to the air gap and the size of the search coil loops have the most significant impact on the effectiveness of the instruments at measuring inter-bar currents. Each of the frequency components will be presented with a postulate of their source in the following sections.

Low-Frequency Component

The 0.2565hz modulating frequency is due to the slip of the stator relative to the stationary rotor. As the stator slips relative to the rotor, a fixed point on the rotor experiences a sinusoidal variation in observed power with a frequency related to the relative slip speed. Working backwards from the low-frequency component, the required slip to generate this frequency can be calculated as:

$$\text{Slip} = 0.2565\frac{cycles}{s}\cdot 60\frac{s}{m} = 15.12rpm \tag{6.2}$$

Mid-frequency Component

Based on the supply frequency and the number of poles of the stator, the 14.887hz mid-frequency component is a result of the fundamental frequency of the supply power. The frequency of the rotating electromagnetic field observed by the rotor is:

$$f_{mid} = \frac{f \cdot 2}{8} = \frac{60hz \cdot 2}{8 pole - pitches} = 15hz \qquad (6.3)$$

High-frequency Component

The high-frequency 718.60hz component is a result of the stator slots passing over the search coils at rated speed, closer to the top leg of the search coil winding than the bottom leg. The search coil is physically wound over the surface of the rotor, down through one end-ring, back through the rotor iron, and up to through the other end-ring. The result is that one side of the search coil passes close to the stator through the air gap, while the opposite side passes through the rotor iron approximately 20mm from the air gap. The effects of the stator slots on the search coil will be stronger at the air gap than 20mm into the rotor iron, generating a net voltage in the search coil proportional to the speed of the motor and the number of stator slots. Analytically, the frequency generated by the stator slots is calculated as:

$$f_{high} = (speed) \cdot (\#ofslots) = \frac{\left(\frac{120 \cdot 60}{8} rpm\right) \cdot 48}{60 s/m} = 720hz \qquad (6.4)$$

Chapter 7

Conclusions

Many authors studying inter-bar currents are focusing on theoretical and mathematical modeling of inter-bar currents, with little attention to direct experimental data. The intention of this thesis was to pioneer practical experimentation related to the presence, distribution, magnitude and effects of inter-bar currents on the rotor of an induction machine. To accomplish this, an induction motor was instrumented with both thermocouples and custom current transducers to gather temperature and frequency component data related to inter-bar currents. While acquiring data directly using the search coils, and indirectly using thermocouples, the performance of several measuring instruments were also tested.

The search coils were wound to measure the main rotating field flux, and were effectively used to find the main frequency components of the flux as experienced by the rotor. Regardless of the materials used for the search coils, the outputs remained consistent, reflective of the fact that the main field flux simply generated a voltage across the coils which were not used to provide current to a load. Based on the direct measurement results, the search coil principle could be extended to directly measure the inter-bar currents with a slight change in winding geometry.

To gather temperature data, three different types of instruments were trialed: J-type thermocouples, T-type thermocouples and RTD's. The J-type thermocouples were found to be highly sensitive to the main stator field, which induced excessive noise on the instrument's output. Conversely, the T-type thermocouples were almost immune to induced noise from the stator field, and returned stable, repeatable results on the temperature rise in the rotor. Finally, the RTD's also performed comparably to the T-type thermocouples, but were significantly larger in size.

Based on the instantaneous rate-of-rise of temperature experimentally determined at various locations around the rotor iron, the expected inter-bar current distribution along the length of the rotor bars was proposed for the initial moments after the excitation was applied to the motor. The experimental results indicate that the rate-of-rise of temperature in the iron core was highly dependent on the location relative to the rotor bars and the end-rings, but not overly dependent on the location radially to the surface. The independence on location radially from the surface is likely due to the fact that the rotor was stationary, reducing many cooling effects. From the various experimental rates-of-rise measured around the rotor iron, non-uniform current and thermal distributions were presented along the length of the rotor bars. Finally, under the assumption that the heat generated in the iron core was due to inter-bar current in isolation during the first few seconds of motor excitation, the initial rate-of-rise of temperature was used to mathematically calculate an average value for the inter-bar currents necessary to generate the measured temperature rise.

7.1 Special Considerations with Thermal Tests

The variation in the rate-of-rise of temperature in different thermocouples is potentially due to poor thermal contact of the instruments to the rotor iron. The thermocouples were affixed to the rotor iron using a special thermal epoxy that required temperatures in excess of 400°F for several hours to cure. During the curing process both the rotor and the thermocouple leads began to expand because of the heat, potentially altering the contact junction. Since the instruments were in blind holes it was impossible to verify that good thermal conductivity was achieved without destroying the contact region.

Additionally, curve fitting was difficult because of the noise present in the data sampling. Even a slight change of individual data points in the raw data has a significant effect on the best-fit polynomials fit to the data, which is amplified in the rate-of-rise calculations presented with the derivatives. Consequently, direct hardware filtering of the thermocouple inputs instead of software filtering would more adequately isolate the true temperature readings.

7.2 Recommended Future Work

The orientation of the search coils relative to the expected path of the inter-bar currents was not suitable for directly measuring inter-bar currents. An ideal current transducer couples the desired conductor parallel to the current path, making use of a ferromagnetic material to form a simple transformer, similar to Figure 7.1 below.

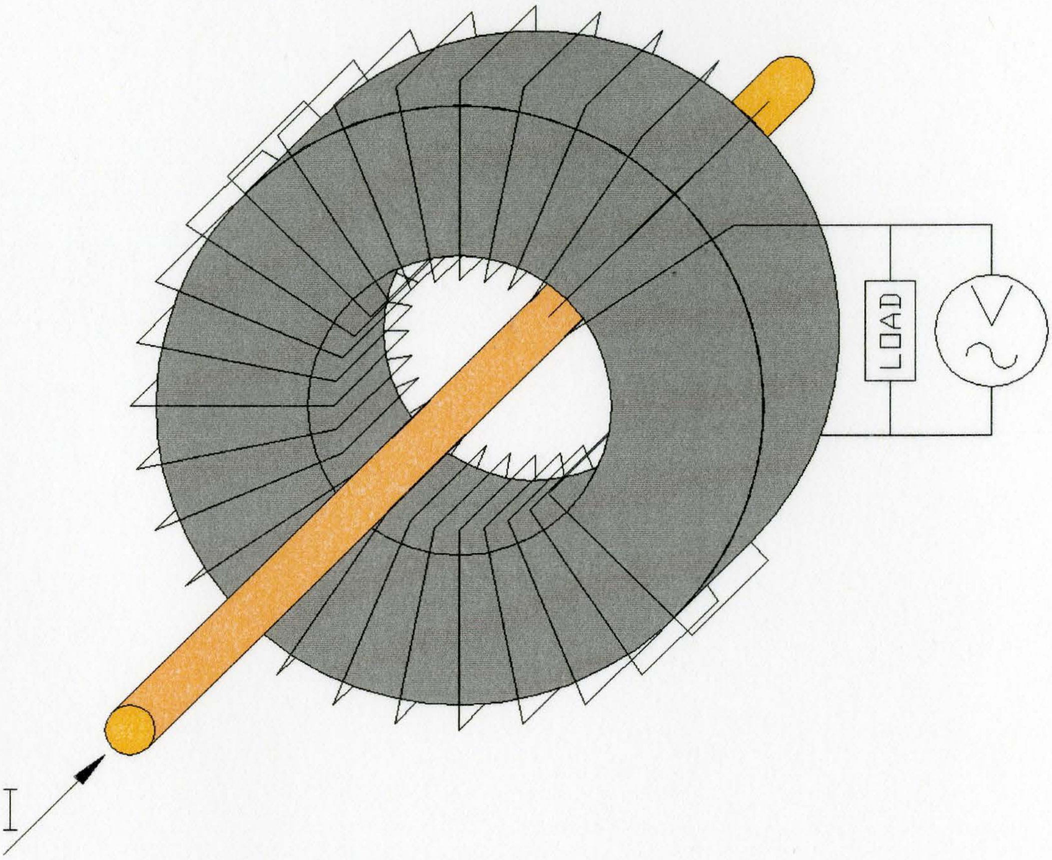

Figure 7.1: Ideal Search Coil Configuration

Orienting the search coil windings in a configuration ideal for measuring the inter-bar currents directly was problematic because a return path for the coil loops below the rotor iron could not be facilitated. Consequently, the search coils were wound in such a way as to measure the induced voltage due to the main field rotating flux. A review of the current and historical literature indicates that little experimental research exists relative to the direct measurement of the main field rotating flux, so the experimental results are still relevant to the academic community. The winding method used in the experiments to measure the main field flux, as well as the winding method suggested for direct current measurement are shown in Figure 7.2.

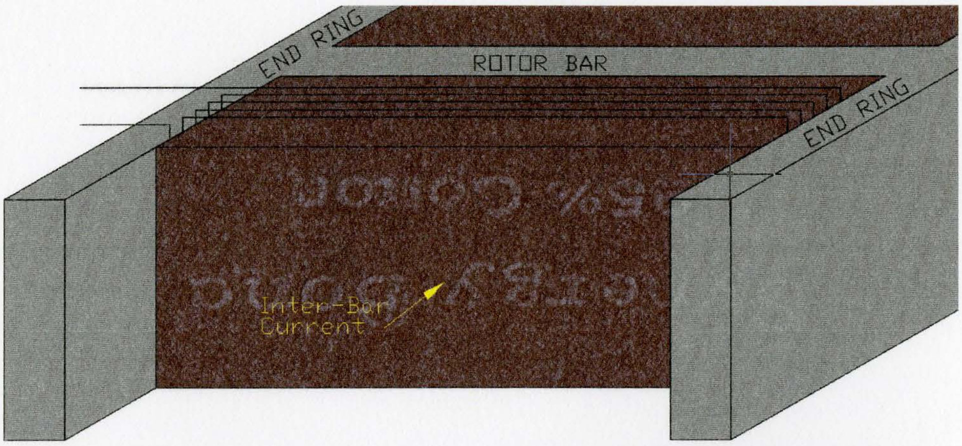

Experimental Winding: Main Field Rotating Flux Measurement

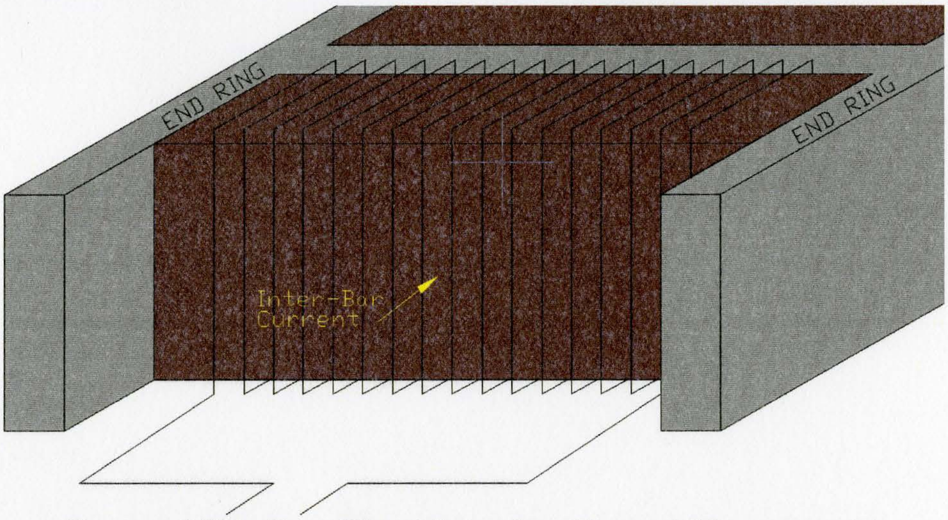

Proposed Winding: Direct Inter-bar Current Measurement

Figure 7.2: Experimental Winding and Correct Winding method for search coils

The thermal tests yielded good preliminary results concerning the presence, distribution, magnitude and effects of inter-bar currents on the rotor of an induction machine. The tests related the temperature rise at various points on the rotor directly to inter-bar currents under no-load conditions. However, the sensitivity of the mathematical equations relating temperature rise to the inter-bar currents warrants systematic care in the placement of the thermal instrumentation on the rotor. In particular, improvement on both the precise location of the thermocouples relative to the end-rings and rotor bars, and the adhesion of the thermocouples to the rotor with the thermal epoxy is required.

Additionally, the initial rate-of-rise of temperature, critical in determining the inter-bar currents, was derived using both least-squares polynomials and filtering of the raw data. Ideally, an improved data acquisition system with integrated hardware filtering would help reduce the sampling noise associated with the thermal inputs and aid in more accurate least-squares modeling. An integrated hardware filter calibrated specifically for both the T-type thermocouples used in the experiment and for the expected time response of the system would produce more stable analog temperature data at a minimal cost.

The results of the direct measurement tests could be improved to better reflect inter-bar currents by changing the geometry and location of the search coil windings. This would require additional modifications to the rotor to facilitate placement of the winding loops around the rotor iron. Specifically, new holes would have to be drilled radially into the rotor, as well as circumferentially around the rotor at a depth of approximately two centimeters. The circumferential hole is literally impossible to drill after the motor has been manufactured without damaging the rotor structure, so this type of clearance would have to be provisioned at the design stage. Additional channels would also be required along the surface of the rotor because of the minimal clearance between the stator and rotor.

Finally, both the thermal and direct measurement tests were performed on the motor under no-load conditions to reduce physical risk associated with loading the motor. The custom inverted induction machine was not designed to experience any unbalanced load such as from a timing belt or single-point brake which would tend to overstress the bearings and support structure. The motor requires significant mechanical modification before any appropriate torsional load could be applied, such as a gearbox or flywheel. However, performing both the thermal and direct measurement tests under load would give much better insight into inter-bar currents.

References

[1] Glew, C.N. (1998). "Stray load losses in induction motors: A challenge to academia". *Power Engineering Journal*: 12 [1]: 27-32.

[2] Jimoh, A.A. & V. Munhurrun. (1999). "A thermal model for the study of stray load losses in induction motors". *IEEE (Africon)*, 2 [Sept.-Oct.]: 881-886.

[3] Veinott, C.G. (1959). Theory and Design of Small Induction Motors. New York, United States of America: McGraw-Hill Book Company Inc.

[4] Bradley, K.J., Ferrah, A., Magill, R., Clare, J.C., Wheeler, P. & P. Sewell. (1999). "Improvements to precision measurement of stray load loss by calorimeter". *Ninth International Conference on Electrical Machines and Drives,* [468]: 189-193.

[5] Dorrell, D.G., Miller, T.J.E. & C.B. Rasmussen. (2003). "Inter-bar currents in induction machines". *IEEE Transactions on Industry Applications*, 39 [3]: 677-684.

[6] Bousbaine, A., Low, W.F. & M. McCormick. (1996). "Novel approach to the measurement of iron and stray load losses in induction motors". *IEE Proc.-Electr. Power Appl.,* 143, [1]: 78-86

[7] Findlay, R.D. & H.A. Briggs. (1973). "Open circuit tooth ripple eddy current loss in smooth laminated poles". *IEEE PES Summer Meeting.*

[8] Christophides, N. (1965). "Origins of load losses in induction motors with cast aluminium rotors". *IEE Procedings – Electric Power Applications*, 112 [12]: 2317-2332.

[9] Yamazaki, K. & Y. Haruishi. (2003). "Stray load loss analysis of induction motor – comparison of measurement due to IEE standard 112 and direct calculation by finite element method". *IEEE,* 1 [1-4]: 285-290.

[10] Carlson, R. (2003). "Inter-bar currents in the rotor of large three-phase cage induction motors: analysis and detection". *Symposium on Diagnostics for Electric Machines, Power Electronics and Drives*: 242-246

[11] Jimoh, A.A. (2000). "Thermal effects of stray load losses in induction machines". *IEEE Transactions on Industry Applications*, 36 [4]: 1085-1093.

[12] Williamson, S., Poh, C.Y. & A.C. Smith. (2003) "Estimation of the inter-bar resistance of a cast cage rotor", 40 [2]: 558-564

[13] Odok, A.M. (1958). "Stray-load losses and stray torques in induction machines". *Trans. Amer. Inst. Electr. Engnrs,* 77 [Pt. II]: 43-55

[14] Subba Rao, V. & O.I. Butler. (1969). "Stray losses in polyphase cage induction motors with particular reference to the condition of imperfect rotor bar-iron insulation". *IEE Procedings – Electric Power Applications*, 116 [5]: 737-751.

[15] Schwarz, K.K. (1964). "Survey of basic stray losses in squirrel-cage induction motors", Proc. IEE [111]: 1565-1574.

[16] Morgan, T.H., Brown, T.E., & A.T. Shcumer. (1939). "Reverse-rotation test for the determination of stray-load loss in induction machines". *Trans. AIEE* [58]: 319-324.

[17] Chalmers, B.J. & A.C. Williamson. (1963). "Stray losses in squirrel-cage induction motors". *IEE Proceedings,* 110 [10]: 1773-1778.

[18] Jimoh, A.A. (1999). "Thermal effects of stray load losses in induction machines". *Industry Applications Conference - IEEE*: 1 [3-7]: 481-488.

[19] Glew, N. (1999). Stray Losses in Induction Motors – If only I knew where to Start!. *IEE*. London: Savoy Place.

[20] Derrah, S., Findlay, R.D. & R. Ong. (2001). "A statistical procedure for analyzing stray losses in induction motors from measurement". *Instrmentation and Measurement Technology Conference - IEEE*: 3 [21-23 May]: 1801-1806.

[21] Williamson, S. & A.C. Smith. (2002). "Equivalent circuits for cage induction motors with inter-bar currents". *IEE Proc.-Electric Power Application,* 149 [3]: 173-183.

[22] Carlson, R., da Silva, C.A., Sadowski, N., Lefevre, Y. & M. Lajoi-Mazenc. (2001). "An analysis of inter-bar currents on a polyphase cage induction motor", *IEEE Transactions*, 39 [6]: 1674-1680.

[23] Nishizawa, H., Itomi, K., Hibino, S. & F. Ishibashi. (1997). "Study on reliable reduction of stray load losses in three-phase induction motor for mass production". *IEEE Transactions on Energy Conversion,* 2 [3]: Set.

[24] Behdashti, A. & M. Poloujadoff. (1979). "A new method for the study of inter-bar currents in polyphase squirrel-cage induction motors". *IEEE transactions on Power Apparatus and Systems",* PAS-98 [3]: 902-911

[25] Ware, D.H. (1945). "Measurement of stray load losses in induction motors". *Trans. AIEE,* 64: 194-196.

[26] Cao, W., Bradley, K.J. & J. Allen. (2004) "Evaluation of stray load loss in induction motors: consequents upon repair and rewinding". *IEEE, 3: 1381-1286.*

[27] Jimoh, A.A. (1986). Stray Load Losses in Induction Machines. Hamilton, Ontario: McMaster University

[28] Ho, S.L., Fu,W.N. & H.C. Wong. (1998). "Estimation of stray losses of skewed rotor induction motors using coupled 2-D and 3-D time stepping finite element methods". *IEEE Transaction on Magnetics*, 34 [5]: 3102-3105.

[29] Carlson, R., da Silva, C.A., Sadowski, N., Lefevre, Y. & M. Lajoi-Mazenc. (2003). "Analysis of the effect of inter-bar currents on the performance of polyphase cage-induction motor", *Industry Applications, IEEE Transactions,* 39 [6]: 1674-1680.

[30] Gersh, D., Smith, A.C. & A. Samuelson. (1997). "Measurement of inter-bar resistance in cage rotors". *IEEE – Conference Publication No. 444,* 1-3 September: 253-257.

[31] McClay, C.I. & S. Williamson. (1997). "The influence of rotor skew on cage motor losses". *IEE*, Conference Publication No. 444.

[32] Heller, B. & A.L. Joki. (1971). "Losses in squirrel-cage motors due to rotor skew". *IEEE Transactions on Power Apparatus and Systems"*, PAS-90 [2]: 556-563.

[33] Jimoh, A.A., Findlay, R.D. & M. Poloujadoff. (1985). "Stray losses in induction machines: Part I. definition, origin and measurement", *IEEE Transactions on Power Apparatus and Systems,* PAS-104 [6]: 1500-1505.

[34] Jimoh, A.A., Findlay, R.D. & M. Poloujadoff. (1985). "Stray losses in induction machines: Part II. calculation and reduction", *IEEE Transactions on Power Apparatus and Systems,* PAS-104 [6]: 1506-1512.

[35] Matsuse, K., Hayashida, T., Miki, I., Kubota, H. & T. Yoshida. (1994). "Effects of crosspath resistance between adjacent rotor bars on performance of inverter-fed high-speed induction motor". *IEEE Transactons on Industry Applications,* 30 [3]: 621-627.

[36] Spooner, E. (1982). "Stray loss in solid-rotor induction machines". *IEE Proceedings,* 129 Pt.B, [4]:
181-189

[37] Lindsay, J.F. & T.H. Barton. (1972). "A modern approach to induction machine parameter identification". *IEEE transactions on Power Apparatus and Systems",* PAS-91 [4]: 1493-1500.

[38] Almeida, A.T., Ferreira, F.J.T.E., Busch, J.F. & P. Angers. (2002). "Comparative analysis of IEEE 112-B and IEC 34-2 efficiency testing standards using stray load losses in low-voltage three-phase cage induction motors". *IEEE Transactions on Industry Applications,* 38 [2]: 608-614.

[39] Meshgin-Kelk, H., Milimonfared, J., & H.A. Toliyat. (2004). "Interbar currents and axial fluxes in healthy and faulty induction Motors". *IEEE Transactions on Industry Applications,* 40 [1]: 128-134.

[40] Bogliettie, A., Lazzari, A.C. & M. Pastorelli. (2003). "International standards for the induction motor efficiency evaluation: a critical analysis of stray-load loss determination". *IEEE Transactions on Industry Applications,* V [i]: 841-848.

Appendix A

Motor CAD Drawings

Appendix A contains various CAD drawings of the custom inverted three-phase induction motor, manufactured by Westinghouse. The CAD drawings included in this appendix are reproductions of hard copies received with the motor. As such, the drawings are not complete, but include all data received with the documentation. Acquiring any additional mechanical or electrical information has proven impossible as Westinghouse is no longer designing or manufacturing electric motors, and does not keep records of previous builds.

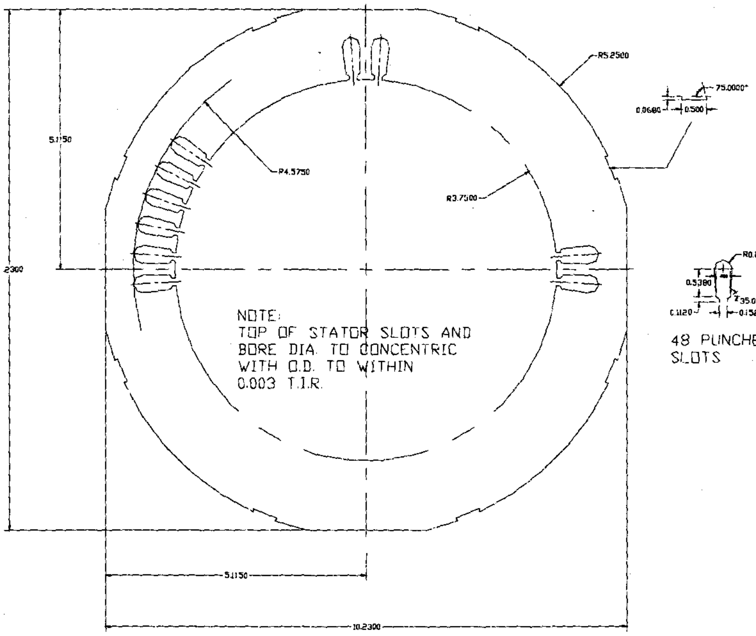

Figure AA.1: Stator Slot Configuration

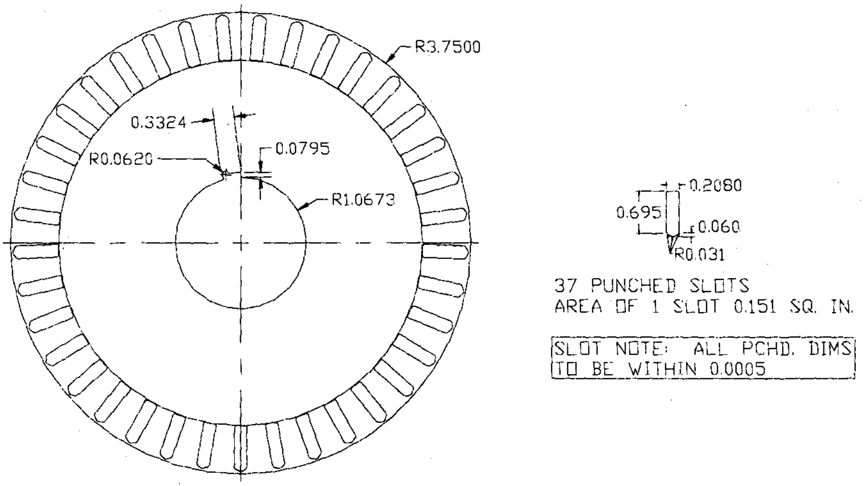

Figure AA.2: Rotor Bar Distribution

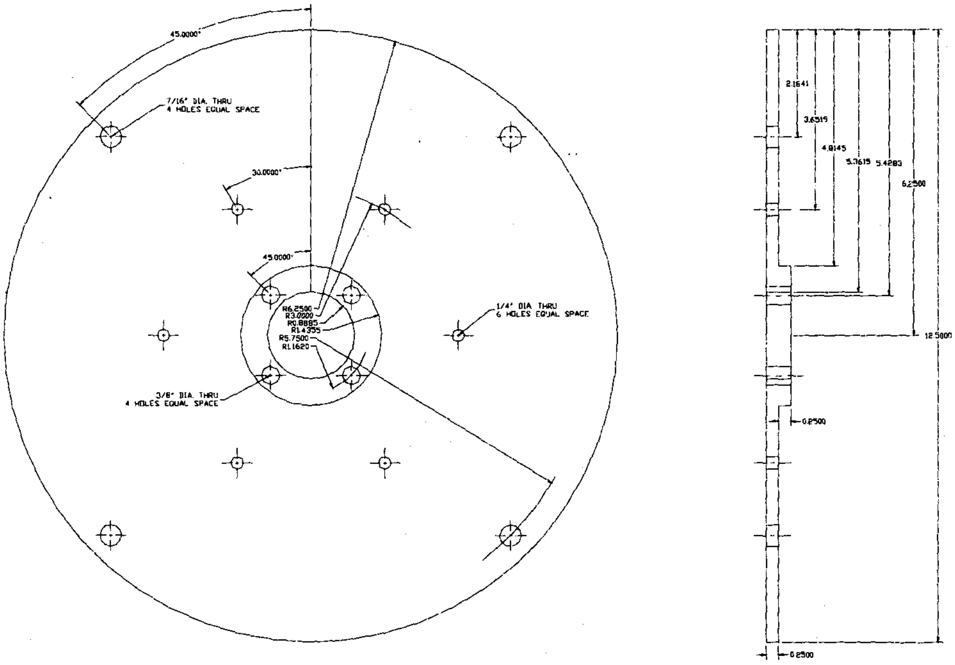

Figure AA.3: Slip Ring Adapter Plate

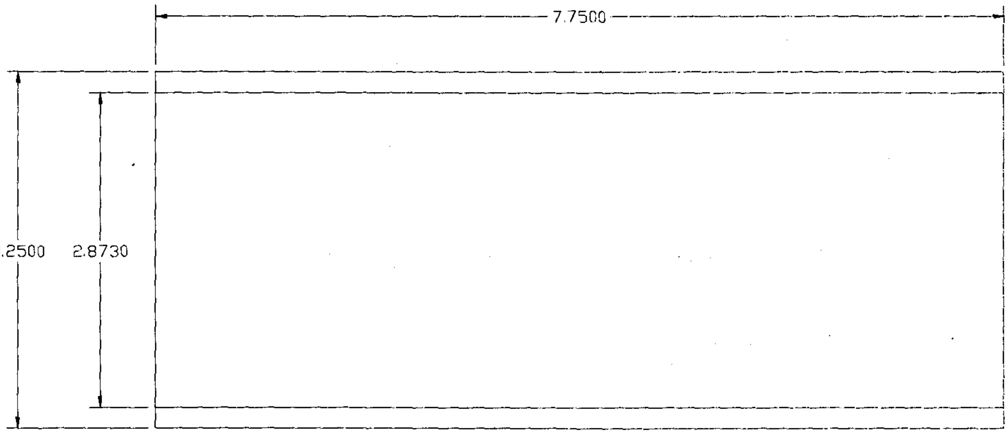

Figure AA.4: Slip Ring Collector Sleeve (mounted on Adapter Plate)

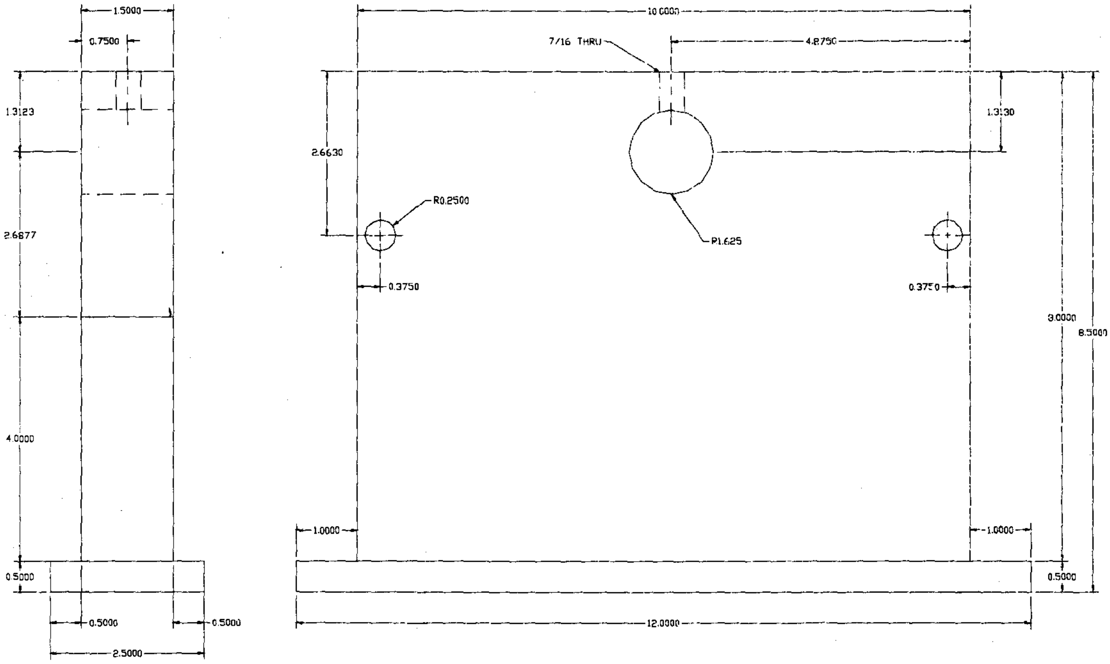

Figure AA.5: Inner Shaft Support (Closest to Slip Rings)

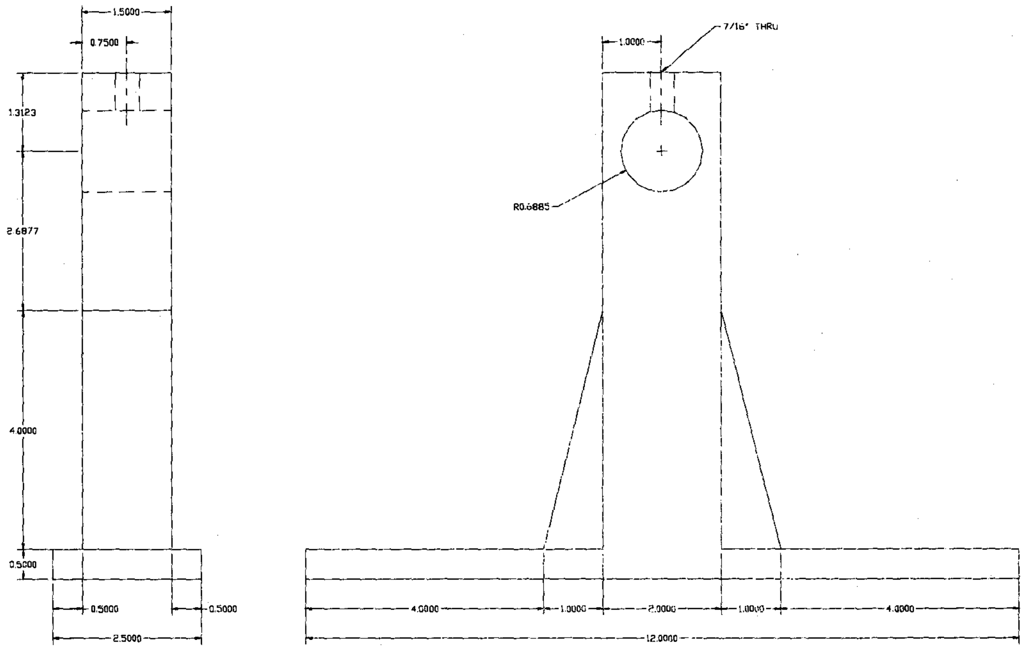

Figure AA.6: Outer Shaft Support

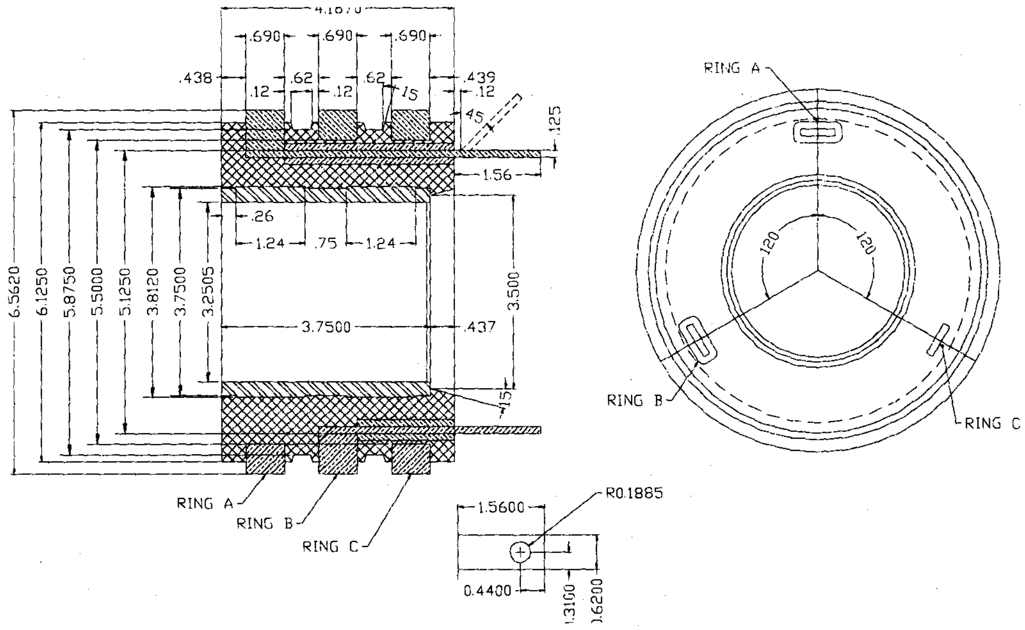

Figure AA.7: Input Collector (Slip Rings, mounted on Collector Shaft)

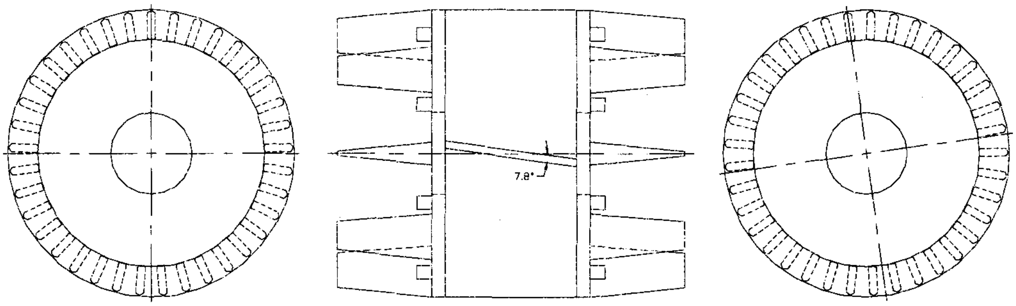

Figure AA.8: Rotor bar skew

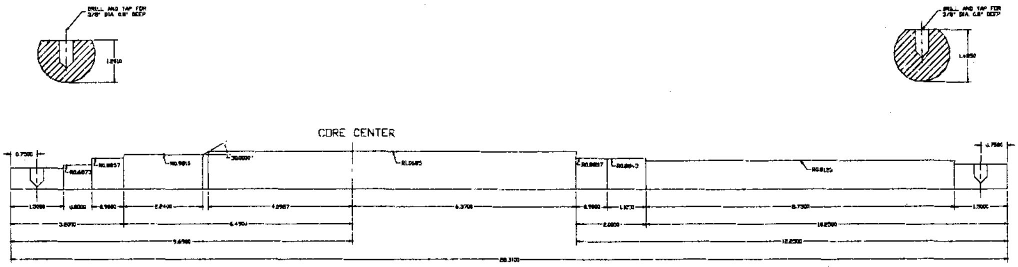

Figure AA.9: Motor Shaft

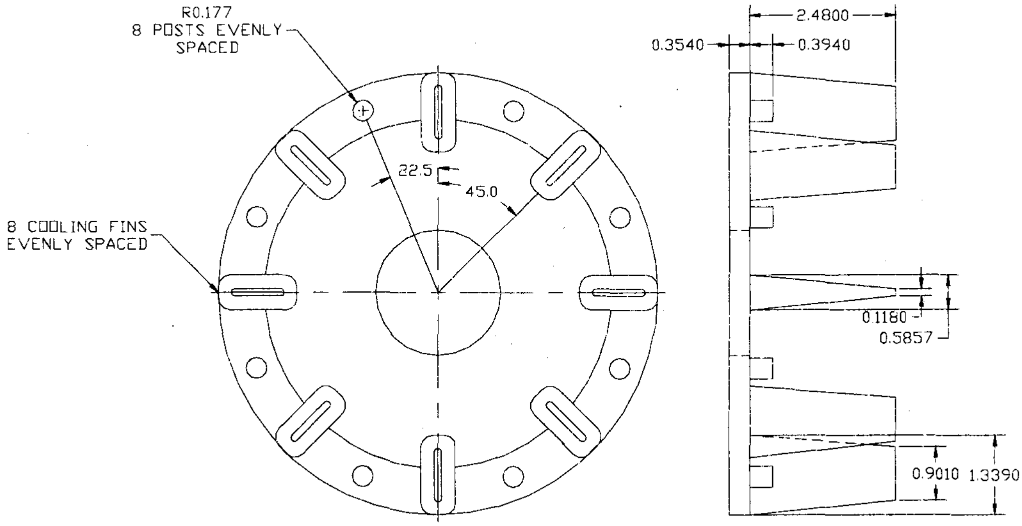

Figure AA.10: Rotor End Plates

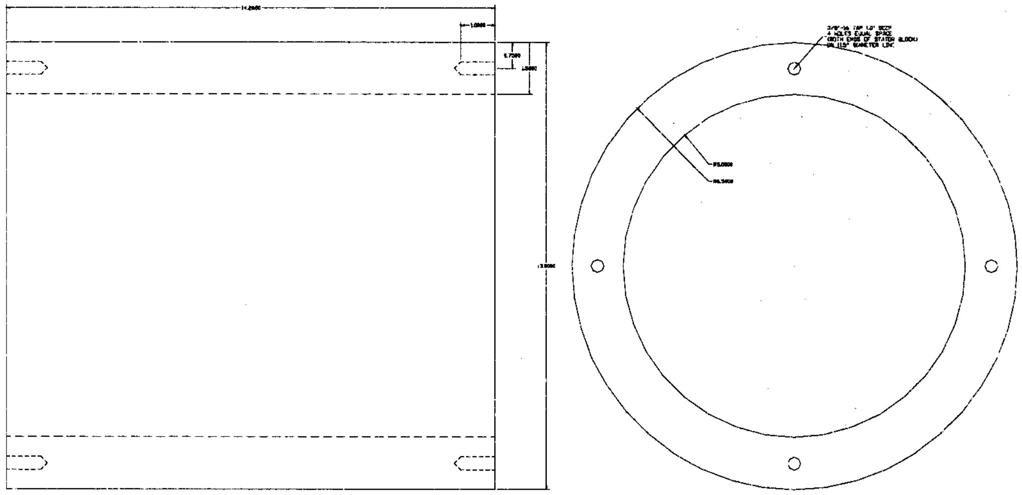

Figure AA.11: Stator Support Cylinder

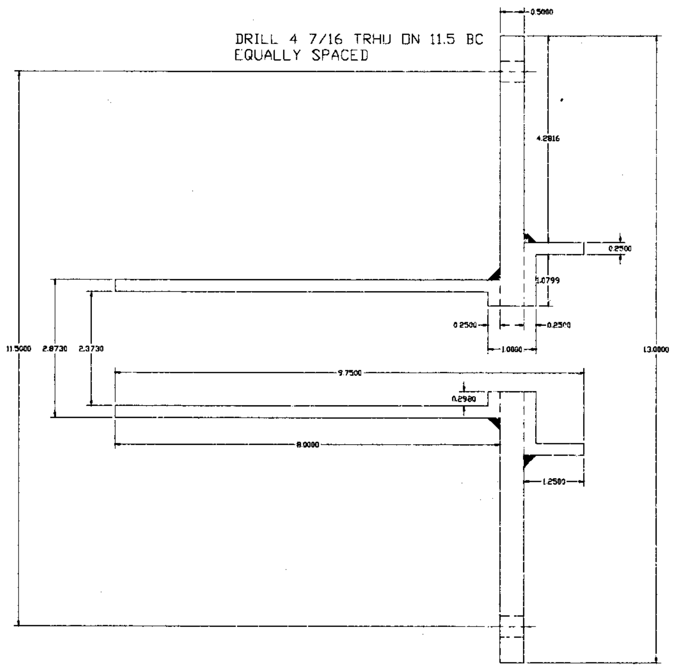

Figure AA.12: Stator Inner Mounting Plate (Closest to Slip Rings)

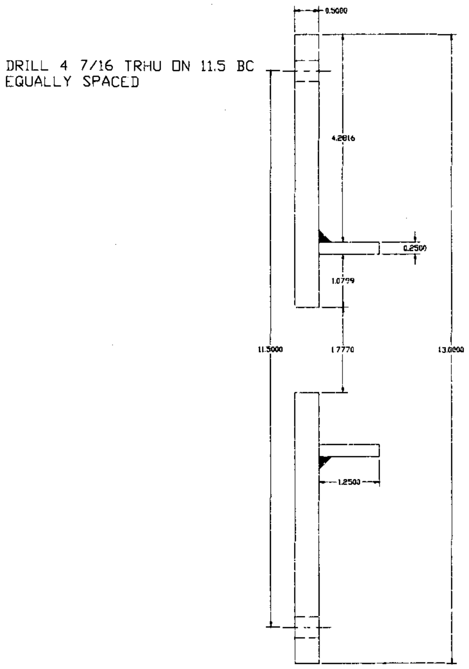

Figure AA.13: Stator Outer Mounting Plate

Appendix B

Supplementary Data

Coef.	TC 3C	TC 1B	TC 3D	TC 2A	TC 2B	TC 4A	TC 3A	TC END	TC 1C	TC 4D	TC 2C
C_{20}	-1.35 E-41	-3.09 E-42	1.40 E-42	2.18 E-42	-3.89 E-42	2.08 E-43	-1.05 E-41	-5.58 E-42	-2.12 E-42	-6.59 E-42	-7.60 E-42
C_{19}	5.84 E-38	1.38 E-38	-5.62 E-39	-8.42 E-39	1.73 E-38	-1.49 E-39	4.45 E-38	2.44 E-38	8.61 E-39	2.84 E-38	3.22 E-38
C_{18}	-1.18 E-34	-2.87 E-35	1.03 E-35	1.48 E-35	-3.58 E-35	4.22 E-36	-8.83 E-35	-4.99 E-35	-1.62 E-35	-5.71 E-35	-6.33 E-35
C_{17}	1.47 E-31	3.71 E-32	-1.15 E-32	-1.56 E-32	4.57 E-32	-6.82 E-33	1.08 E-31	6.31 E-32	1.88 E-32	7.06 E-32	7.68 E-32
C_{16}	-1.28 E-28	-3.32 E-29	8.68 E-30	1.09 E-29	-4.03 E-29	7.25 E-30	-9.19 E-29	-5.53 E-29	-1.51 E-29	-6.03 E-29	-6.43 E-29
C_{15}	8.17 E-26	2.20 E-26	-4.65 E-27	-5.16 E-27	2.61 E-26	-5.48 E-27	5.74 E-26	3.58 E-26	8.82 E-27	3.78 E-26	3.94 E-26
C_{14}	-3.98 E-23	-1.11 E-23	1.80 E-24	1.61 E-24	-1.28 E-23	3.07 E-24	-2.73 E-23	-1.76 E-23	-3.91 E-24	-1.80 E-23	-1.83 E-23
C_{13}	1.51 E-20	4.37 E-21	-4.94 E-22	-2.51 E-22	4.89 E-21	-1.31 E-21	1.01 E-20	6.79 E-21	1.34 E-21	6.64 E-21	6.58 E-21
C_{12}	-4.55 E-18	-1.36 E-18	8.80 E-20	-3.75 E-20	-1.47 E-18	4.35 E-19	-2.96 E-18	-2.07 E-18	-3.62 E-19	-1.93 E-18	-1.85 E-18
C_{11}	1.09 E-15	3.37 E-16	-5.79 E-18	3.71 E-17	3.52 E-16	-1.13 E-16	6.91 E-16	5.05 E-16	7.71 E-17	4.43 E-16	4.13 E-16
C_{10}	-2.09 E-13	-6.69 E-14	-1.97 E-15	-1.27 E-14	-6.72 E-14	2.31 E-14	-1.29 E-13	-9.85 E-14	-1.31 E-14	-8.08 E-14	-7.27 E-14
C_9	3.20 E-11	1.06 E-11	7.97 E-13	2.84 E-12	1.02 E-11	-3.71 E-12	1.92 E-11	1.54 E-11	1.78 E-12	1.17 E-11	1.01 E-11
C_8	-3.90 E-09	-1.34 E-09	-1.60 E-10	-4.59 E-10	-1.24 E-09	4.68 E-10	-2.28 E-09	-1.93 E-09	-1.94 E-10	-1.34 E-09	-1.10 E-09
C_7	3.76 E-07	1.33 E-07	2.18 E-08	5.55 E-08	1.18 E-07	-4.59 E-08	2.14 E-07	1.91 E-07	1.69 E-08	1.21 E-07	9.27 E-08
C_6	-2.83 E-05	-1.03 E-05	-2.14 E-06	-5.05 E-06	-8.84 E-06	3.45 E-06	-1.58 E-05	-1.48 E-05	-1.19 E-06	-8.38 E-06	-5.97 E-06
C_5	1.63 E-03	6.13 E-04	1.53 E-04	3.43 E-04	5.09 E-04	-1.94 E-04	8.91 E-04	8.86 E-04	6.74 E-05	4.43 E-04	2.87 E-04
C_4	-7.01 E-02	-2.72 E-02	-7.91 E-03	-1.70 E-02	-2.20 E-02	7.98 E-03	-3.78 E-02	-3.96 E-02	-3.03 E-03	-1.74 E-02	-9.94 E-03
C_2	2.16 E+00	8.62 E-01	2.87 E-01	5.99 E-01	6.91 E-01	-2.28 E-01	1.15 E+00	1.27 E+00	1.04 E-01	4.90 E-01	2.37 E-01
C_2	-4.50 E+01	-1.84 E+01	-6.89 E+00	-1.40 E+01	-1.48 E+01	4.20 E+00	-2.38 E+01	-2.77 E+01	-2.54 E+00	-9.31 E+00	-3.64 E+00
C_1	5.61 E+02	2.36 E+02	9.78 E+01	1.93 E+02	1.92 E+02	-4.33 E+01	2.96 E+02	3.60 E+02	3.87 E+01	1.07 E+02	3.21 E+01
C_0	-3.12 E+03	-1.34 E+03	-5.95 E+02	-1.16 E+03	-1.11 E+03	2.01 E+02	-1.64 E+03	-2.08 E+03	-2.46 E+02	-5.47 E+02	-1.04 E+02

Table AB.1: Steady State Test: Least-Squares Polynomial Coefficients

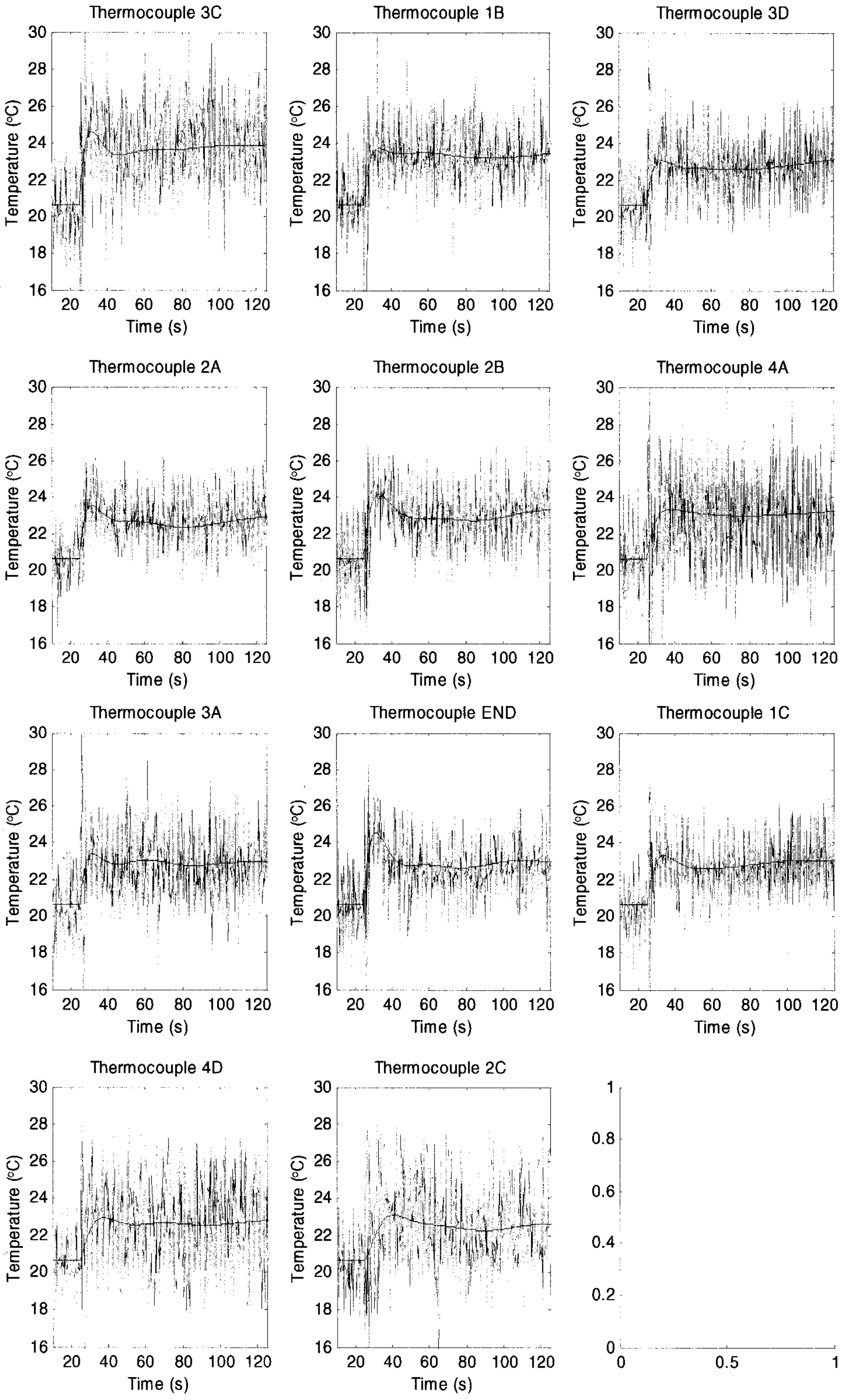

Figure AB.1: Steady-State Test: Log Data Set Polyfit Curves Over Raw Data Sets

Coef.	TC 3C	TC 1B	TC 3D	TC 2A	TC 2B	TC 4A	TC 3A	TC END	TC 1C	TC 4D	TC 2C
C_{18}	-1.57 E-37	-1.18 E-37	-7.79 E-38	-1.01 E-37	6.26 E-38	3.03 E-38	-6.90 E-39	-5.96 E-38	-7.49 E-39	1.23 E-37	1.49 E-37
C_{17}	6.09 E-34	4.50 E-34	3.00 E-34	3.90 E-34	-2.36 E-34	-1.06 E-34	3.82 E-35	2.47 E-34	3.28 E-35	-4.70 E-34	-5.68 E-34
C_{16}	-1.09 E-30	-7.93 E-31	-5.32 E-31	-6.99 E-31	4.10 E-31	1.68 E-31	-9.03 E-32	-4.73 E-31	-6.60 E-32	8.27 E-31	1.00 E-30
C_{15}	1.20 E-27	8.58 E-28	5.80 E-28	7.68 E-28	-4.35 E-28	-1.61 E-28	1.25 E-28	5.54 E-28	8.09 E-29	-8.90 E-28	-1.08 E-27
C_{14}	-9.04 E-25	-6.37 E-25	-4.33 E-25	-5.80 E-25	3.14 E-25	1.04 E-25	-1.15 E-25	-4.45 E-25	-6.78 E-26	6.56 E-25	8.03 E-25
C_{13}	4.97 E-22	3.44 E-22	2.36 E-22	3.19 E-22	-1.63 E-22	-4.68 E-23	7.48 E-23	2.60 E-22	4.12 E-23	-3.50 E-22	-4.32 E-22
C_{12}	-2.06 E-19	-1.40 E-19	-9.65 E-20	-1.32 E-19	6.34 E-20	1.51 E-20	-3.61 E-20	-1.14 E-19	-1.88 E-20	1.40 E-19	1.75 E-19
C_{11}	6.55 E-17	4.38 E-17	3.04 E-17	4.21 E-17	-1.86 E-17	-3.48 E-18	1.32 E-17	3.84 E-17	6.57 E-18	-4.31 E-17	-5.41 E-17
C_{10}	-1.62 E-14	-1.06 E-14	-7.43 E-15	-1.04 E-14	4.15 E-15	5.31 E-16	-3.72 E-15	-1.00 E-14	-1.79 E-15	1.02 E-14	1.30 E-14
C_9	3.14 E-12	2.02 E-12	1.42 E-12	2.02 E-12	-7.06 E-13	-3.98 E-14	8.10 E-13	2.05 E-12	3.79 E-13	-1.88 E-12	-2.42 E-12
C_8	-4.75 E-10	-3.00 E-10	-2.13 E-10	-3.06 E-10	8.99 E-11	-3.35 E-12	-1.37 E-10	-3.25 E-10	-6.27 E-11	2.68 E-10	3.52 E-10
C_7	5.58 E-08	3.47 E-08	2.47 E-08	3.62 E-08	-8.36 E-09	1.47 E-09	1.78 E-08	4.01 E-08	8.07 E-09	-2.95 E-08	-3.95 E-08
C_6	-5.05 E-06	-3.09 E-06	-2.22 E-06	-3.29 E-06	5.33 E-07	-2.29 E-07	-1.77 E-06	-3.80 E-06	-8.00 E-07	2.47 E-06	3.39 E-06
C_5	3.46 E-04	2.09 E-04	1.51 E-04	2.27 E-04	-1.96 E-05	2.22 E-05	1.32 E-04	2.72 E-04	6.01 E-05	-1.55 E-04	-2.19 E-04
C_4	-1.75 E-02	-1.04 E-02	-7.61 E-03	-1.16 E-02	5.55 E-05	-1.45 E-03	-7.21 E-03	-1.43 E-02	-3.34 E-03	7.01 E-03	1.03 E-02
C_3	6.30 E-01	3.71 E-01	2.73 E-01	4.18 E-01	3.42 E-02	6.41 E-02	2.78 E-01	5.32 E-01	1.32 E-01	-2.21 E-01	-3.41 E-01
C_2	-1.51 E+01	-8.84 E+00	-6.55 E+00	-1.01 E+01	-1.74 E+00	-1.84 E+00	-7.06 E+00	-1.31 E+01	-3.49 E+00	4.49 E+00	7.41 E+00
C_1	2.14 E+02	1.25 E+02	9.35 E+01	1.44 E+02	3.81 E+01	3.08 E+01	1.06 E+02	1.91 E+02	5.46 E+01	-5.20 E+01	-9.36 E+01
C_0	-1.32 E+03	-7.68 E+02	-5.73 E+02	-8.89 E+02	-3.02 E+02	-2.06 E+02	-6.73 E+02	-1.21 E+03	-3.58 E+02	2.72 E+02	5.34 E+02

Table AB.2: Steady State Test: Least-Squares Logarithmic Polynomial Coefficients

	Thermocouple 1C			Thermocouple 2B			Thermocouple 2C			Thermocouple 3C			Thermocouple END		
Coef	Test 1	Start 2	Start 3	Start 1	Start 2	Start 3	Start 1	Start 2	Start 3	Start 1	Start 2	Start 3	Start 1	Start 2	Start 3
C_9	3.40 E-13	-9.45 E-14	-2.70 E-14	4.05 E-13	-3.30 E-14	-9.51 E-13	2.82 E-13	6.17 E-14	5.27 E-13	7.87 E-13	1.02 E-13	-5.05 E-13	4.84 E-13	-2.16 E-13	-1.28 E-14
C_8	-1.29 E-10	1.58 E-10	7.80 E-11	-1.66 E-10	5.05 E-11	2.67 E-09	-1.15 E-10	-1.08 E-10	-1.49 E-09	-3.11 E-10	-1.77 E-10	1.40 E-09	-1.96 E-10	3.34 E-10	2.17 E-11
C_7	2.13 E-08	-1.17 E-07	-1.00 E-07	2.96 E-08	-3.39 E-08	-3.33 E-06	2.00 E-08	8.29 E-08	1.87 E-06	5.31 E-08	1.35 E-07	-1.73 E-06	3.43 E-08	-2.29 E-07	-9.03 E-09
C_6	-1.98 E-06	5.03 E-05	7.47 E-05	-3.02 E-06	1.31 E-05	2.43 E-03	-1.95 E-06	-3.70 E-05	-1.37 E-03	-5.13 E-06	-6.02 E-05	1.25 E-03	-3.42 E-06	9.09 E-05	-6.87 E-06
C_5	1.16 E-04	-1.39 E-02	-3.58 E-02	1.93 E-04	-3.18 E-03	-1.13 E+00	1.17 E-04	1.05 E-02	6.45 E-01	3.08 E-04	1.71 E-02	-5.77 E-01	2.13 E-04	-2.31 E-02	9.63 E-03
C_4	-4.40 E-03	2.53 E+00	1.14 E+01	-7.99 E-03	5.04 E-01	3.53 E+02	-4.43 E-03	-1.99 E+00	-2.02 E+02	-1.19 E-02	-3.23 E+00	1.78 E+02	-8.62 E-03	3.88 E+00	-5.04 E+00
C_3	1.09 E-01	-3.08 E+02	-2.43 E+03	2.13 E-01	-5.16 E+01	-7.32 E+04	1.07 E-01	2.49 E+02	4.23 E+04	2.94 E-01	4.04 E+02	-3.64 E+04	2.25 E-01	-4.33 E+02	1.48 E+03
C_2	-1.73 E+00	2.39 E+04	3.31 E+05	-3.52 E+00	3.24 E+03	9.75 E+06	-1.58 E+00	-2.00 E+04	-5.67 E+06	-4.48 E+00	-3.24 E+04	4.80 E+06	-3.66 E+00	3.08 E+04	-2.56 E+05
C_1	1.56 E+01	-1.08 E+06	-2.63 E+07	3.23 E+01	-1.11 E+05	-7.57 E+08	1.34 E+01	9.31 E+05	4.44 E+08	3.80 E+01	1.51 E+06	-3.68 E+08	3.32 E+01	-1.27 E+06	2.46 E+07
C_0	-3.81 E+01	2.16 E+07	9.26 E+08	-9.98 E+01	1.48 E+06	2.61 E+10	-2.73 E+01	-1.92 E+07	-1.54 E+10	-1.12 E+02	-3.11 E+07	1.25 E+10	-1.02 E+02	2.29 E+07	-1.01 E+09

Table AB.3: Start-up test: Least-Squares Polynomial Coefficients

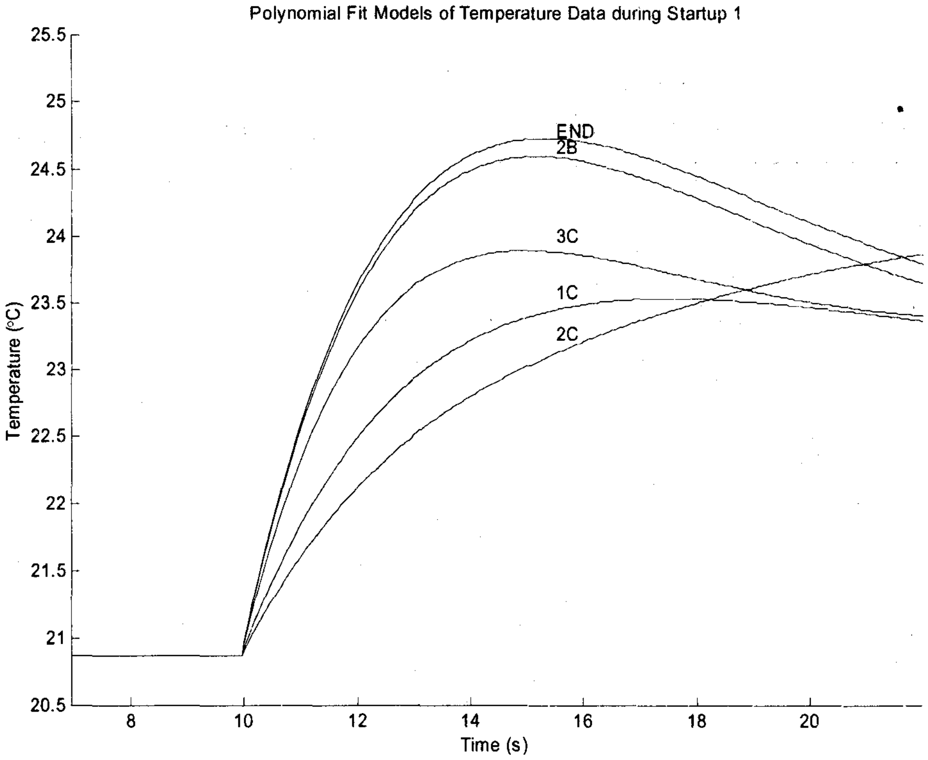

Figure AB.2a: Rate-of-Rise of Thermocouples During Startup: Start-up Test

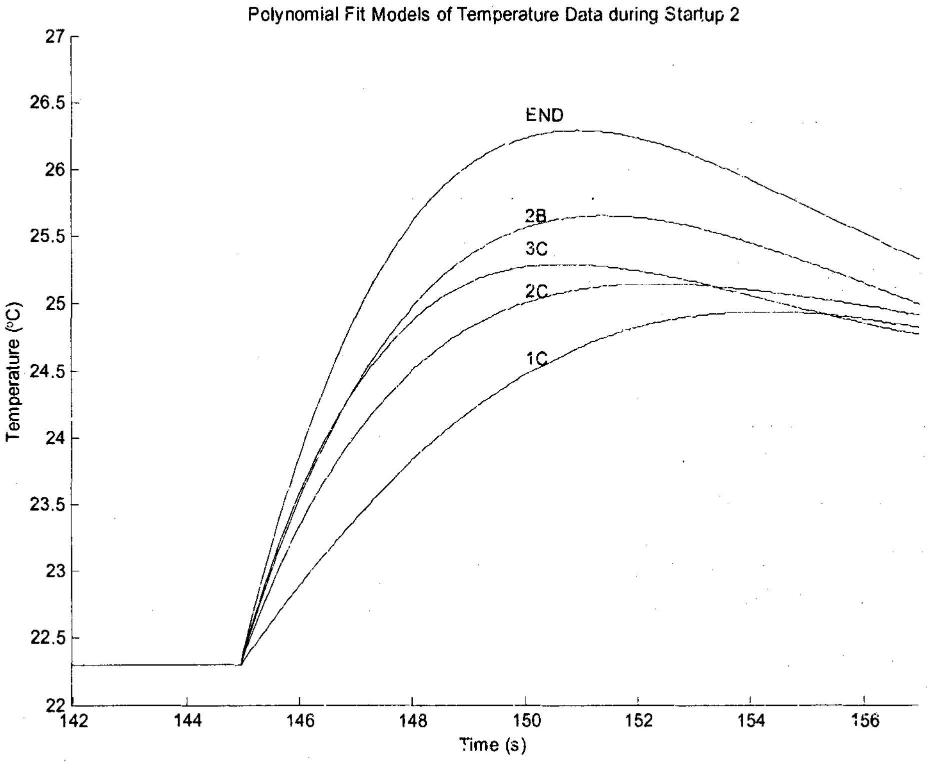

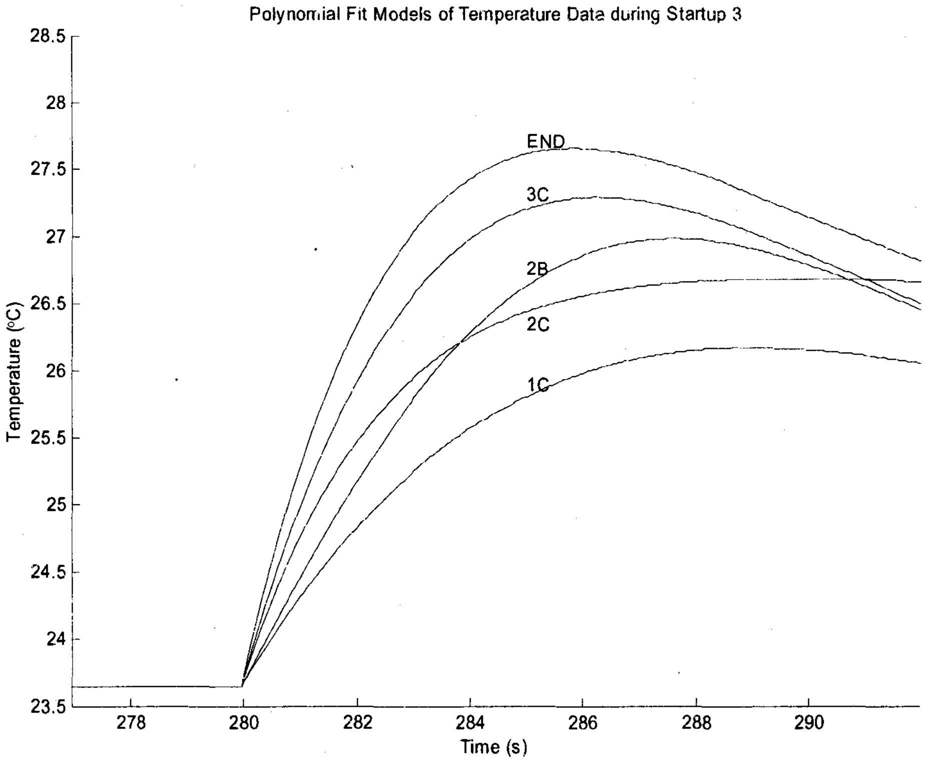

Figure AB.2b: Rate-of-Rise of Thermocouples During Startup: Start-up Test

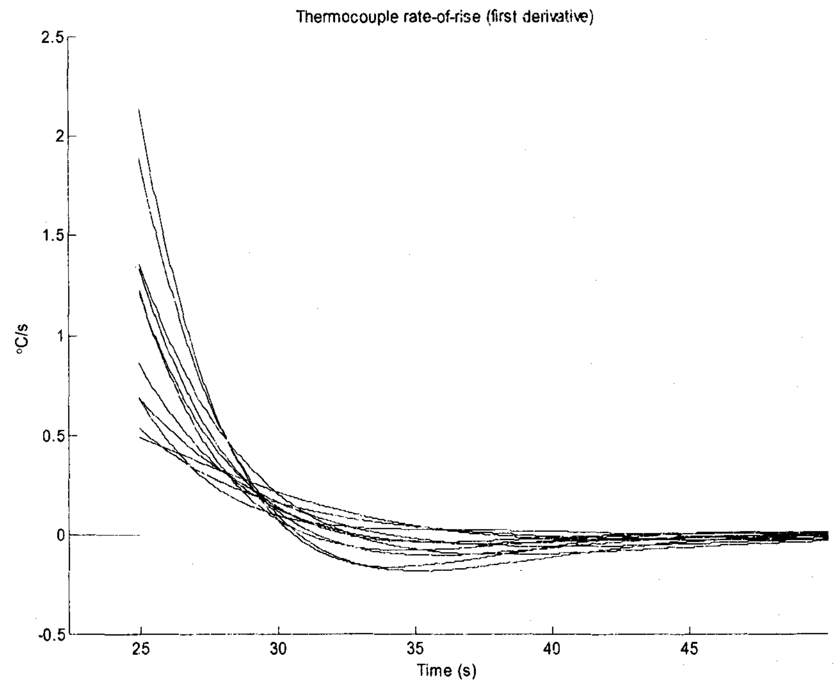

Figure AB.3: First Derivative of Thermocouple Best-fit Polynomials

Appendix C

Data Acquisition Setup

The DAQBOARD-2005 PCI-based data acquisition system used for the experiment was an 8-point differential analog input card manufactured by Omega. The card offers 16-bit A/D conversion resolution, with a maximum sampling rate of 200-kHz over all analog inputs. Additional to the analog inputs, the card supports 40 general purpose digital I/O, 6 on-board counters and timers and 2 frequency generators. This particular analog input card does not support any analog output channels.

The acquisition card is PC mounted, and connected to a terminal based breakout board by an Omega OMB-CA-195 100-conductor high-density ribbon cable. The ribbon cable has a standard female db-37 connector on the breakout board end, which mates to an Omega OMB-DBK200 or equivalent breakout board. The breakout board is field-mounted on the motor, to allow easy connection of measurement instrumentation. The thermocouple and RTD transmitters are mounted on the field breakout board for convenience.

The complete data acquisition system can be seen below in Figure 4.3.5. The system is dissected into three general physical sections:

1. PC related hardware and software

2. Hardware mounted external to both the motor and PC based data acquisition system on a custom breakout board
3. Field instrumentation mounted directly on the test motor

The number of analog instrument readings that can be taken simultaneous by the data acquisition system is limited by three factors:

1. The data acquisition card has a limitation of 200,000 samples per second over all analog points. The card can also accommodate up to 16 single-point or 8 differential analog inputs. Therefore, the maximum number of combined temperature and search coil inputs is 8 at a maximum samplings speed of 25,000 samples/second/input. If a higher sampling rate is required, fewer input points must be used.
2. Only two thermocouple transmitters and one RTD transmitter were purchased, limiting the number of temperature samples per experiment to three.

The instrumentation is place on the rotor, which is embedded inside the stator assembly. All instrument leads must be placed in one of two small slots in the rotor shaft, in order to fit through the bearings in the stator end plates. The slots cannot be made any larger because the shaft must remain strong enough to support the full weight of the stator/rotor assembly. With 30AWG wire leads, approximately 10 thermocouples or RTD's can fit in the shaft slots. The search coil wire used is 24AWG, limiting the number of search coils to approximately 6 per test.

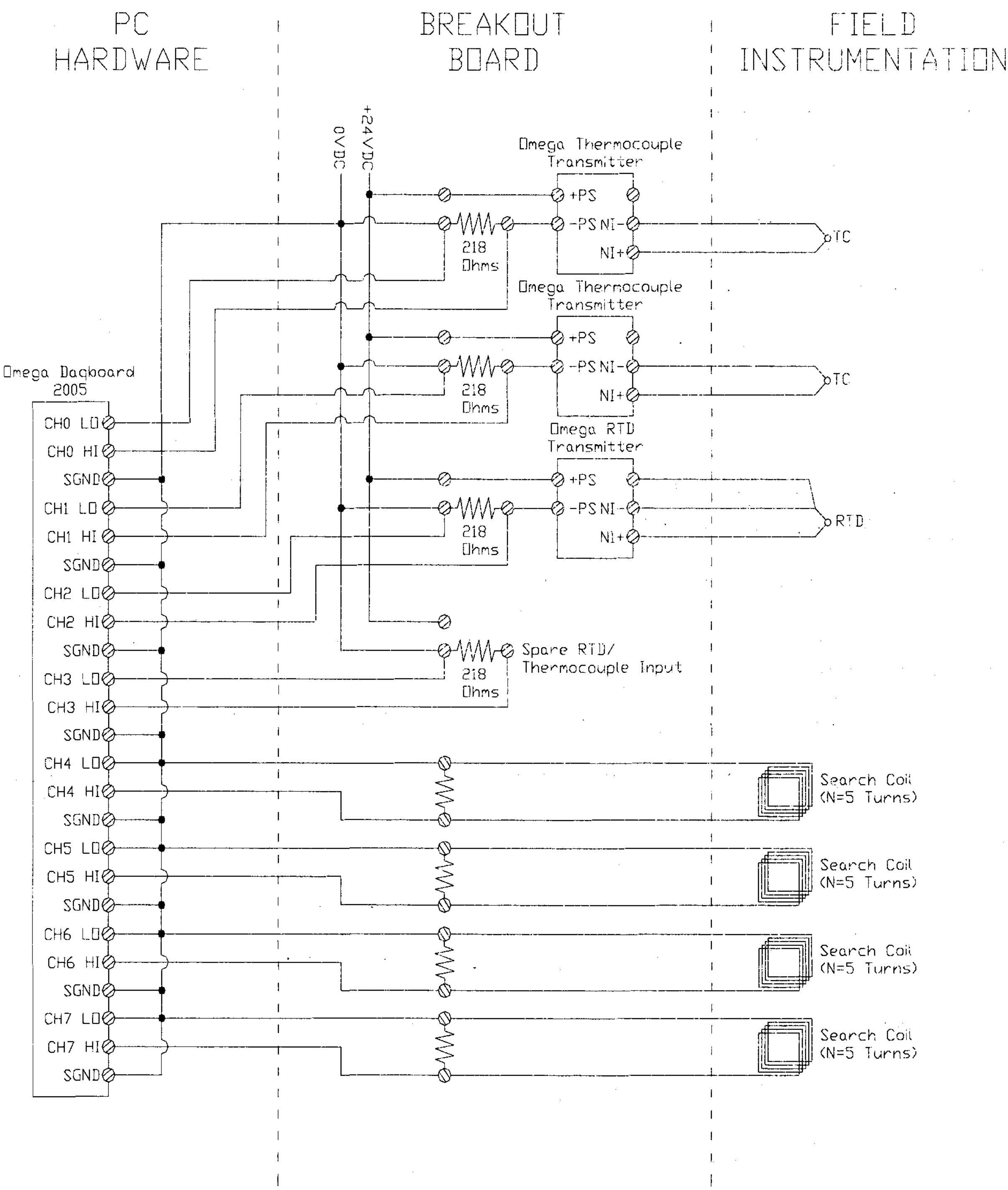

Figure AC.1: Data acquisition setup